SYNTHESIS, CHARACTERIZATION AND PHOTOVOLTAIC INTEGRATION OF TYPE II NANOROD HETEROSTRUCTURES

BY

HUNTER Y. MCDANIEL

DISSERTATION

Submitted in partial fulfillment of the requirements
for the degree of Doctor of Philosophy in Materials Science and Engineering
in the Graduate College of the
University of Illinois at Urbana-Champaign, 2011

Urbana, Illinois

Doctoral Committee:

Professor Moonsub Shim, Chair
Professor Kenneth S. Suslick
Professor Angus A. Rockett
Professor Jian-Min Zuo

ABSTRACT

Motivated by a desire to control the actions of charges within materials in new and productive ways, researchers have increasingly focused their efforts on engineering materials on the nanometer scale where the laws of quantum mechanics rule supreme. Novel properties emerge when a semiconductor crystal is prepared at sizes below the hydrogenic ground state of the material, also known as the exciton Bohr radius. In addition to effects of quantum confinement, the large fraction of surface atoms can play a significant role in determining nanocrystal properties and applications. By combining two or more nanometer scale semiconductor crystals together to form a nanocrystal heterostructure, new avenues for materials engineering are opened up as nascent properties emerge. The high fraction of surface atoms means that much larger degrees of strain are possible than in the bulk. The large fraction of interface atoms means that the heterojunction properties can dominate the properties of the entire structure. Along with engineering these novel multi component properties comes new unexplored areas of science to be investigated and understood. New techniques are needed for studying these materials that require resolution of features much smaller than the wavelength of (visible) light. Along with this research comes a responsibility to share findings with the scientific community and to pursue directions that can positively impact humanity. At the same time, we should take a long term view when judging the applications of this

or any new technology as we are only beginning to understand what is possible.

After an introduction to the field in chapter one where we motivate our focus on anisotropic nanocrystal heterostructures, we discuss the formation of Fe_3O_4/CdS structures from spherical seeds in chapter two. In chapter three we turn our focus to type II CdSe/CdTe nanorod heterostructures where the anisotropy is inherent. The type II system is of particular interest because absorbed photons rapidly produce separated electrons and holes which we suspect could make these attractive materials for photovoltaics. Also in chapter three, we observe unexpectedly high levels of strain in these structures and develop a technique using an aberration corrected scanning transmission electron microscope to argue a hypothesis as to its cause. In chapter four we develop a synthetic strategy to forming alloyed type II nanorod heterostructures and show that we can tune their heterojunction energies. Also in chapter four, we take a further step in developing the structural characterization technique from chapter three by using it to spatially quantify composition in alloyed nanorod heterostructures. In chapter five we explore the time resolved absorption spectra of the various nanorod heterostrucutres discussed in previous chapters in order to probe carrier dynamics in these materials. Finally, in chapter six we tie together the previous chapters by developing a new type of solar cell integrating type II nanorod heterostructures. In a systematic comparison between different nanorod heterostruecutres with single component nanorods, we uncover the conditions under which the attractive qualities of type II nanorod heterostructures can be capitalized on.

To my parents, for their love and support.

ACKNOWLEDGMENTS

In particular, I would like to acknowledge my advisor, Professor Moonsub Shim, for without whom none of this work would have been possible. Initially, I was skeptical of working in an area seemingly so dominated by chemistry following my undergraduate studies in electrical engineering in physics. His encouragement and enthusiasm for nanocrystal science awakened me to one of the most exciting frontiers of materials research. His open mindedness allowed me the freedom to pursue my imagination, of which I consider my most valuable resource. I don't know how my PhD experience would have turned out with another advisor other than that it couldn't possibly be better than the one I have had with Dr. Shim, whom I sincerely thank.

Next, I would also like to thank my committee members; Professors Ken Suslick, Angus Rockett and Jim Zuo. Your support and guidance has been invaluable to me as I have proposed and developed this thesis. I have learned much from you and I hope that I have made you proud. I would also like to thank my group members and collaborators, working with you has been a pleasure.

My parents, Candy and Dudley, thank you for your continued love and support. In particular, thank you for financially supporting my undergraduate studies at the University of California at Santa Barbara where I developed my passion for research. Also thanks to my sister, Katie,

for always keeping me on my toes.

Lauren, you kept me sane these past few years and distracted me when I needed it most. I continue to be inspired by you and look forward to our years ahead. Thank you from the bottom of my heart.

I am grateful to the Materials Science Department at the University of Illinois here at Urbana-Champaign, particularly the hard working administrators who help maintain this program at the highest standard.

Some of this work was supported by the ACS PRF under Grant No. 46443-AC10 and by the Nanoscale Science and Engineering Initiative of the National Science Foundation under NSF Award Number DMR-0642573.

Much of the characterization and fabrication was carried out in the Center for Microanalysis of Materials, University of Illinois, which is partially supported by the U.S. Department of Energy under Grant No. DEFG02-91-ER45439.

Transient Absorption measurments were conducted at the Argonne Center for Nanoscale Materials in collaboration with Dr. Matt Pelton. His assistance was greatly appreciated. Use of the Center for Nanoscale Materials was supported by the U. S. Department of Energy, Office of Science, Office of Basic Energy Sciences, under Contract No. DE-AC02-06CH11357.

TABLE OF CONTENTS

LIST OF COMMONLY USED ABBREVIATIONS

NC	Nanocrystal
NR	Nanorod
NCH	Nanocrystal Heterostructure
NRH	Nanorod Heterostructure
CSS	Charge Separated State
PL	Photoluminesence
TEM	Transmission Electron Microscopy
STEM	Scanning Transmission Electron Microscopy
EDS	Energy Dispersion X-ray Spectroscopy
ETA	Extremely Thin Absorber
ETL	Electron Transport Layer
HTL	Hole Transport Layer
EQE	External Quantum Efficiency
PV	Photovoltaic

CHAPTER 1

INTRODUCTION

Advances in synthetic precision over the size, shape, and composition of nanocrystalline materials are inspiring increasingly revolutionary technological breakthroughs [1–5]. A variety of novel properties may arise when materials are prepared in the nanometer size regime including tunable band energies (semiconductors) [6], enhanced carrier multiplication (narrow gap semiconductors) [7, 8], room temperature superparamagnetism (magnetic oxides), efficient catalysis [9] and much more. Materials with such properties exhibit promise in multiple areas including lasers [10], novel display technologies [11, 12], photodetectors [13], solar energy conversion [14], drug delivery, and biomedical imaging [15–17]. Further, solution based processing techniques offer the potential for low cost and large scale synthesis of nanocrystals (NCs) which can be made soluble in a variety of solvents.

We can envision capabilities well beyond the current state-of-the-art; however, there are many obstacles in transitioning from interesting properties being observed to functional devices and systems. Highly efficient, size-tunable, photoluminescence (PL) makes semiconductor NC solids attractive as a lasing medium but fast Auger recombination rates hamper optical gain [10]. High PL efficiencies place semiconductor NCs at the forefront of bioimaging research but uncontrolled blinking is a hindrance for pushing the limits, especially at the single NC level [18, 19].

Large surface-to-volume ratios provide an advantage for photocatalytic production of hydrogen, as well as a variety of other catalytic processes with TiO_2 NCs, but the ultraviolet band gap of TiO_2 renders solar energy driven photocatalysis inefficient [20].

In the pursuit of lowering cost and increasing photovoltaic efficiency, researchers have looked at incorporating NCs in solar cells. Three approaches have been employed with varying degrees of success. Schottky cells, with NCs sandwiched between two metal electrodes, offer a simple approach that has produced photon conversion efficiencies (PCE) as high as 3.3% [21, 22]. Quantum dot sensitized solar cells (QDSSC) use band gap tuned NCs to sensitize a wide gap semiconductor, usually TiO_2 or ZnO, to the solar spectrum and rely on an electrolyte for hole transport [23]. Hybrid organic-inorganic photovoltaics employ a bulk heterojunction (BHJ) between NCs and an organic semiconductor to dissociate excitons generated in the blend. Hybrid BHJs have demonstrated PCEs of up to 2.8% [24]. While significant improvements have been made, PCEs remain low compared with the current record for a thin film, single junction, solar cell at above of 20%.

In recent years, synthetic techniques have been developed for creating anisotropic structures, such as nanorods (NRs), with precision over diameter and aspect ratio. For example, wurtzite II-VI semiconductors can be easily prepared in the rod shape with the addition of alkylphosphonic acids [25]. Surface capping molecules, along with enhanced reactivity of polar facets, enhance growth of these crystals along the [0 0 0 1] direction [26]. NRs are attractive for various reasons that include polarized absorption and emission, enhanced carrier mobility in films, and further increased surface to volume ratios. Since the quantum size effect on band

gap primarily depends on the dimension of greatest confinement, the band gap of NRs can be tuned with diameter control while maintaining extremely high aspect ratios. With respect to solar cell applications, the anisotropy of NRs has been shown to enhance PCEs in hybrid BHJs by improving charge transport [27].

Utilizing nanocrystal heterostructures (NCHs), additional properties and applications are beginning to emerge. Type I band offset core/shell NCHs, where a small gap core is surrounded by a passivating and confining larger band gap shell, demonstrate greatly enhanced PL quantum yield [28], often reduced toxicity, and can exhibit steady PL without blinking [29]. Of particular interest in photovoltaic applications, type II NCHs have been shown to exhibit rapid photo-induced charge separation [30], long carrier lifetimes, charge separated state (CSS) absorption and optical gain [31]. A shell thickness dependent transition from a type I to a type II band offset has been demonstrated in core/shell NCHs based on the quantum size effect [32] and also lattice strain [33]. Anisotropy will be especially important in NCHs for charge processes that require directionality and exposure of all components to the outside environment. In core/shell NCs, the core material is isolated from the outside environment chemically, physically and electrically which will be unacceptable for applications in catalysis or photovoltaics where both carriers must be extracted.

Using one component as a seed for the growth of the second phase, there have now been several different materials incorporated into non-core/shell heterostructures [34–42]. With anisotropy inherent in the crystal structure, wurtzite phase NR seeds may be the most obvious choice of seed materials for promoting anisotropy in NCHs [43]. Exclusive or near exclusive deposition of the second material at the tips can be achieved by

direct extension of the initial NR growth in a single pot synthesis. Although not straight forward, we don't have to be limited to forming anisotropic NCHs from anisotropic seeds. In systems with a large lattice mismatch, lattice coincidence, strain effects, and facet reactivity drive the junction formation process [44–46] and can be taken advantage of in order to promote anisotropy.

Because no two distinct materials have identical lattice constants, strain exists to varying degrees in all NCHs. Strain often dictates achievable structure(s) and therefore, can play a role in developing synthetic techniques. Further, strain can potentially be used as a method of tailoring NCH constituent band gaps and band offsets which is of particular importance in applications requiring charge separation [47]. Some of the key unknowns in this field are associated with how anisotropic strain manifests itself in NCH morphology, electronic and optical properties.

1.1 Objective

Research of NCHs will be of interest in a wide array of noted fields but the area of greatest societal need, and potential global impact, is in energy conversion. How can we engineer NCHs, in particular, anisotropic NCHs such as NR heterostructures (NRHs), for useful photon harvesting? Anisotropy has already been shown to be of critical importance for single phase NC based hybrid BHJ solar cells, and we expect that anisotropy should be even more critical in NCH based solar cells since each component of the heterostructure should be accessible in specific ways. The first objective then necessarily becomes the development of techniques for promoting NCH anisotropy by seeded growth from either anisotropic (e.g.

NRs) or isotropic (spherical) seeds. Secondary to this objective, is an awareness of strain and determining what role strain plays in promoting anisotropy.

In order to develop NCHs for photovoltaic applications, we should begin to narrow the scope of materials to be incorporated to those which have reasonable solar spectrum absorption and also type II band offsets. Further, we should focus on materials which can be fabricated by scalable colloidal techniques. The focus becomes creating cheap materials, which are highly effective at absorbing solar photons, and converting them into free carriers for extraction to electrodes. The next key question to answer is; can we design NCHs to promote photo-induced charge separation? Due to their extremely high surface to volume ratios, NCs can accommodate higher strain than bulk materials, and more importantly, they can accommodate extremely high strain/volume ratios . Thus, strain considerations not only become crucial for understanding the properties of NCHs but potentially empowering. Aside from strain effects, by choosing particular constituent compositions or engineering their relative orientations, we might be able to tune the band structure in ways that directionally separate carriers.

While there have been a few reported attempts to incorporate type II NCHs into photovoltaics to date, the results have mostly been disappointing because researchers simply sought to replace single phase NCs with NCHs in previously successful NC based devices [48–50]. NCHs would play a fundamentally different role in a photovoltaic device than single phase NCs. So finally, in order to demonstrate the importance of research on anisotropic type II NCHs, we will show that the rational design of NCHs can lead to improved photovoltaic performance if a solar cell is designed to appropriately take advantage of their attractive qualities.

CHAPTER 2

ANISOTROPIC NANOCRYSTAL HETEROSTRUCTURES FROM SPHERICAL SEEDS

Significant components of this chapter were published as "Size and Growth Rate Dependent Structural Diversification of Fe_3O_4/CdS Anisotropic Nanocrystal Heterostructures" in ACS Nano [46].

Anisotropic Fe_3O_4/CdS NCHs have been synthesized from nearly spherical Fe_3O_4 seeds prepared from thermal decomposition of $Fe(CO)_5$ in oleic acid and octyl ether following ref [51]. Oleic acid acts as the surface capping molecule and its concentration allows the average size of the seed NCs to be varied from ∼3 nm to ∼20 nm. The ability to control the average size while maintaining a relatively narrow size distribution of ∼5 - 10 % makes Fe_3O_4 NCs ideal for examining size-dependent strain effects.

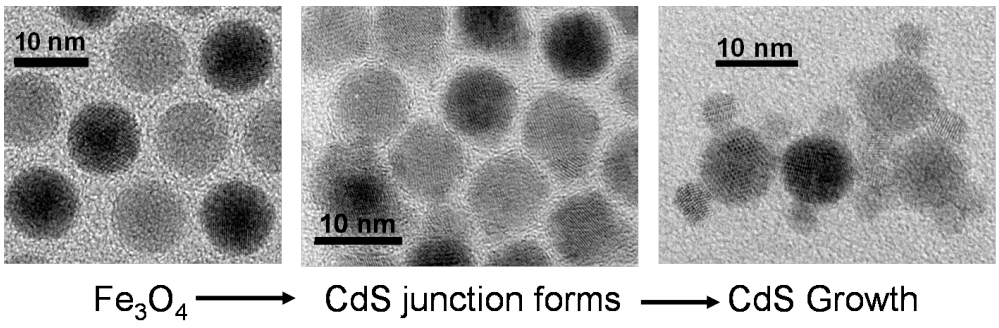

Figure 2.1: The general synthesis procedure. First, Fe_3O_4 of desired size is synthesized. CdS junctions are formed with the desired frequency by varying the amount of Cd/S reagent added in the first injection. Growth of the preformed nuclei occurs upon subsequent addition of Cd/S reagents. Notice the change in NC morphology from isotropic to increasingly anisotropic. In the junction formation step, Fe_3O_4 NCs appear to have small lumps which are the CdS nuclei.

2.1 Formation of junctions and growth of CdS from Fe_3O_4 seeds

The CdS precursors consist of bis-trimethylsilylsulfide (TMS_2S) in Triocylphosphine (TOP) for the S source and $Cd(CH_3)_2$ in TOP for the Cd source. The all-solution phase precursors provide the versatility with which Fe_3O_4/CdS junction formation can be separated from subsequent growth of CdS. The S and Cd reagent solutions are added sequentially followed by an annealing step which establishes the average number of CdS particles that nucleate on each Fe_3O_4 seed NC. Subsequent injection of TMS_2S and $Cd(CH_3)_2$ mixed together in TOP extends the growth of CdS from the nuclei on the surfaces of Fe_3O_4 NCs (see Figure 2.1). The average number of CdS particles that grow on Fe_3O_4 NCs can be controlled by varying the amount of S and Cd in the initial junction formation step. However, as Figure 2.3 shows, the maximum number of CdS particles that can grow on the seed NCs depends strongly on the size of the Fe_3O_4 NCs with the limitation approaching one CdS particle per seed for the smallest sizes. The details of the synthesis can be found in the methods of this chapter.

Fe_3O_4 has a cubic inverse spinel crystal structure with a lattice constant a = 0.837 nm while CdS is polymorphic and will form in either the zinc blende (cubic with a = 0.583 nm) or wurtzite (hexagonal with a = 0.414 nm and c = 0.672 nm) phase. Considering the overwhelmingly large 30 % lattice mismatch in the bulk Fe_3O_4 and CdS lattice parameters, it is surprising that these two materials form a stable interface at all. A careful examination of high resolution TEM images, as exemplified by Figure 2.2, shows that the predominant junction planes are well-aligned (111)/(111) interface for zinc blende CdS and (111)/(0001) interface for wurtzite CdS.

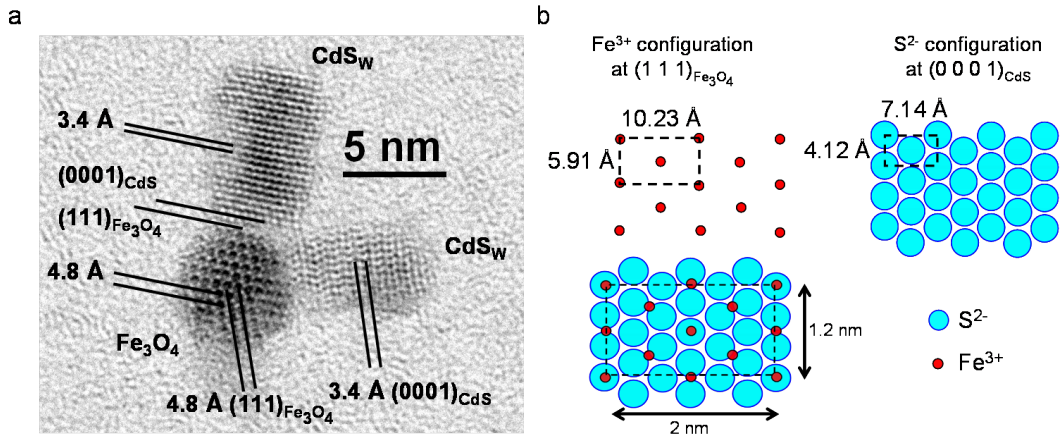

Figure 2.2: **a,** High resolution TEM image of a Fe3O4/CdS nanocrystal heterostructure. Lattice spacings measured by integrated line scans are also shown. **b,** Schematic of the heterointerface and the alignment of the junction planes are shown. Red circles correspond to Fe atoms and blue to S atoms.

When lattice fringes are visible in both Fe_3O_4 and CdS, as is the case in Figure 2.2, the relative orientation of the crystallographic planes at the interface can also be identified. Both zinc blende and wurtzite cases lead to the same atomic arrangement at the heterointerface as schematically shown in Figure 2.2. Considering the zinc blende case, 3 atomic steps along the $[1\,\bar{1}\,0]$ direction of CdS is nearly identical in length as 2 atomic steps along the same direction on Fe_3O_4. Similarly, 3 and 2 steps along the $[1\,1\,\bar{2}]$ direction for CdS and Fe_3O_4, respectively, lead to nearly identical lengths. This coincidental overlap of lattice sites at the heterojunction is what maintains the epitaxial and stable interface in otherwise incompatible lattice structures. When CdS grows in hexagonal wurtzite structure, there are also significant cases where the CdS part of the junction plane is the $[1\,\bar{1}\,0]$ plane which is usually accompanied by stacking faults. The stacking faults lead to partial conversion of the plane to the (111) plane of zinc blende CdS. Then, the heterojunction becomes similar to the (111)/(111)

interface shown in Figure 2.2.

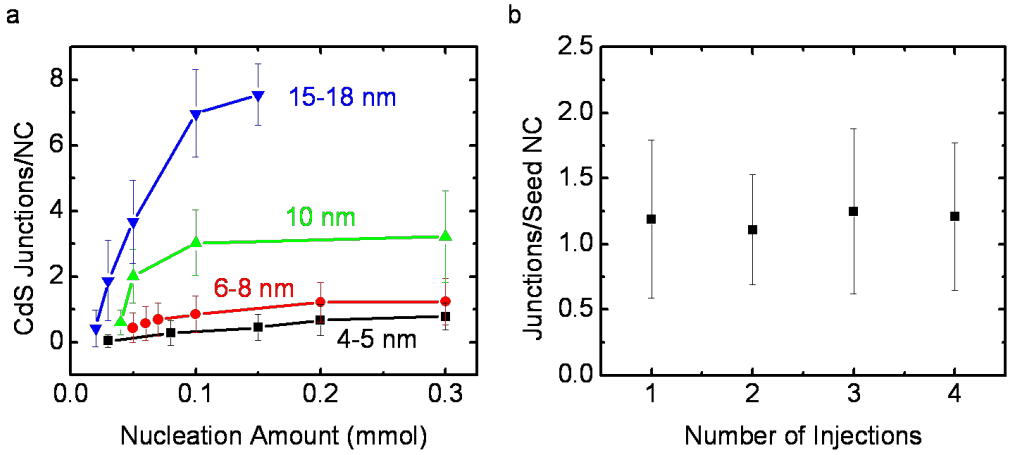

Figure 2.3: **a,** The relationship between junction frequency, Fe_3O_4 seed size, and nucleation precursor amount. Each data point is a single synthesis which started with seed Fe_3O_4 in one of the four ranges (4.7nm, 6.9nm, 10nm and 16.1nm average sizes). Junction frequency increases with nucleation amount up to a saturation number which depends on Fe_3O_4 size. Junction frequencies less than one result from a population of isolated Fe_3O_4 NC. Error bars are the standard deviation in the data. **b,** Average number of junctions formed per seed NC with multiple CdS growth steps (number of injections). Fe_3O_4 NCs of average diameter 6.7 nm are first nucleated with 0.1 mmol of CdS precursors. Each growth step consisted of 5x Cd/S reagent amount used for the initial nucleation. Error bars are the standard deviation of the number of junctions per seed NC counted from TEM images.

The heterointerfaces observed above indicate the importance of coincidence site lattices [52, 53] which have been widely used to explain planar heteroepitaxy in large lattice mismatched systems [54] and large angle grain boundaries [55]. Since our group's initial work on Fe_3O_4/CdS [44, 45], several other systems including Cu_2S/In_2S_3 NCHs have been shown to exhibit coincidence lattices [56, 57]. However, based on the bulk lattice parameters (see Figure 2.2), the (111)/(111) Fe_3O_4/CdS interface should still exhibit a non-negligible mismatch of 4.6% along each of the directions with coincident lattice sites. This mismatch manifests itself in how strain

builds up with increasing size of any one component of the NCHs.

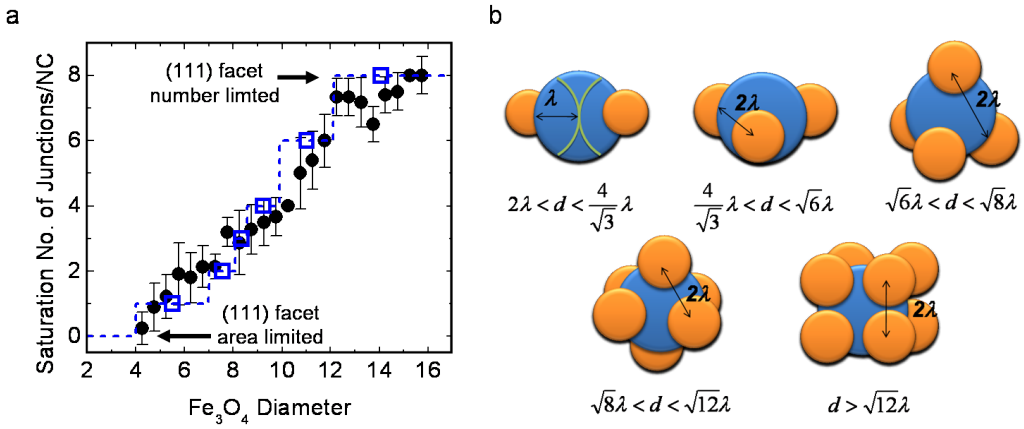

Figure 2.4: **a,** Seed diameter dependence of the maximum number of CdS particles that can nucleate and grow on Fe_3O_4 nanocrystals. At the smallest sizes, nucleation of CdS is hindered due to the (111) junction plane area being too small and therefore incapable of supporting heterogeneous nucleation. At the largest sizes, the total number of (111) facets available prevents further nucleation of CdS. The blue dashed line is derived from a simple interfacial strain dependent geometrical constraint model with $\lambda =$ 3.5 nm. **b,** Schematics and the corresponding diameter range for the simple geometrical model described in the text. A fixed effective strain length (λ) leads to limitations on the maximum number of junctions per NC of a given diameter (d).

The maximum number of CdS particles that can grow on each seed Fe_3O_4 NC has been shown to be dependent on the size of the seed NC in Figure 2.3. For a more precise size dependence, NCHs synthesized in the saturated regime where the maximum number of CdS particles per seed NC is reached were examined. The Fe_3O_4 seed diameter dependence of the maximum number of CdS particles that can grow per Fe_3O_4 NC is shown in Figure 2.4. Since each reaction leads to Fe_3O_4 NCs with a size distribution of about 5 to 10 %, data shown is binned at diameter increments of 0.5 nm. A near linear dependence is seen in the diameter range from ~4 to ~12 nm and seems to plateau at ~8 CdS particles for largest sized seeds which is imposed by the limited number of (111) facets available. At the small size

range, there should be a limitation from the surface area of the (111) planes since at ∼4 nm seed diameter, the (111) facets should to be about 2 nm across which is about the size scale of a single coincident unit cell (see Figure 2.2). This may reflect the critical size for heterogeneous nucleation.

In order to better understand how strain might limit the growth of CdS on seeds of various sizes we developed the simple geometrical model depicted in Figure 2.4b. In this model, we assume a fixed strain interaction length (λ) for every junction which could not overlap. If we ignore the restrictions imposed by the lattice symmetry, and only account for this fixed length which must exist between any two junctions (2λ), then we come up with discrete seed sizes for which a given number of junctions can exist. For $\lambda = 3.5$ nm, our data fits the model relatively well (see dashed blue line in Figure 2.2a).

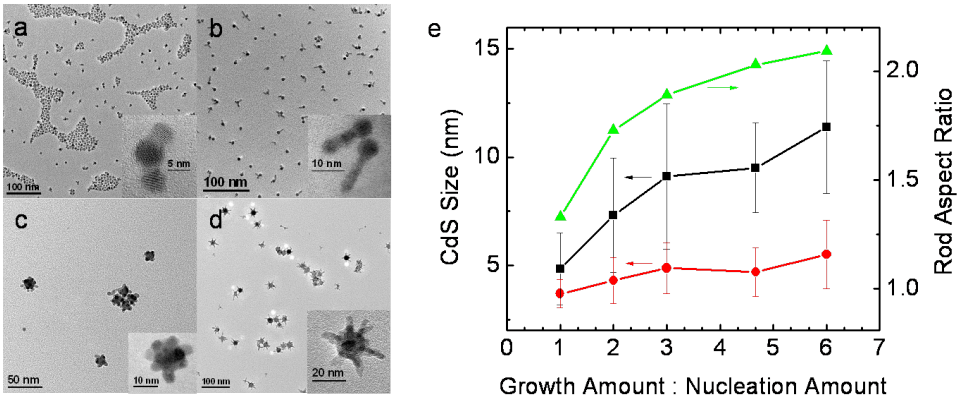

Figure 2.5: **a,b,c,d,** TEM images demonstrating rod-on-dot anisotropy dependence on precursor concentration. Smaller size seed Fe_3O_4/CdS NCs with 1:1 (**a**) and 5:1 (**b**) growth-to-nucleation CdS precursor amount ratio leading to slow and fast CdS growth, respectively. (**c**) and (**d**) are analogous to (**a**) and (**b**) for larger sizes of seed NCs. Higher magnification images are shown in the insets. **e,** Rod-on-dot anisotropy dependence on precursor concentration is quantified. We vary the ratio of growth precursor amount to nucleation precursor amount for a fixed seed size (7nm) and fixed nucleation amount (0.15 mmol).

In most previous reports, a delicate balance between reaction

temperature, concentrations of reagents, reactivity of precursors, and types of capping molecules is necessary in optimizing NR growth. With our approach to the synthesis of Fe_3O_4/CdS NCHs, where the junction formation is separated from growth, the growth step can be easily adjusted to promote CdS rod growth. As a simple control over the growth rate, the amount of CdS precursors added in the second injection step relative to the junction formation step can be increased. Figure 2.5 shows TEM images of CdS rod growth from nearly spherical Fe_3O_4 seeds that can be achieved by simple increase in the second precursor injection amount without any other changes. The initial CdS reagent injection allows control over the number of CdS particle nucleated and the subsequent growth injection(s) can determine size/length/anisotropy.

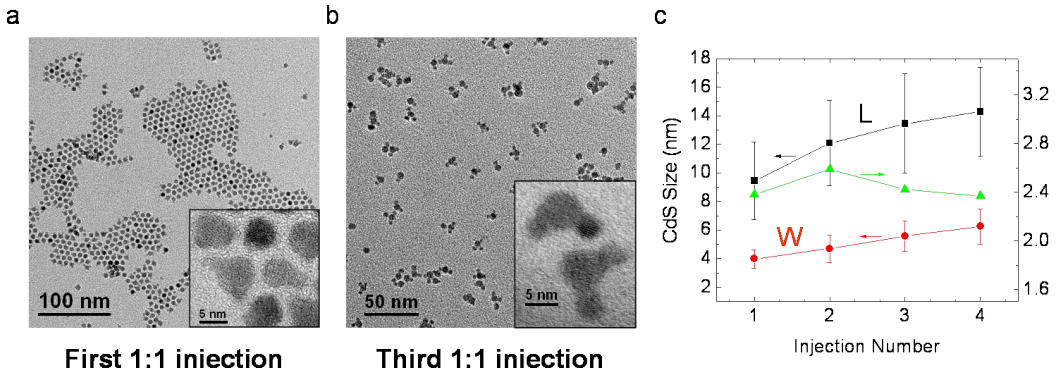

Figure 2.6: **a,b,** Low and high (inset) magnification TEM images demonstrating dot-on-dot growth achieved by multiple low concentration (1:1 (growth-to-nucleation)) injections at the first (**a**) and third (**a**) injection. **c,** The dependence of length (black), width (red) and aspect ratio (green) of CdS (grown on Fe_3O_4 seeds) on the effect of multiple high concentration (6:1) injections in attempt to increase CdS aspect ratio. The plot is produced from samples taken during a single synthesis.

In an effort to increase the aspect ratio beyond ∼2, we did additional high concentration injections of CdS precursors. We found that while the length of the CdS rods did increase, the width increased equally

fast leaving the aspect ratio nearly unchanged (Figure 2.6c). This result is likely due the additional surface area available on the rod for CdS material to deposit. We could intentionally reduce the size of the CdS growth without increasing aspect ratio by conducting multiple low concentration injections (Figures 2.6a and 2.6b). Alternatively, increasing the oleic acid concentration (capping agent) is another simple means of retarding CdS rod growth. Increasing the capping agent concentration slows CdS growth by increasing the effective coverage of the CdS surface. Even at the elevated 5:1 growth-to-nucleation precursor ratio, CdS rods would not form if the oleic acid concentration had been increased by only 36% (Figure 2.7b).

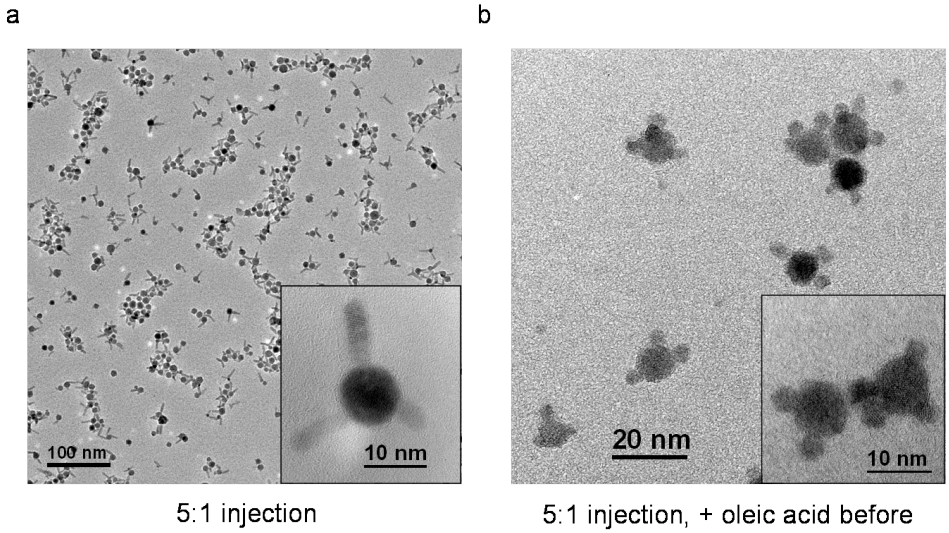

Figure 2.7: **a,b,** Low and high (inset) magnification TEM images demonstrating the effect of adding additional oleic acid prior to the growth step. In a typical 5:1 (growth-to-nucleation) injection, CdS nanorods extend from the Fe_3O_4 seeds (**a**). Increasing the oleic acid 36% prior to a 5:1 injection for growth led to rod-on-dot morphology exclusively (**b**).

2.2 Wurtzite/zinc blende polytypism and structural diversification

Previous studies on Fe_3O_4/CdS NCHs have shown that the CdS can grow as wurtzite or zinc blende [45]. This polytypism in CdS leads to diversification of possible morphologies within the rods-on-dot geometries even when the number of nuclei per seed NC can be controlled. While the structural diversity may be amplified, the rods-on-dot structures can in turn facilitate characterizing crystallographic orientations at the heterojunctions due in part to the larger sizes of the rods and in part to easy-to-identify rod growth axis. There are three distinct CdS rod configurations that we have observed in the rods-on-dot NCHs. In all three configurations, CdS always grows on the $\{1\,1\,1\}$ plane of the seed Fe_3O_4 NCs.

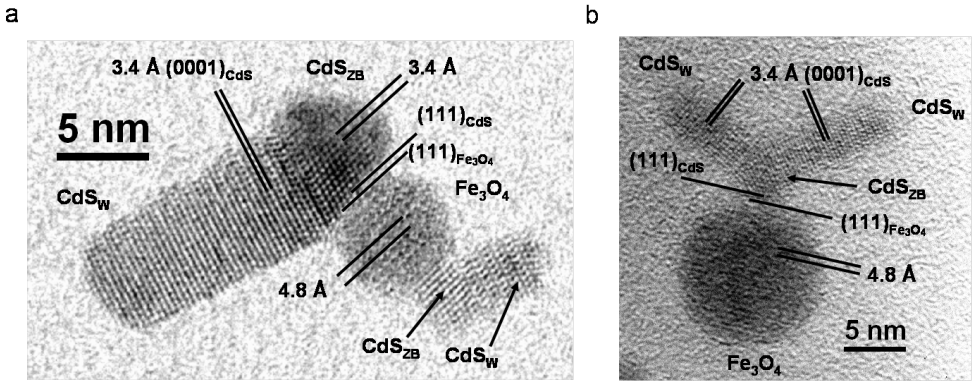

Figure 2.8: **a,b,** High resolution TEM images of branched CdS nanorods grown on Fe_3O_4/CdS NCs. Branching occurs by initial zinc blende nucleation followed by wurtzite growth. An example is shown for small (**a**) and large (**b**) seed NCs. Note that the junction planes are the same in both cases.

For NCHs with 7 - 9 nm Fe_3O_4 seeds, the most abundant of the three configurations is the "branched" structure (56% out of 126 junctions examined via high resolution TEM) as shown in Figure 2.8a. For the larger 15 - 16 nm seed diameter, as shown in Figure 2.8b, we observe similar, but

slightly lower, yield of these branched junctions (41% out of 79 junctions). Note that these structures sometimes have only one branch as shown in Figure 2.8a which then makes them appear similar to the "kinked" structures discussed later. However, the single-branch structure can be easily distinguished from the kinked structures by high resolution images showing lattice fringes and by difference in the angle of the rod growth direction with respect the Fe_3O_4 {1 1 1} plane. Branching occurs when the CdS is initially nucleated as zinc blende and fast growth conditions favoring rod growth lead to tetrapod-like structures where wurtzite rods grow out of the {1 1 1} planes of the zinc blende nuclei. The Fe_3O_4/CdS heterojunctions in these cases are the zone axes aligned {1 1 1}/{1 1 1} planes with coincidence sites shown in Figure 2.8b.

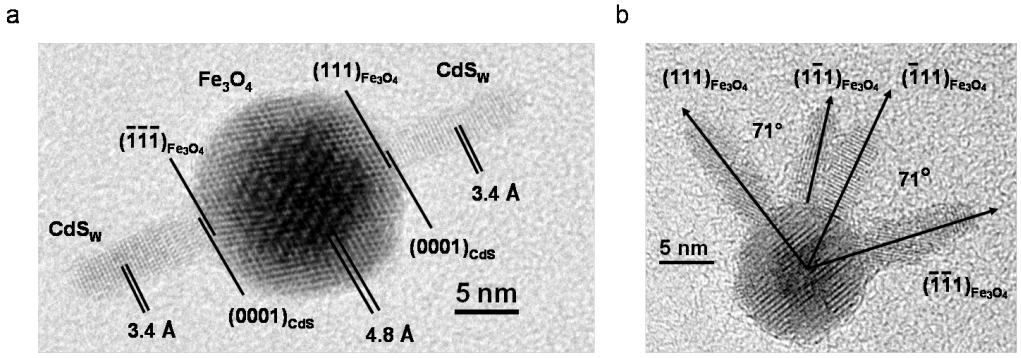

Figure 2.9: **a,b,** High resolution TEM images of linear CdS nanorods grown onFe_3O_4/CdS NCs. Linear rods arise from nucleation of wurtzite CdS and continues wurtzite growth. An example is shown for two (**a**) and four (**b**) CdS growths.

For the smaller 7 - 9 nm seed size range, the second most abundant configuration observed is the linear structure (27%) as shown in Figure 2.2a. At the larger seed size of 15 - 16 nm, we observe a substantial increase in the yield of these junctions (58%) as shown in Figure 2.9. These linear structures arise from CdS being nucleated as wurtzite and continuing to

grow in the same crystal structure with preferential growth along the (0 0 0 1) direction. The heterointerfaces in this configuration are the same junction planes with coincidence sites as shown in Figure 2.2b with the {0 0 0 1} planes for CdS which is equivalent to the {1 1 1} planes of zinc blende.

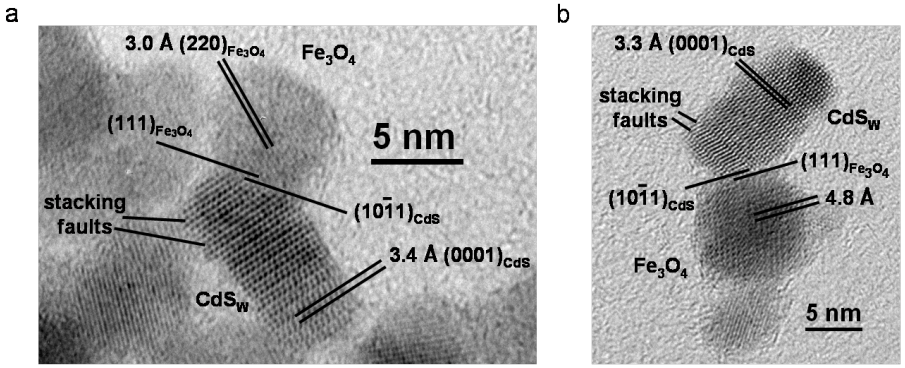

Figure 2.10: **a,b,** High resolution TEM images of kinked CdS nanorods grown on Fe_3O_4/CdS NCs. Note the stacking faults near the junction in the CdS which are often observed and may help to better accommodate the heterointerface.

The least frequently observed NCH morphology is shown in Figure 2.10. This "kinked" structure, which is observed ∼15% of the time for the smaller 7 - 9 nm seed NCs and only ∼1% of the times for the larger 15 - 16 nm seeds, arises from wurtzite CdS growth. The heterojunction in this case consists of {1 1 1}/{1 0 $\bar{1}$ 1} interface. These kinked structures are also often associated with stacking faults near the Fe_3O_4/CdS interface as indicated in Figure 2.10. The {1 0 $\bar{1}$ 1} planes of wurtzite is a near close-packed plane - i.e. similar to the {0 0 0 1} plane. Incorporating the stacking faults, the CdS part of the interface then becomes the same as or very close to the junction plane with coincidence sites shown in Figure 2.2b. We believe that the main reason for the low yields of these kinked structures on larger seed Fe_3O_4 NCs may be associated with interfacial strain. The smaller seed NCs

will likely accommodate strain better making it more versatile for the CdS $\{1\,0\,\bar{1}\,1\}$ junction plane to form.

2.3 Fe_3O_4/CdS conclusions

In the Fe_3O_4/CdS system we successfully showed that NCH anisotropy was possible from nearly isotropic seeds primarily due to limited lattice coincidence. We showed that strain limited the number of heterojunctions that could form on seeds of a given size, and consequently, that larger seeds could accommodate more junctions. Finally, we demonstrated that by tuning the precursor concentration and surfactant chemistry during the growth step we could tune the anisotropy of the second component. Unfortunately, although the ideal bulk band alignment between Fe_2O_3 and CdS is type II, the Fe_3O_4/CdS system is inadequate for photo-induced charge separation because Fe_3O_4 contains many mid gap nonradiative recombination sites as evidenced by the brown color of Fe_3O_4 NCs. These mid gap states are associated with oxygen deficiencies and the two oxidation states of iron in the material (Fe^{2+} and Fe^{3+}), and result in the expected PL of CdS being completely quenched for the final products. While this quenching indicates some degree of energy or charge transfer, the usefulness of such transfer is in doubt. After having demonstrated how to drive anisotropy in NCHs from spherical seeds, we moved exclusively towards II-VI materials that exhibited higher PL yields and chose combinations which had type II band alignment.

2.4 Methods

All syntheses were carried out using standard airless techniques under N_2. Reagents were used as received. All steps of the synthesis described below were carried out as a "one-pot" synthesis where the reaction mixture is always kept in the same reaction vessel under N_2. Small aliquots were taken out of the reaction mixture after each step for characterization.

2.4.1 Synthesis of Fe_3O_4 NCs

Fe_3O_4 NCs were prepared in a 50 ml three neck round bottom flask with a reflux condenser by thermal decomposition of 0.2 ml of $Fe(CO)_5$ in a vacuum degassed solvent of dioctyl ether and oleic acid according to ref. [51]. The average size of the NCs was controlled by changing the amounts of oleic acid and dioctyl ether, while the amount of iron pentacarbonyl was kept constant in all syntheses. As an example, 10 ml of dioctyl ether and 1.1 ml of oleic acid were used to make NCs with 7 nm average diameter. We note that vacuum degassing of the solvent to consistent dryness is important in achieving desired size of Fe_3O_4 with narrow size distribution.

2.4.2 Heterojunction Formation

Following the synthesis of Fe_3O_4 NCs, the reaction mixture was cooled to 100 °C under N_2 and an indicated amount of 1 M bis-trimethylsilylsulfide (TMS_2S) in 3 ml of trioctylphosphine (TOP) was injected. The solution was then heated up to 180 °C at ∼15 °C/min and held at this temperature for 5 min before cooling to 60 °C. An equimolar amount (1:1 Cd:S) of 1 M $Cd(CH_3)_2$ in TOP was then added dropwise to the reaction mixture. After 5 min of vigorous stirring the solution was heated at ∼15 °C/min to 250 °C

and maintained at this temperature for 30 min. As discussed below, the amount of CdS precursors injected for this junction formation step (which we interchangeably refer to as the nucleation step) determined the average frequency of heterojunctions formed per seed NC.

2.4.3 Subsequent growth of CdS

Following the nucleation step, the reaction mixture was cooled to 60 °C and indicated amounts of 0.5 M $Cd(CH_3)_2$ and TMS_2S in TOP (1:1 Cd:S molar ratio) were added dropwise. After stirring for 5 min, the solution was heated up to 200 °C at ∼15 °C/min and annealed for 1 h. At annealing temperatures of 200 °C and below, the rods-on-dot geometry is maintained but higher temperature annealing (e.g. reflux at ∼280 °C) causes structures to slowly revert to dots-on-dot morphologies. The resulting NCHs can be precipitated with ethanol and redissolved in non-polar solvents. The molar ratio of growth injection of CdS precursors to the nucleation amount determines the aspect ratio of the epitaxially grown CdS. Smaller growth:nucleation Cd/S reagent ratios lead to spherical CdS grown on Fe_3O_4 NCs while higher ratios lead to CdS rod growth. Injecting more than 6x the amount of Cd/S reagent for the growth step than the nucleation step generally leads to homogeneous nucleation of isolated CdS NCs. This is independent of the nucleation amount. Adding oleic acid before the growth step greatly reduced the aspect ratio for CdS. The overall junction formation and growth of CdS on Fe_3O_4 NCs are outlined in the series of TEM images in Figure 2.1.

2.4.4 Characterization of NCHs

Transmission electron microscopy (TEM) samples were prepared using a dilute chloroform solution (optical density of ∼0.1 at ∼600 nm) of NCs on Cu grids coated with a thin carbon film (Tedpella Inc.). TEM analysis was conducted with a JEOL 2010 LaB6 operating at 200kV. Powder x-ray diffraction (PXRD) measurements were carried out on a Rigaku Geigerflex with a D-MAX system. Fe_3O_4 NCs typically had standard size deviation of 6%. Samples with higher than 10% size distribution were not included in the statistical analysis. In all plots shown, the error bars are the standard deviation in the TEM statistics from the average value which is the plotted point.

CHAPTER 3

STRAIN INDUCED NANOROD HETEROSTRUCTURE CURVATURE

Significant components of this capter wre published as "Anisotropic Strain-Induced Curvature in Type-II CdSe/CdTe Nanorod Heterostructures" in the Journal of the American Chemical Society [58]. Additionally, some portions were published as "Anisotropic Nanocrystal Heterostructures: Synthesis and lattice strain" in Current Opinion in Solid State and Materials Science [59].

Semiconductor nanocrystal heterostructures (NCHs) are adding new dimensions to how unique size-tunable electronic and optical properties of nanocrystals (NCs) can be engineered. There is an increasing interest in NCHs that can promote photo-induced charge separation. Shell thickness dependent transition from type I (carrier confining) to type II (carrier separating) band offset has been demonstrated in core/shell NCHs. In addition to this approach to tuning the relative band offsets, nanorod - (NR) and nanowire based heterostructures with inherent anisotropy can provide directionality in charge separation necessary for energy applications. Here we report anisotropic strain in CdSe/CdTe nanorod heterostructures (NRHs) driven by the growth of lattice-mismatched CdTe unevenly on the sides of CdSe NR seeds. Atomic resolution scanning transmission electron microscopy (STEM), in addition to high-resolution transmission electron microscopy (TEM) used in the previous chapter, are used to characterize the interfaces of these NR heterostructures (NRHs) revealing the cause of the strain-induced curvature. Linear NRHs, where the CdTe only grows out

of the tips of the CdSe NR seeds, are also synthesized for comparison.

3.1 Synthesis of CdSe NR seeds

Anisotropic CdSe/CdTe NCHs are formed in a single pot starting with CdSe NR seeds which are first synthesized by arrested precipitation similar to previous reports [25, 58] where Se dissolved in trioctylphosphine (TOP) is rapidly injected into a Cd precursor containing solvent at elevated temperature (Figure 3.1). The Cd precursor is formed by the dissolution of CdO by octadecylphosphonic acid (ODPA) to form ODPA-Cd in the presence of the polar trioctylphosphine oxide (TOPO) solvent. Twice the molar amount of Cd is present in the reaction flask as the amount of Se injected thus we expect that roughly 50% of the ODPA-Cd precursor is left over from the synthesis of the seeds. Once the seed NRs are formed (takes ∼15min from injection), Te dissolved in TOP is slowly added directly to the hot reaction mixture containing the seeds. The excess ODPA-Cd complex leftover from the seed synthesis provides the Cd source for CdTe formation. The details can be found in the methods section of this chapter.

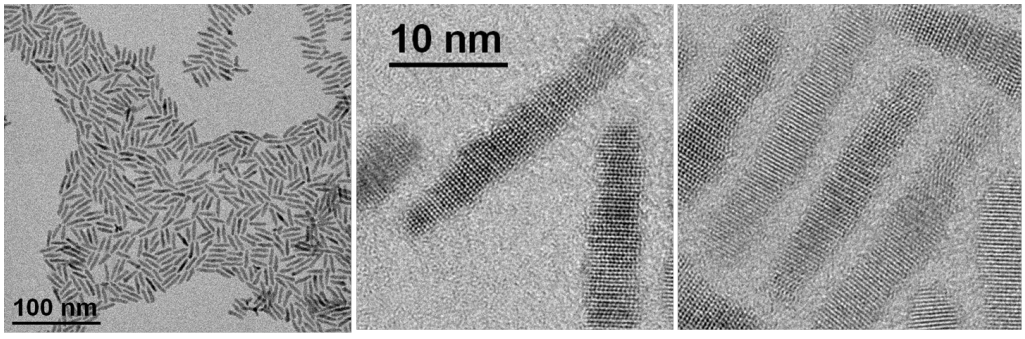

Figure 3.1: TEM images of CdSe seed NRs at low and high magnification. The scale is the same for the center and right images.

The reaction conditions, Te precursor injection rate and temperature

in particular, are optimized to prevent homogeneous nucleation of CdTe. As was the case with the Fe_3O_4/CdS NCH system, the injection rate can often determine the effective reagent concentration which is critical because at high reagent concentrations, homogeneous nucleation may begin to compete with heterogeneous nucleation. Within exclusive heterogeneous nucleation regime, Te reagent injection rate and injection temperature effect how CdTe grows on the seed CdSe NRs.

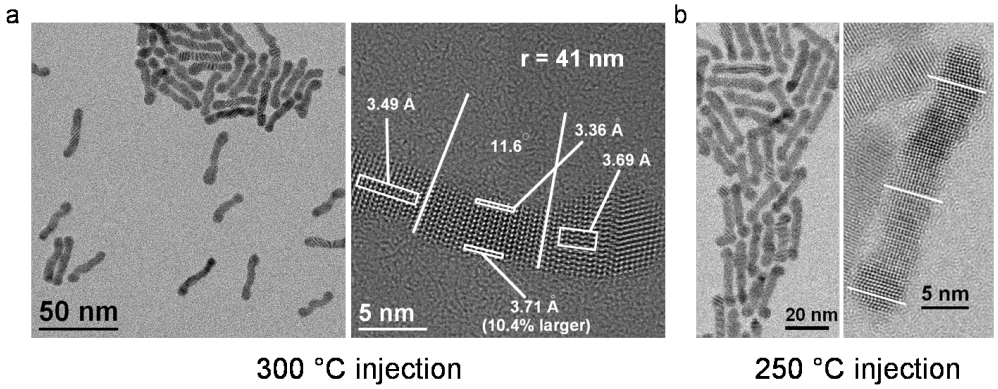

Figure 3.2: **a,b,** TEM images of CdSe/CdTe heterostructures of curved (**a**) and linear (**b**) shapes. The curved shapes arise from partial deposition of CdTe on the sides of the seed NRs. The linear shapes, obtained by nucleation and growth of CdTe at a lower temperature, consist of CdTe only at the tips.

3.2 Synthesis of curved and linear NRHs

Figure 3.2 shows two distinct structures that arise with a change in the injection temperature from 300 to 250 °C. At the lower Te injection temperature, exclusive tip growth is observed leading to linear or "barbell" structures. With increasing injection temperature above ∼270 °C, nucleation and growth occurs on the sides of the seed NRs as well. We hypothesize that growth of CdTe on the sides of the seed NRs gives rise to the observed curvature in the NCHs resulting from anisotropic stress of the

larger lattice constant CdTe being deposited. This suggests that an unusual combination of tensile and compressive strain exists in the seed NRs. Regardless of the final spatial distribution of CdTe on the seed CdSe NRs, both the linear and curved NRHs should exhibit significant strain due to a substantial lattice mismatch of ∼7 % between the two bulk lattice constants of CdSe and CdTe (larger). The importance of this expected lattice mismatch is often mentioned in the literature dealing with NCHs [60] but rarely elaborated on. Few reports have characterized the nature of this strain and what effects it has on both the synthesis and properties of NRHs.

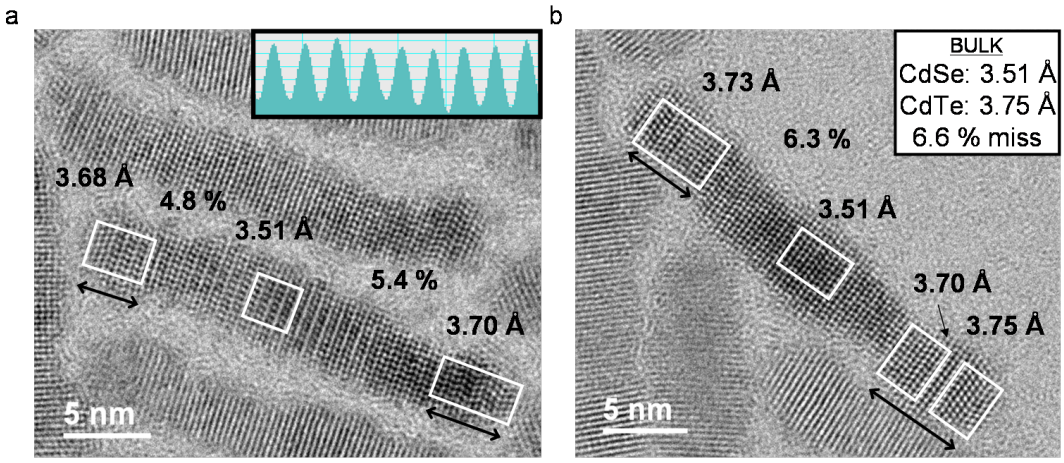

Figure 3.3: **a,b,** High resolution bright field transmission electron micrographs of CdSe/CdTe linear NRHs with ∼half (**a**) and the full (**b**) amount of CdTe deposited on the seed CdSe NRs. The full case is ∼50% CdTe, 50% CdSe. Double headed arrows indicate the approximate size of the CdTe regions. Averaged lattice spacings of the boxed regions using an integrated line scan (inset of **a**) are also indicated for comparison to the bulk values (inset of **b**).

3.3 Analysis of strain in NRHs using TEM

Figure 3.3 shows TEM images of linear CdSe/CdTe NRH during the growth of CdTe with measured lattice spacings in the CdSe and the CdTe regions.

It appears that the depositing CdTe initially adopts the lattice constant of the CdSe NR seed, with a high degree of compressive strain (note 3.68 Åis observed vs the bulk value of 3.75 Å). However, since we have not resolved the actual interface, nor its abruptness, we can not rule out the possibility that part of the seed is being included in this measurement. If the initially deposited CdTe is under a large degree of strain, we expect that as the CdTe domain grows in size it approaches its bulk lattice constant because eventually the bulk value (3.75 Å) is reached at the tip of the NRH.

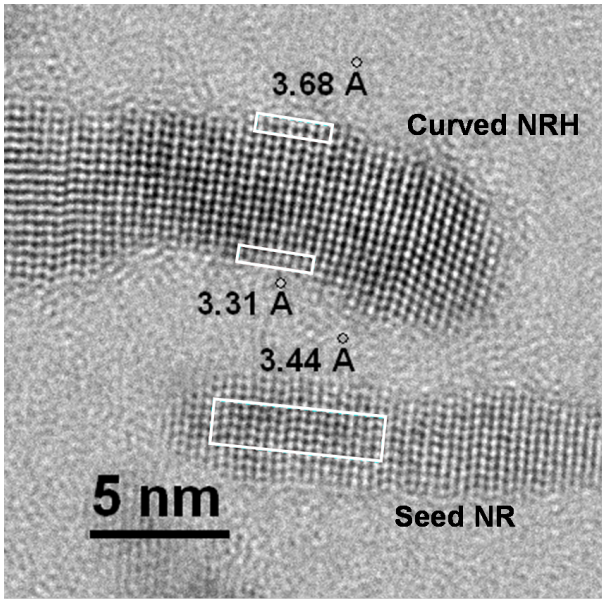

Figure 3.4: High magnification TEM image of both a CdSe NR seed (bottom) and curved CdSe/CdTe NRH (top) side by side. The uncalibrated, integrated average, raw d-spacings (c/2 lattice constant) are shown in the boxed regions shown. In addition to the direct observation of 3.8% strain in the CdSe portion of the NRH, this image demonstrates an error of roughly 2% in the uncalibrated measurements with the microscope on that particular day. In all other figures, the shown lattice constants and distances have been calibrated such that CdSe NR seeds have the appropriate bulk lattice constant.

We point out that distances measured in a TEM can vary slightly with the TEM alignment, magnification and instrument calibration. In the microscope used for most images in this thesis, the raw measured values

typically underestimated distances by 2- 5% based on statistical assessment of CdSe NRs (see Figure 3.4). In order to correct for this we carefully aligned the microscope at the beginning of a TEM session and started by taking TEM images of CdSe NR seeds which were used to determine the "multiplication" factor for all distances in TEM images taken during a given session. All measured lengths, widths and lattice constants were adjusted from the raw values to correct for the off calibration of the TEM. As a side note, all measurements were taken with the objective defocus zeroed (DV = 0 or "standard focus"). Calibration was done separately at different magnification if needed although typically lattice measurements were only conducted at the highest possible magnification of 600kX.

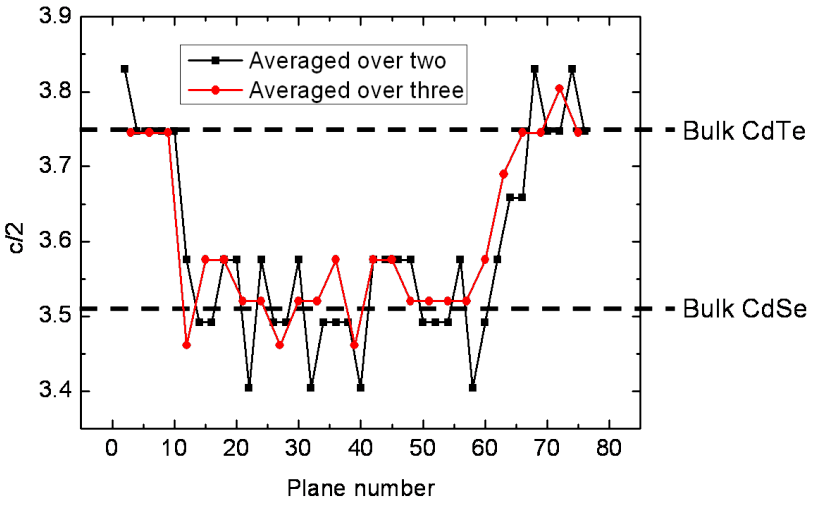

Figure 3.5: Calibrated measurements of the c-axis lattice constant measured along the length of the linear NRH shown in 3.3b are shown. In order to reduce the standard deviation in the measurements, the lattice constants have been averaged over two (black) and (three) fringes. Note that lattice constants in other images are averaged over at least five fringes. Bulk lattice parameters are noted by the dashed lines.

Figure 3.5 shows the d-spacings for the linear NRH in Figure 3.3b across the entire length of the structure. Since the resolution is not high

enough to get reasonable measurements of a single lattice fringe, averages have been taken across two and three lattice fringes. Doing this averaging greatly reduces the deviations in the measurement but results in a loss of junction resolution. Using TEM alone we measure the change in the lattice constant to be abrupt within this limit of 3-5 lattice planes. This method is probably effective at determining average lattice constants over a region away from the interface, as well as roughly resolving the location of the interface, but it fails to resolve the abruptness of the interface chemically. Furthermore, since we don't know how abrupt the interface is chemically we can not use this technique alone to resolve the spatial distribution of strain. That is, we can not effectively say whether the change in lattice constant is associated with strain or an alloyed region (using TEM alone).

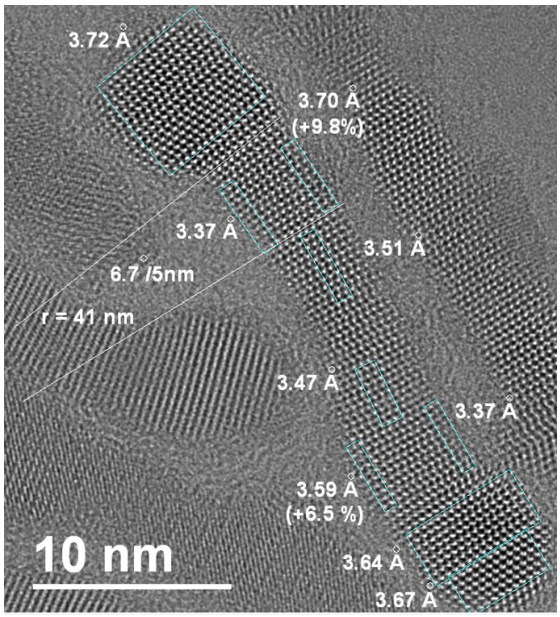

Figure 3.6: High resolution TEM image of a characteristic curved NRH having an "integral" shape. Lattice constants (calibrated) measured at various places (boxed regions) in the structure and are shown.

For comparison, another calibrated TEM image of a curved NRH in which (0002) lattice spacing over the entire NRH is mapped is shown in

Figure 3.6. This "integral" shaped NRH, with two opposing curvatures separated by an inflection point, was the most commonly observed shape. Interestingly, the larger tip (top) more closely matches the bulk value for CdTe and induces a smaller radius of curvature for the top half of the NRH as compared with the bottom tip. This observation agrees with the notion that CdTe initially adopts the CdSe seed lattice constant then approaches the bulk value as it grows larger. It was common to observe an asymmetry in NRH tips such that the increase in tip diameter occurs primarily on the inside edge of the curvature as seen here on both ends of this NRH.

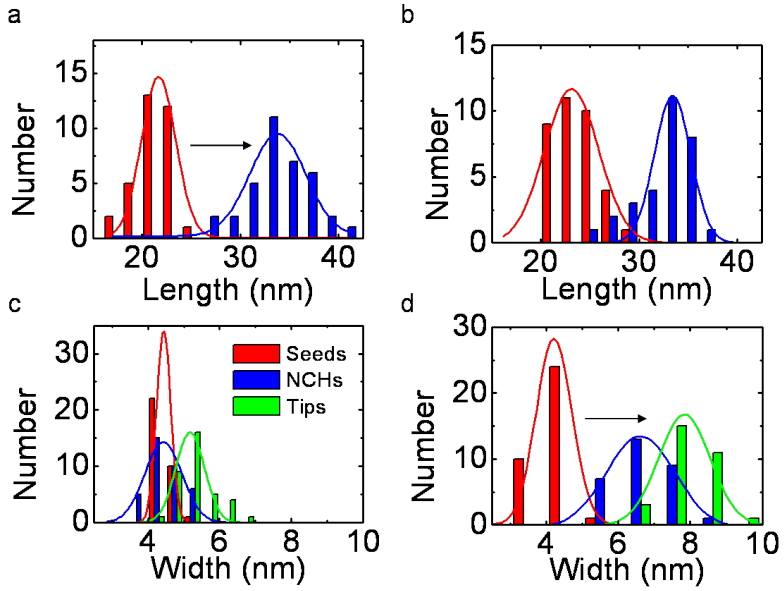

Figure 3.7: **a,b,** Length statistics (calibrated) for seeds (red), linear (blue in **a**) and curved (blue in **b**) NRHs. **c,d,** Central width statistics (calibrated) for seeds (red), linear (blue in **c**) and curved (blue in **d**) NRHs. Width for the tips of NRHs is also shown for each case (green).

In addition to lattice constant measurements, TEM can provide accurate characterization of NRH morphology (size statistics). The size statistics for linear and curved NRHs are compared with the starting CdSe NR seeds in Figure 3.7. The curved NRHs exhibit a significantly larger increase in their central width as well as at their tips (Figure 3.7d) but a

lesser increase in length (Figure 3.7b), compared to the linear NRHs. This observation supports our hypothesis about partial side growth of CdTe in the case of the curved NRHs.

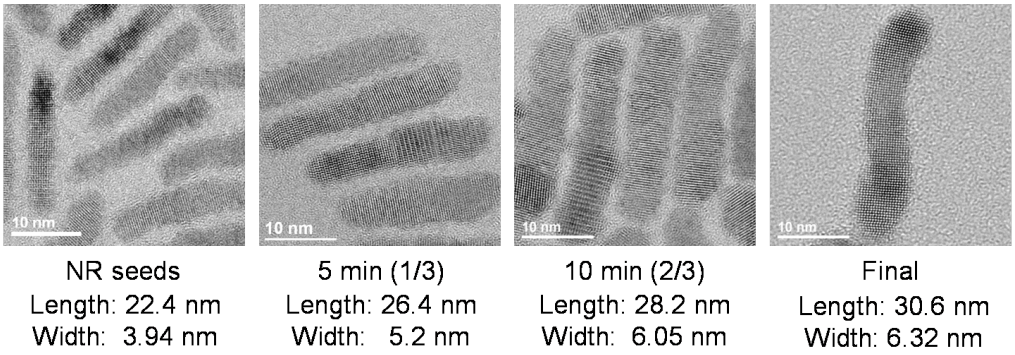

Figure 3.8: TEM images and average sizes (of ∼30 NRs/NRHs in each case) for curved NRHs at various stages of their synthesis depicting the gradual development of curvature. Widths are measured in the center of the NRHs.

When a statistical analysis of curved NRH sizes is carried out systematically during the deposition of CdTe (samples taken during TOP-Te injection), we find that the increase in width (and development of curvature is gradual (Figure 3.8). Again, this observation suggests that the curvature results from the growth of mismatched CdTe on CdSe NR seeds.

An X-ray diffraction (XRD) pattern for curved NRHs is shown along with their CdSe NR seeds in Figure 3.9. Note the sharp peak for the (0002) lattice spacing (c-axis (NR growth axis)) for the CdSe NR seeds (Figure 3.9a). The XRD pattern for the curved NRHs is significantly broadened and shifted towards a larger lattice constant compared with the seed NRs (Figure 3.9b). This broadening is consistent with the large distribution of lattice constants that we observe using TEM. The CdSe NR seed XRD pattern contains features that match reported CdSe wurtzite phase (Figure 3.9c) while the curved NRHs also exhibit features corresponding to CdTe zinc blende (3.9d) and wurtzite (3.9e) phases.

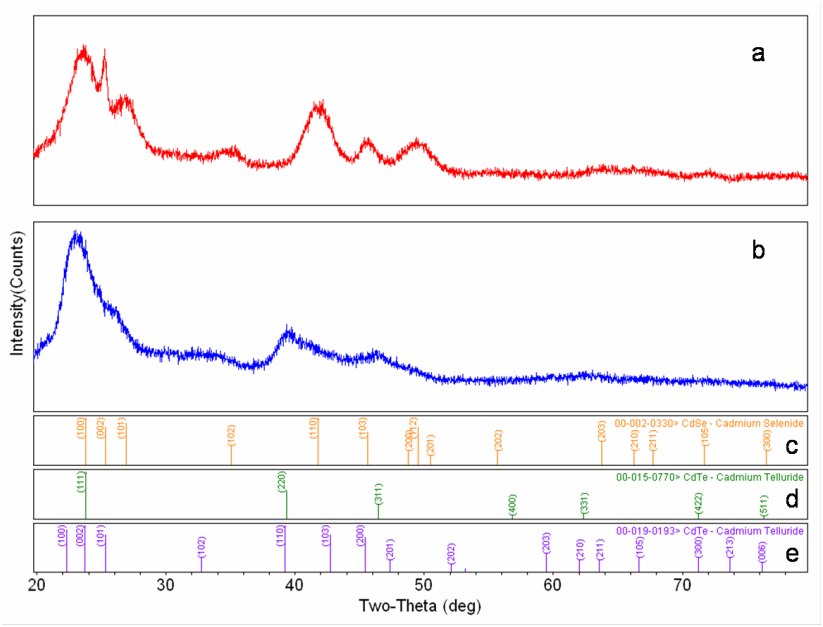

Figure 3.9: **a,b,** Powder XRD pattern measured from CdSe NRs (**a**) and curved NRHs (**b**). Reported XRD patterns for CdSe wurtzite (**c**), CdTe zinc blende (**d**) and CdTe wurtzite (**e**) phases are shown for comparison.

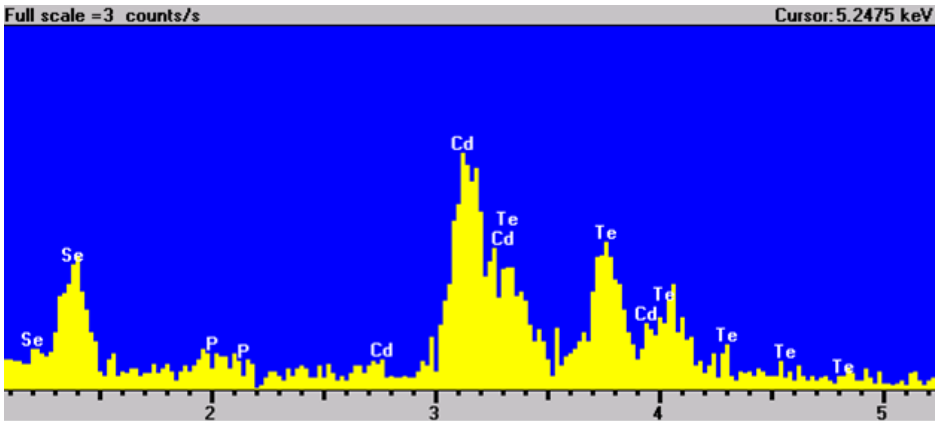

Figure 3.10: Wide area EDS pattern measured on curved NRHs. Semi-quantitative analysis of this data gave an elemental composition which was 50.3% Cd, 17.6% Se and 32.1% Te

Energy dispersive X-ray spectroscopy (EDS) confirms the presence of CdSe and CdTe in the curved NRHs, semi-quantitative analysis of this data gave a composition which was 50.3% Cd, 17.6% Se and 32.1% Te. While this appears to suggest that the structures contain more CdTe than CdSe, we expect Tellurium to be over counted here due to overlap with the

primary Cd peak. Further, analysis of the TEM size statistics for both linear and curved NRHs give a volume increase of ∼100% after CdTe deposition. Using EDS we can rule out the possibility that the large degree of strain is due to the presence of another chemical species.

Linear barbell structures (see Figures 3.2b and 3.3) with expected sharp heterointerfaces should provide an ideal or at least a simple geometry with which lattice strain in NCHs may be examined. However, surface/interface relaxation will alter the lattice constants at different locations of the NCHs and the same crystal structure between CdSe and CdTe makes it difficult to identify heterointerfaces at the atomic level. Obtaining selected area diffraction patterns at different locations of the NRHs not only lacks the desired spatial resolution but can also be difficult to interpret if there are lattice distortions due to interface strain. The main technique employed to date has been EDS mapping but it requires a large X-ray collection angle, often suffers from low signal-to-noise ratio, and lacks the desired atomic resolution [61].

3.4 Identification of the heterointerface using Z-contrast STEM

Using a high-angle annular dark field (HAADF) detector on an aberration corrected scanning transmission electron microscope (STEM), we are able to extract compositional information from ultra high resolution images. With the dark field detector we are counting scattered electrons as we raster the narrow beam spot across the sample. The scattering cross section for electrons with an element is proportional to the square of the atomic number (Z) thus, the technique gives rise to "Z-contrast." Figure 3.11 shows

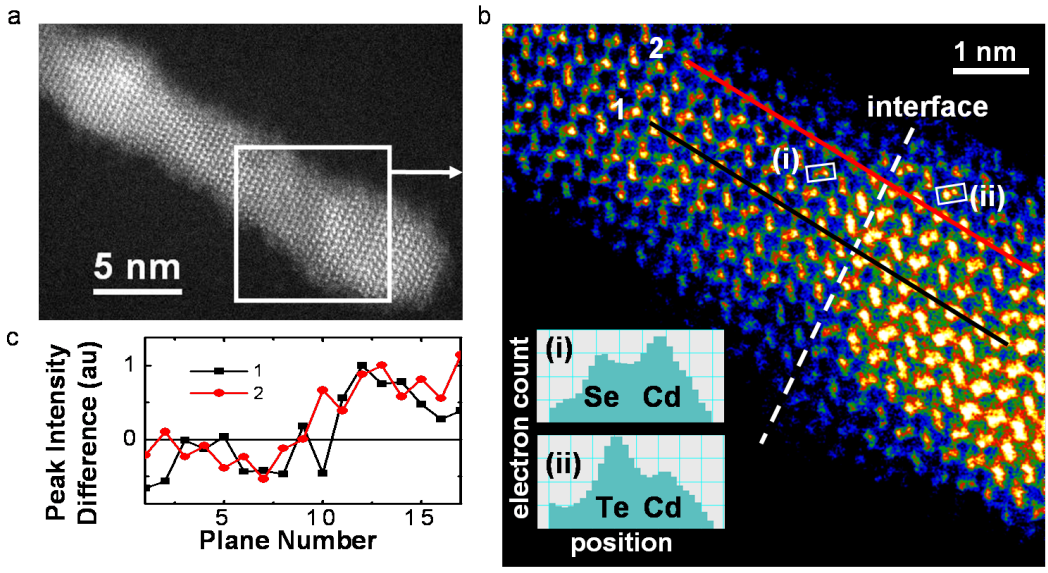

Figure 3.11: **a,b,** High resolution high-angle annular dark field scanning transmission electron microscope images of a linear barbell CdSe/CdTe NRH. Boxed region in (**a**) is magnified in (**b**). The inset in (**b**) corresponds to intensity profiles of the regions labeled (i) and (ii) revealing Z-contrast. Line scans of the intensity difference across the CdSe/CdTe interface (dashed line) along paths 1 (black line) and 2 (red line) are shown in (**c**).

a HAADF STEM image of a linear NRH at a low (3.11a) and high (3.11b) magnification with the heterointerface indicated by the dashed line. If the NRH is viewed along the $[1\,1\,\bar{2}\,0]$ zone axis (for wurtzite), the positions of all metal (Cd) atoms in a column line up with the beam (also all chalcogen (Se or Te) atoms in a column). Pairs of these columns of atoms are resolved as "dumbbells" in the image with one side being the metal column and the other side being the chalcogen column. The interface is easily observable both by an overall increase in the brightness ($Z_{Cd}+Z_{Se} = 82$ vs $Z_{Cd}+Z_{Te} = 100$) and more conclusively, by a contrast inversion of atomic pairs ($Z_{Cd}>Z_{Se}$ vs $Z_{Cd}<Z_{Te}$) seen in the Figure 3.11b inset. This Z-contrast between Cd and the chalcogen columns allows us to estimate the chemical sharpness of the heterointerface. The Z-contrast profile (measured as a change in the raw scattered intensity between each column in a "dumbbell") across the

interface in Figure 3.11c shows contrast inversion to be complete within ∼2 - 3 atomic steps. Given that the seed NRs are not likely to start with completely flat tips, we suspect the interface to be atomically sharp.

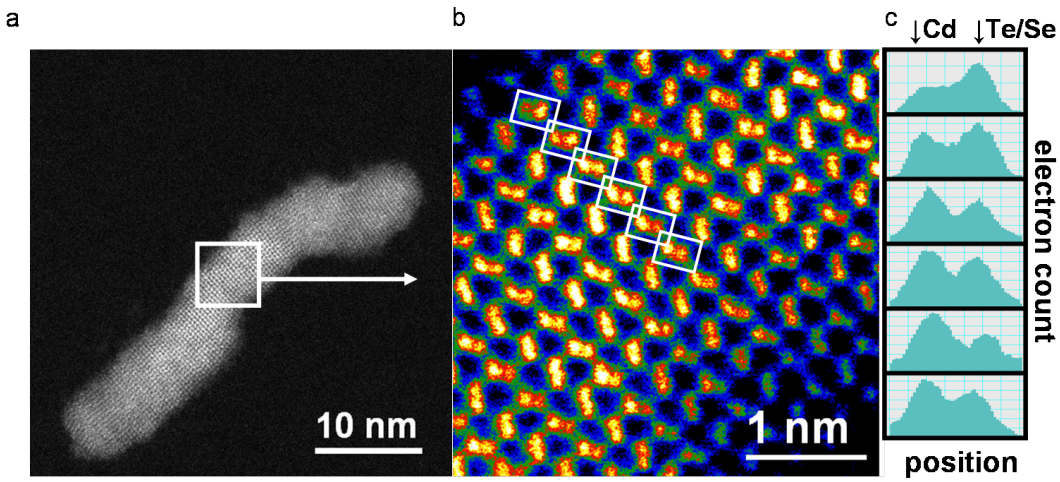

Figure 3.12: **a,b,** High resolution HAADF STEM images of a curved CdSe/CdTe NRH. Boxed region in **a** is magnified in **b**. Integrated line scans of metal-chalcogen pairs from the outlined regions in **b** are shown in **c**.

HAADF STEM images of the curved CdSe/CdTe NCHs we synthesized with a 300 °C TOP-Te injection temperature confirm our hypothesis that deposition of CdTe on the sides of the CdSe NRs is correlated with the curvature (Figures 3.12, 3.13a and 3.13b). Atomic pairs show contrast inversion from the outside of the curvature (where the lattice constant is largest) to the inside (where the lattice constant is smallest). High resolution TEM images in Figures 3.2a and 3.13c reveal that the curvature arises from an actual deflection in the lattice planes. Given the substantial mismatch between CdSe and CdTe, one would expect the lattice spacing to expand from the CdSe to the CdTe region. However, the lattice expands from the inside of the curvature to the outside much more than the bulk lattice mismatch. The expected (0002) lattice spacing difference between CdSe and CdTe is 6.6% (with respect to the smaller CdSe)

whereas we measure an expansion in Figures 3.2a and 3.13c of 10%. Lattice expansion as large as 13% has been observed. Through careful calibration of the TEM and images of mixed NRH with NR samples indicate that the CdTe portion of the NRH never expands beyond its bulk lattice constant (see Figure 3.4). Rather, the CdSe is under significant compression on the inside of the curvature, as high as ∼6%, in addition to the interface region which is under tensile strain, ∼3%.

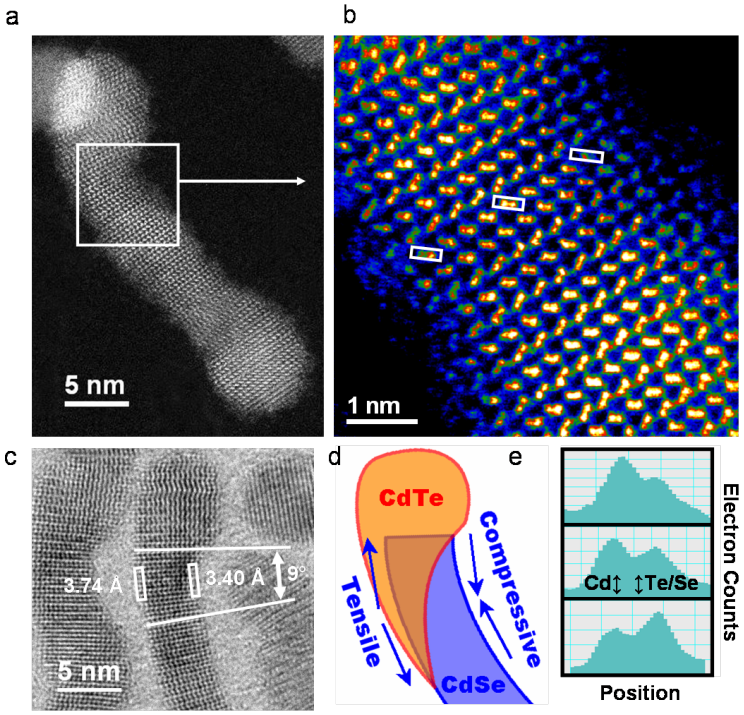

Figure 3.13: **a,b,** Additional high resolution HAADF STEM images of a curved CdSe/CdTe NRH. Boxed region in **a** is magnified in **b**. Line scans of the outlined regions in **b** are shown in **e**. **c,** High resolution TEM image of a curved CdSe/CdTe NRH. Angle of curvature and local lattice spacing of the boxed regions are indicated. Note, the bulk spacings are 3.51 Åand 3.75 Åfor CdSe and CdTe respectively. **d,** Schematic illustrating how CdTe deposition leads to tension and compression in the seed CdSe NR.

The emerging picture of the growth mechanism based on TEM and STEM analysis is as follows. A higher temperature injection activates side facet nucleation and growth of CdTe on CdSe NR seeds. Initially, the CdTe

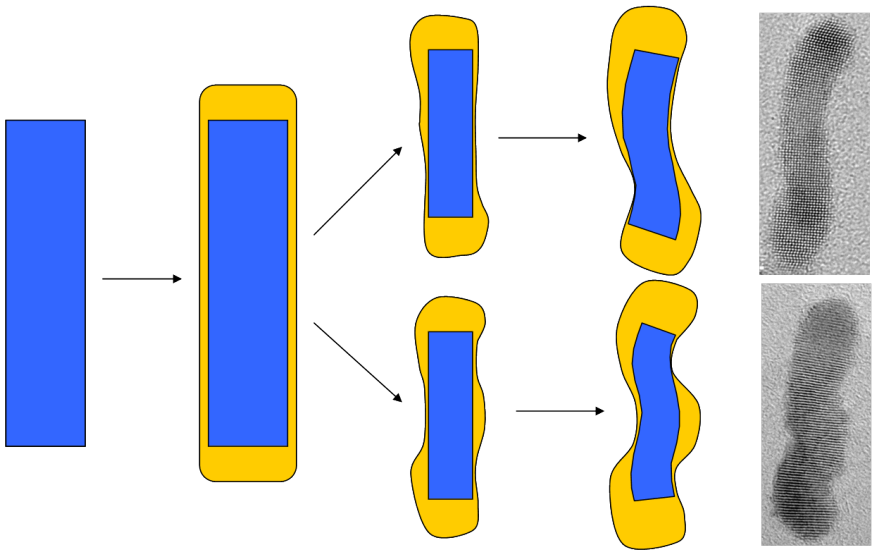

Figure 3.14: Schematic of curved NRHs at various stages of their synthesis depicting the mechanism for development of curvature. Two possible outcomes are shown demonstrating the sensitivity to early inhomogeneity of the CdTe shell on the final morphology.

deposits as a thin, highly strained shell. Either due to some small variations (asymmetries) in the CdSe seeds, or perhaps due to a Stranski-Krastanov-esq strain induced island formation, some regions of the growing CdTe shell on the NRH are thicker than others. These thicker regions exert a larger tensile stress on the sides of the CdSe NR seeds. This net stress on one side of the seed causes it to deflect or "curve" a little. As such, the opposite side of the seed is under compressive stress as it gets squeezed by the deflection. As additional CdTe deposits, it finds a poorer lattice match on the compressed side than on the thicker shell CdTe region side. This difference in lattice match makes it more favorable for CdTe to grow on the outside regions of the curvature, increasing the thickness in these already thicker regions, further promoting the curvature. In this way, a positive feedback mechanism develops to enhance the NRH curvature to the point where the depositing CdTe reaches its bulk lattice constant. This

process is outlined in Figure 3.14.

3.5 Optical properties of type II NRHs

In addition to the very apparent implications of strain for the synthesis of NCHs as seen in both the Fe_3O_4/CdS and the CdSe/CdTe systems, we expect that there should be significant modification to the band structure of these highly strained systems. This modification will be not only a change in the band gaps of the constituents spatially but will also give rise to differences in the conduction and valence band offsets at the interface. One indirect way to probe such changes is by looking at the optical properties of NRHs dissolved in a transparent solvent. Figure 3.15 compares the absorption and photoluminescence (PL) spectra of seed CdSe NRs with the linear (3.15a and 3.15c) and curved (3.15b and 3.15d) NRHs (blue and red) with the CdSe seed NRs (black). We expect the absorption band edge for CdTe of the tip sizes observed with TEM to be ∼680 nm, therefore the absorption tail beyond 680 nm is attributed to charge separated state (CSS) absorption and is typical of type II NCHs [32]. Both the curved and linear NRHs exhibit this tail but the curved NRHs seem to have an enhanced effect. A higher degree of CSS absorption in the curved structures could arise from an increase in the interface area that we would expect from the growth of CdTe on the sides of the seed NRs and may be beneficial for absorption of lower energy solar photons.

The linear NRHs have a typical, large Stokes-shifted, PL beyond the expected PL of CdTe band edge that is commonly observed in core/shell type II NCHs [32]. This PL arises from CSS recombination but the quantum yield of is about 100 times lower than the PL from the CdSe seed

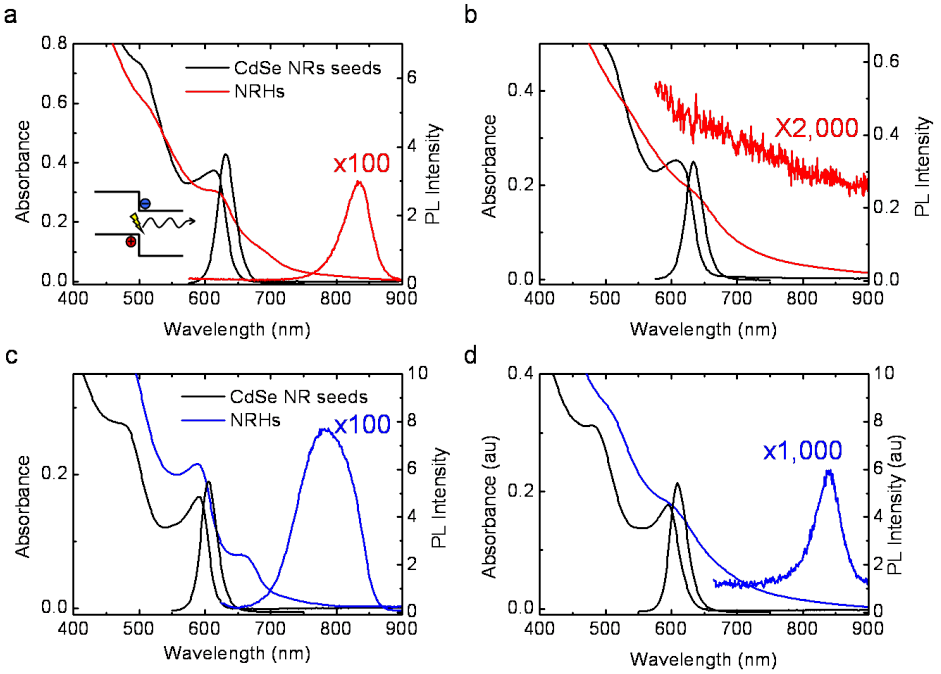

Figure 3.15: **a,b,c,d,** Absorption and photoluminescence spectra of the linear (**a,c**) and curved (**b,d**) CdSe/CdTe NRHs along with corresponding spectra of seed CdSe NRs. Spectra of the seeds are shown in black and those of the NRHs are in blue and red. The bottom two batches (blue) were synthesized from a different recipe to produce slightly smaller seeds which had higher PL intensities and narrower size distributions (note sharper peaks in the absorption). See the methods in Chapter six for details on the sysnthesis of these NRHs. PL spectra have been scaled to make the features observable on the same scale. The schematic (inset of **a**) demonstrates the CSS recombination that the observed PL in type II NRHs arises from.

NRs. It has been shown previously, using time resolved PL, that CSS PL in type II NCHs can exhibit long decay times, as high as 100µs at room temperature [62]. In contrast to the linear NRHs, the curved structures show a complete quenching of the PL. The lack of, or a greatly reduced, CSS PL in curved NRHs provides an argument for enhanced physical charge separation, in other words, reduced electron/hole wave function overlap. An alternative explanation may be that the higher interface area and closer interface proximity to the crystal surface promote recombination which competes with the CSS PL (radiative) recombination. While PL is

an indirect method of characterizing band structure, these results are a preliminary indication that the energy landscape for charges is different in these two structures. We note that using a modified synthesis, it is possible to produce smaller sized CdSe seeds. Using smaller sized seeds we do observe a very weak PL from the curved NRHs (Figure 3.15d). However, the PL from curved NRHs synthesized from the same size seeds as linear NRHs is always at least an order of magnitude lower in quantum yield (brightness) and also longer in peak wavelength than the linear NRHs.

The linear and curved CdSe/CdTe NCHs presented above demonstrate the ability to control the location of CdTe growth on the seed CdSe NRs which can in turn provide us with the ability to manipulate spatial distribution of lattice strain in these NRHs. This may lead to new approaches to band structure engineering especially useful for directing charge carriers in photovoltaics. Further, the formation of a type II interface, and perhaps the increase in that interface area, promotes CSS absorption at longer wavelengths than the isolated components of the NRH. CSS absorption may not only tune absorption to the solar spectrum but could potentially generate carriers without paying the energy penalty (or as large of a penalty) of exciton dissociation. That is, carriers absorbed at the interface come already dissociated but it is unclear how much Coulombic energy would still be associated with these charges. More work is needed to determine if CSS absorption can actually enhance the photo-current of a solar cell (see Chapter 6).

3.6 Methods

3.6.1 General considerations

The single pot reactions were carried out in a standard Schlenk line under N_2 atmosphere. Technical grade trioctylphosphine oxide (TOPO) (90%), technical grade trioctylphosphine (TOP) (90%), CdO (99.5%), Se powder (99.99%), and Te powder (99.9%) were obtained from Sigma Aldrich. ACS grade chloroform, methanol, butanol, and toluene were obtained from Fischer Scientific. N-octadecyl phosphonic acid (ODPA) was obtained from PCI Synthesis. Materials were used as received.

3.6.2 Synthesis of CdSe NR seeds

First, 2.5 g (6.5 mmol) of TOPO, 1.73 g (5.2 mmol) of ODPA and 0.333 g (2.6 mmol) of CdO were added to a 50 ml three-neck round-bottom flask. The reaction mixture was then degassed at 150 °C for 1 h under vacuum with occasional N_2 purges. The reaction mixture was then heated to 300 °C under vigorous stirring to form ODPA-Cd complex until the solution became transparent and colorless, typically after 1 h. The solvent was cooled to 150 °C and degassed for an additional 10 min to remove O_2 and H_2O produced during complexation. At 320 °C under N_2, a solution containing 0.1023 g (1.3 mmol) Se dissolved in 1.6 g (4.3 mmol) TOP and 0.3 g toluene was swiftly injected. The reaction mixture was quenched to 260 °C where the growth was carried out, the solution changes color from light red to dark maroon over this period. After 15 min at 260 °C, the reaction mixture was rapidly cooled to 100 °C where an aliquot of the seed CdSe NRs was taken for analysis. Subsequent growth of CdTe was carried

out by addition of Te reagent to the same reaction vessel maintained under N_2 as described below.

3.6.3 Synthesis of Curved CdSe/CdTe NRHs

Following the formation of CdSe NR seeds, the reaction mixture was heated to 300 °C where 1.3 ml of 1 M trioctylphosphine telluride (TOPTe) diluted with 4ml of TOP was injected at a rate of 20 ml/h via syringe pump (total injection time ∼16 min). The reaction mixture was aged for an additional ∼5 min at 300 °C before the heating mantle was removed and the reaction flask was rapidly cooled by air jet. Upon completion of reaction, the final product was cleaned by precipitation with methanol (80%) and butanol (20%), then stored as a solution in chloroform under N_2 atmosphere.

3.6.4 Synthesis of Linear CdSe/CdTe NRHs

Following the formation of CdSe NR seeds, the reaction temperature was adjusted to 250 °C at which point 1.3 ml of 1 M TOP-Te diluted with 4ml of TOP was injected at a rate of 20 ml/h via syringe pump. The reaction mixture was aged for an additional ∼5 min at 250 °C before the heating mantle was removed and the flask was rapidly cooled by air jet. Cleaning and storage procedures were same as described for the curved NRHs.

3.6.5 TEM/STEM

Transmission electron microscopy (TEM) samples were prepared on Cu grids with thin carbon film from a dilute solution (optical density ∼0.2 at ∼ 600nm of NCs in chloroform. TEM analysis was carried out with a JEOL 2100 TEM operating at 200 kV. Additional TEM and HAADF STEM

analyses were carried out with a JEOL 2200 aberration corrected STEM/TEM operating at 200 kV.

3.6.6 Absorption and photoluminescence

UV-vis absorption spectra were obtained with an Agilent 8453 photodiode array spectrometer. Photoluminescence spectra were collected with a Horiba Jobin Yvon FluoroMax-3 fluorometer.

3.6.7 XRD and EDS

Rigaku Geigerflex with the D-MAX system was used for the acquisition of powder X-ray diffraction patterns. EDS analysis was carried out with a JEOL 2010f STEM operating at 200 kV.

CHAPTER 4

ALLOYED TYPE II NANOROD HETEROSTRUCTURES

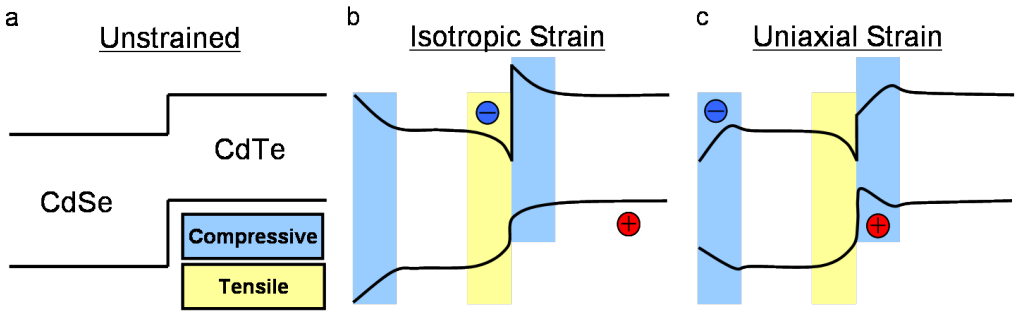

Figure 4.1: **a,b,c,** Schematics depicting the approximate CdSe/CdTe heterojunction unstrained (**a**), isotropically strained (**b**) and the potential effects of axial strain based on recent theoretical modeling (**c**). The magnitude of the strain effects shown, particularly in the valence band where the effect would be small, are not to scale and would depend on various factors. Excited electrons (negative blue circles) and holes (positive red circles) are added to demonstrate how the locations of lowest energy states could vary depending on the effect of strain. As noted, compressive regions are in light blue while tensile regions are in light yellow.

While it is clear that strain has large implications on the synthesis of NRHs, it is less clear exactly how the band structure is affected. We have seen evidence for charge separation across the type II heterojunction in the absorption spectra of linear and curved NRHs (charge separated state (CSS) feature); however, if the curved NRHs exhibited any PL at all, it was at least an order of magnitude lower in quantum yield and red shifted from the PL peak of the linear NRHs. We observed a very different strain field in the curved than the linear NRHs, so its conceivable that the difference in PL can be attributed to strain effects. Figure 4.1 qualitatively compares

the unstrained (Figure 4.1a) and intuitively (isotropically) strained (Figure 4.1b) band structure for the CdSe/CdTe heterojunction. One possibility for reduced PL quantum efficiency in the curved NRHs is that the strain is reducing the electron/hole wavefunction overlap by driving carriers away from the junction.

According to recent computational studies on uniaxial (along the rod axis direction) strain in the CdSe/CdTe system, the effect of strain on the band structure of NCHs can be similar in magnitude to quantum size effects [63]. Further, intuitive ideas based on isotropic strain (Figure 4.1b) about band bending due to strain near the heterointerface may not only be wrong in magnitude but also in sign [47, 64]. According to these recent studies, uniaxial tensile strain on CdSe and CdTe reduces the band gap as expected but uniaxial compressive strain is predicted to increases the band gap only at very small strains. At higher uniaxial compressive strain, but still below the equilibrium interfacial strain ($\sim$3.4% on each side), band gap is predicted to decrease. Whether or not such effect is occurring or beneficial for photo-induced charge separation is unclear. The next step towards the goal of engineering NRHs for useful photon harvesting is to understand the role that strain plays in the band structure of these materials. Ultimately, we would like to tune strain to promote charge separation in NRHs. In order to do so, we must first develop synthetic strategies for a systematic variation of strain in NRHs and also develop techniques for characterizing these structures.

4.1 CdSe/$Cd_xZn_{1-x}Te$ NRHs

CdSe and ZnTe are almost perfectly lattice matched (0.8%) with one another and exhibit a type II bulk band alignment. It was expected that synthesis of CdSe/$Cd_xZn_{1-x}Te$ NRHs would be similar to synthesis of CdSe/CdTe NRHs except a Zn precursor would be co-injected with the TOP-Te precursor to form the second component. In order to systematically vary strain, one would tune the the Cd:Zn ratio from 0% to 100% in the secondary component to vary the strain from 0.8% to 6.7%. Since the valence band of ZnTe and CdTe (highest occupied molecular orbital of the entire NRH) are similar, and since the seed would remain constant in the study (lowest unoccupied molecular orbital of the NRH would also remain fixed, strain aside), this system could provide an effective strategy to separate out the effects of strain on the band structure.

In the initial attempts to form non-alloyed CdSe/ZnTe we added a mixture of Et_2Zn and TOP-Te directly to the reaction mixture following CdSe NR seed synthesis at 250 °C as with the linear CdSe/CdTe NRHs. The synthesis recipe was modified to have roughly half the amount of Cd, which was expected to be fully consumed in the seed synthesis, and to leave none (or very little) for reaction with TOP-Te (see methods). This resulted in homogeneous nucleation of the second component. Because Et_2Zn is particularly reactive, we lowered the injection temperature of the ZnTe precursors. At ∼170 °C the reaction resulted in nearly 100% heterogeneous nucleation of the second component, primarily at the tips of the CdSe NR seeds, as seen in Figures 4.2a and 4.2d. The absorption resembled the broad absorption tail into the red region of the spectrum of the curved NRHs seen in Figures 3.15b and 3.15d indicating a type II heterojunction

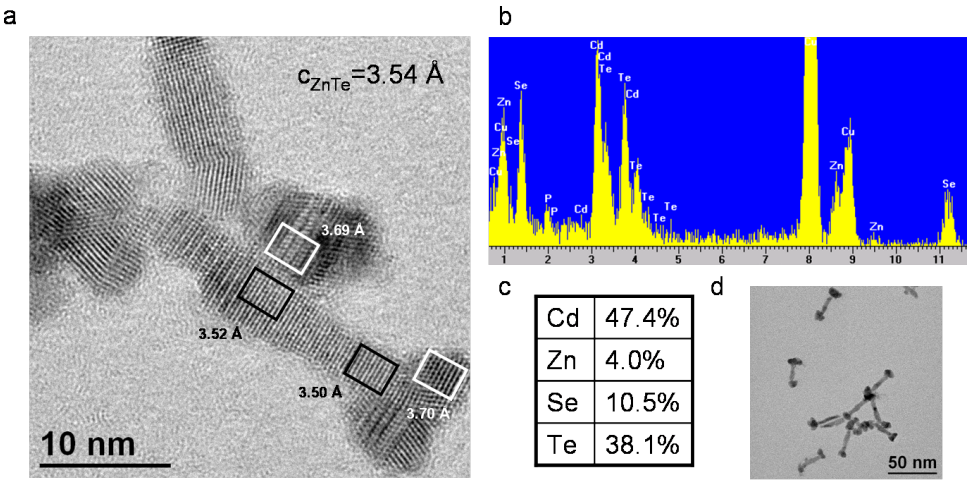

Cd	47.4%
Zn	4.0%
Se	10.5%
Te	38.1%

Figure 4.2: **a,d,** High (**a**) and low (**d**) magnification TEM images of CdSe seeded $Cd_xZn_{1-x}Te$ in a single pot synthesis. Average lattice constants measured with integrated line-scans in the boxed regions of the expected CdSe seed (black) and second component (white) are shown. The ZnTe lattice constant is given for comparison (CdSe lattice constant is nearly the same, 0.8% lower). **b,** EDS measurements while the beam is focused on an entire NRH are shown with the x-axis energy of captured x-rays in keV and the y-axis is x-ray counts. **c,** Elemental composition calculated from the integrated area of the EDS peaks are given.

had likely formed. Also like the curved NRHs, the PL of the CdSe seeds was completely quenched upon injection of the ZnTe precursors with no new peak appearing. Upon closer inspection of TEM images, it was revealed that the lattice constant in the second component was both non-uniform and too large to be primarily ZnTe. Further analysis via wide area energy dispersive x-ray spectroscopy (EDS) revealed that very little Zn was present in the material (Figure 4.2b and 4.2c). We hypothesized that the highly reactive Et_2Zn was somehow activating left over ODPA-Cd complex to form mostly CdTe as the second component. This was quite surprising because attempts to grow CdTe NRs and CdSe/CdTe NRHs at temperatures below 200 °C failed. A single pot approach to forming CdSe/ZnTe may not be possible since ODPA-Cd precursor will be undoubtedly leftover from the CdSe seed NR synthesis.

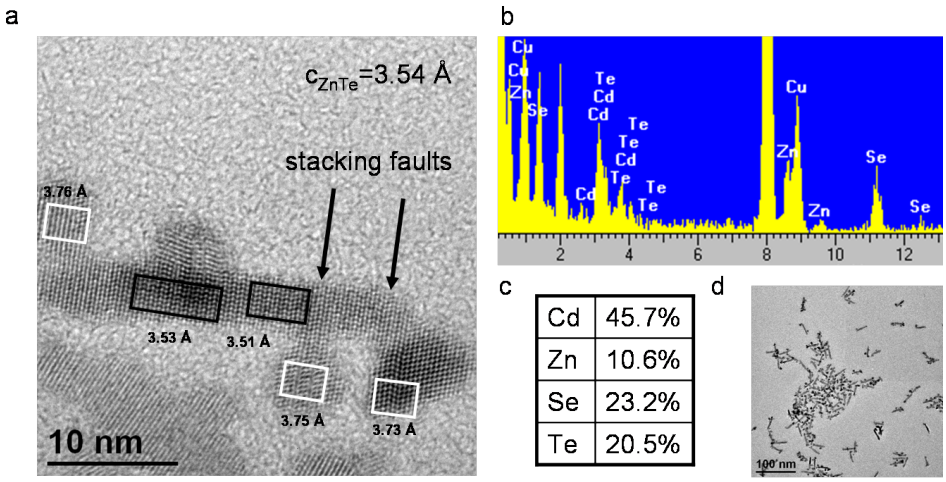

Figure 4.3: **a,d,** High (**a**) and low (**d**) magnification TEM images of CdSe seeded $Cd_xZn_{1-x}Te$ in a separate pot after cleaning. Average lattice constants measured with integrated line-scans in the boxed regions of the expected CdSe seed (black) and second component (white) are shown. The ZnTe lattice constant is given for comparison. Stacking faults in the CdSe NR seed are noted. **b,** EDS measurements while the beam is focused on a NRH tip are shown with the x-axis energy of captured x-rays in keV and the y-axis is x-ray counts. **c,** Elemental composition calculated from the integrated area of the EDS peaks are given.

In order to control the incorporation of Cd into the second component, we synthesized CdSe NR seeds then cleaned them to remove any excess ODPA-Cd complex. Special care was taken during cleaning to separate excess leftover ODPA-Cd complex. This ODPA-Cd complex has nearly identical solubility as the ODPA/TOPO passivated CdSe NRs but it tends to aggregate in chloroform and has a lower density. Ultra centrifugation helps to separate ODPA-Cd complex from a solution of CdSe NRs dissolved in chloroform as it aggregates and rises during centrifugation, although an ultracentrifuge was not used at this time. This approach initially failed to produce NRHs when we used TOPO and OPDA as reaction solvents/capping agents (same as previously) and more work is needed to understand the problem with using ODPA as a solvent when Et_2Zn is desired as the Zn precursor. It would appear that there is a strong

affinity for ODPA to complex with Zn and prevent the formation of ZnTe (under these conditions). After trying a number of coordinating and non-coordinating solvents typically used for colloidal II-VI NC synthesis (including heptadecane, octadecene, octadecylamine, hexadecylamine, oleic acid and octyl ether), a mixture of TOPO and oleylamine was found to form the NRHs seen in Figures 4.2a and 4.2d from CdSe NR seeds using Et_2Zn and TOP-Te as ZnTe precursors. Surprisingly, the second component in these materials still had lattice constants that were too large too be pure ZnTe (Figure 4.2a). Interestingly, the second component was found to be almost entirely of the zinc blende phase and tended to nucleate near stacking faults in the CdSe NR seeds as seen in Figure 4.2a. This observation is consistent with zinc blende being the ZnTe equilibrium phase [65]. With the electron beam focused near the second component of NRHs, EDS revealed that while more Zn was present than previously, the ratio was still less than expected.

We have used EDS here as a first estimate of NRH composition, but EDS lacks the spatial resolution to spatially map composition effectively on the NRH size scale. However, coupled with measurements of lattice constant using TEM, we tentatively conclude that the second component was in fact CdTe rich. We suspect that either significant OPDA-Cd complex persists with the CdSe NRs even after extensive cleaning or that oleylamine partially dissolves the CdSe NR seeds to provide the Cd precursor for reaction with TOP-Te. A $Cd_xZn_{1-x}Te$ component is likely present in these structures, however, systematically controlling this composition is likely to be difficult.

4.2 Tuning the composition in $CdSe/CdSe_xTe_{1-x}$ NRHs

Because we ultimately could not grow pure ZnTe on CdSe NRs, the $CdSe/Cd_xZn_{1-x}Te$ system was determined inadequate for a systematic study of strain through alloying. We tried various single pot and multi-pot strategies to make non-alloyed CdSe/ZnTe and always encountered a CdTe rich second component. Having had success synthesizing non-alloyed CdSe/CdTe previously, as an alternative way to systematically modify the type II heterointerface, we investigated $CdSe/CdSe_xTe_{1-x}$ alloyed NRHs.

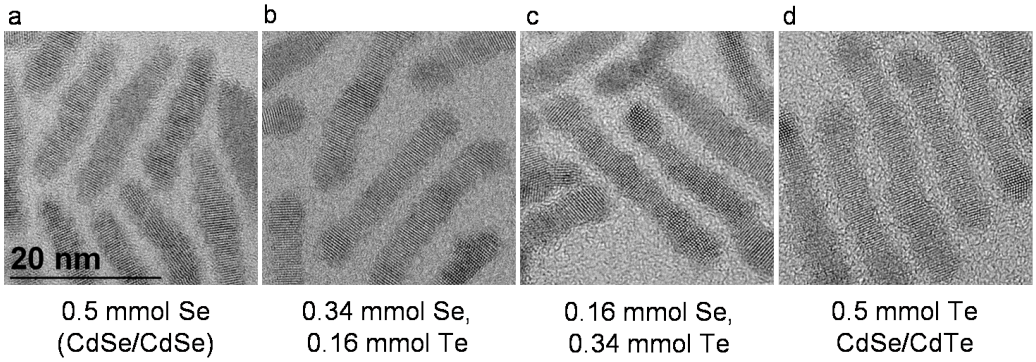

Figure 4.4: **b,c,** High magnification TEM images of initial attempts at forming $CdSe/CdSe_xTe_{1-x}$ NRHs using the a similar recipe as the linear CdSe/CdTe NRHs except with a 2:1 (**b**) and 1:2 (**c**) ratio of Se:Te precursor in the second (heterostructure forming) injection. **a,d,** High resolution TEM images of CdSe NRs (**a**)and CdSe/CdTe NRHs (**d**) synthesized with an identical recipe as **b** and **c** except only Se and Te were included in the second injection. The total molar amount of Se and Te is noted for each case.

Initially, we tried to use the same synthesis procedure as with linear CdSe/CdTe (non-alloyed) NRHs except we injected 2:1 and 1:2 mixtures of Se:Te (dissolved in TOP) into a hot reaction mixture containing the CdSe NR seeds and excess ODPA-Te in expectation of forming $CdSe/CdSe_{0.67}Te_{0.33}$ and $CdSe/CdSe_{0.33}Te_{0.67}$ NRHs. The absorption and PL of these cases were nearly identical to that of the non-alloyed linear

NRHs and TEM analysis indicated that the primary effect of increasing the amount of Te content in the second injection was to increase the length of the NRHs as seen in Figure 4.4. Statistical analysis of lattice constants in TEM images revealed that the second component was still far more CdTe rich than expected from the Te:Se precursor ratio. Bailey et al. reported the synthesis of $CdSe_xTe_{1-x}$ NCs under similar conditions and noted that the reactivity of Te towards Cd is "considerably higher" than Se and that as a result, the reaction rate of CdTe is roughly double that of CdSe [66]. Smith et al. similarly had difficulty in forming PbSe rich $PbSe_xTe_{1-x}$ alloyed NCs using TOP-Te and TOP-Se and ultimately used more reactive Se precursors [67].

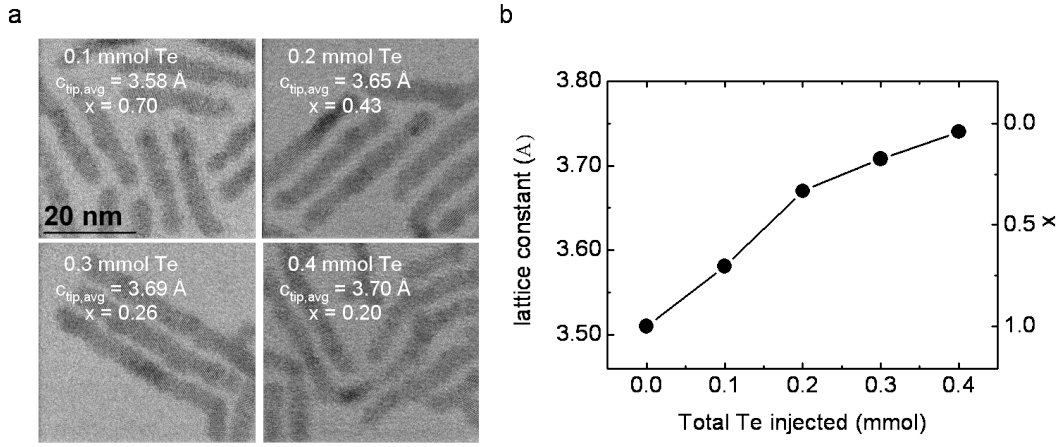

Figure 4.5: **a,** Characteristic TEM images of $CdSe/CdSe_xTe_{1-x}$ NRHs formed from a fixed (and excess) amount of Se (0.80 mmol) and various amounts of Te co-injected slowly. **b,** Average lattice constant measured in the tips (left y-axis) of the NRHs is shown along with composition assigned (right y-axis) from these measurements according to Vegard's Law.

Considering these relevant reports, we adjusted the synthesis in two ways. First, we injected the precursors very slowly to push the reaction to a concentration limited regime rather than a reaction rate limited regime so as to not form a graded composition as the TOP-Te precursor reacted and

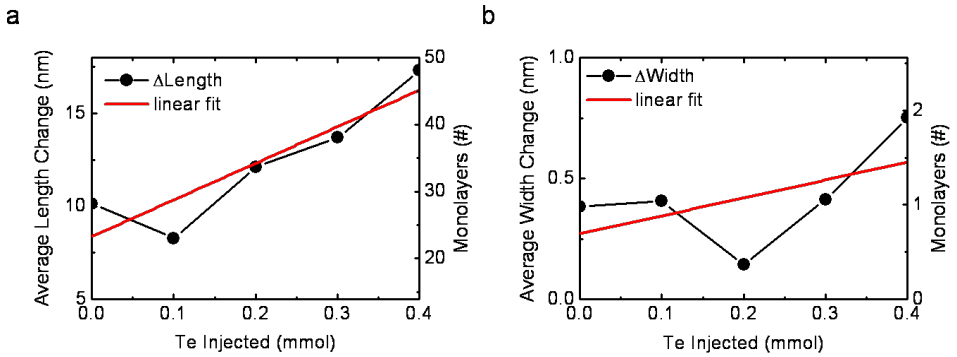

Figure 4.6: **a,b,** The average length (**a**) and width (**b**) of alloyed NRHs measured from TEM images as a function of amount of Te co-injected with a fixed amount of Se (0.80 mmol). The length and width increases in terms of monolayers is shown on the right y-axis of each figure. Linear fits are shown in red.

got used up more quickly. Second, we injected an excess and fixed amount of Se precursor (0.80 mmol) while varying only the amount of TOP-Te. We hypothesize that due to the lower reactivity of TOP-Se, the chemical yield of this precursor was lower than that of TOP-Te and thus, more Se is needed than Te to form equivalent amounts of CdSe and CdTe. Ultimately, by slow injection of Se and Te precursors with an excess of Se, we were able to achieve CdSe/$CdSe_xTe_{1-x}$ NRHs with controlled composition over the entire range of alloys (based on TEM analysis, see Figure 4.5). It is worth noting that because we used a fixed amount of Se and changed only the amount of Te, the total molar amount of precursor injected in the second step did change. As the total amount of precursor increased, the length of the NRHs also increased but the average width did not significantly change (see Figures 4.6a and 4.6b).

While varying the composition of alloyed NRHs, we monitored the absorption of the NRHs (Figure 4.7). The absorption peak associated with the CdSe 1s states (∼600 nm) did not significantly redshift following the deposition of the second component. However, as the composition was

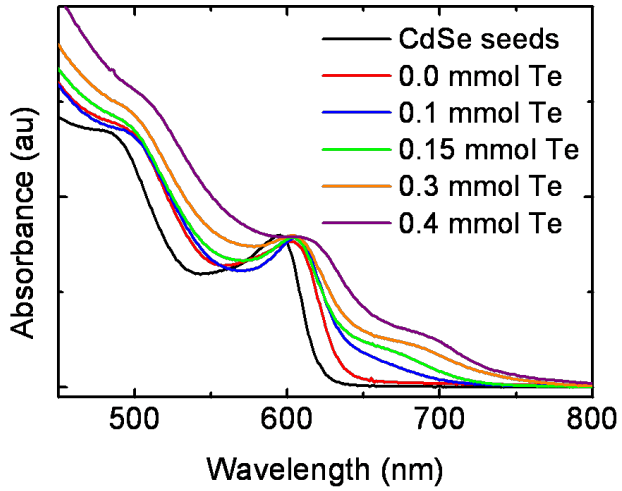

Figure 4.7: Absorption spectra of CdSe NR seeds (black) and various alloyed NRHs synthesized by varying only the amount of Te co-injected with TOP-Se. The absorption for the 0.15 mmol Te case (green) corresponds with the blue PL curve in 4.8a.

varied to increase the CdTe composition (decreasing x), a new shoulder appeared and shifted to the red. We attribute this shoulder to the $CdSe_xTe_{1-x}$ 1s excitation and the decreasing energy of this feature with increasing CdTe content (x decreasing) is consistent with a reduction in the band gap as a result of alloying.

The photoluminescence (PL) of the CdSe NR seeds at half way through Se/Te precursor injection and of the final products were also monitored. Figure 4.8a depicts the wide range over which the PL could be varied in these NRHs. To synthesize $CdSe/CdSe_{0.5}Te_{0.5}$ NRHs we used 0.15 mmol Te based on the results outlined in Figure 4.5b. As can be seen, the PL energy, which roughly estimates the energy of the heterointerface charge separated state (CSS), redshifts with increasing size (half to full injection) and with increasing CdTe composition (decreasing x). Both results are expected because reduced confinement in the second component should reduce the band gap and hence also the spatially indirect interface band

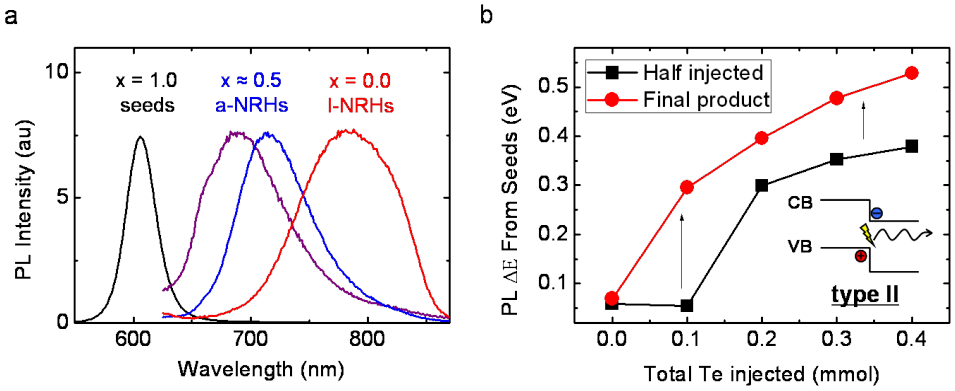

Figure 4.8: **a,** Photoluminescence of CdSe NR seeds (black), 50% alloy (blue) and non-alloyed (red) NRHs are shown. Also shown is the PL for the half injection point of the 50% alloy NRHs (purple). The PL intensities have been scaled to appear equal in magnitude. **b,** The change in PL peak energy as a function of Te amount injected (with a fixed amount of TOP-Se (0.80 mmol)) for half (black) and full (red) injection of the precursors to monitor the size effect on PL (half injection is smaller).

gap (difference between the CdSe conduction band and $CdSe_xTe_{1-x}$ valence band energies). Further, as the composition approaches the non-alloyed CdSe/CdTe case (x = 0.0), the $CdSe_xTe_{1-x}$ valence band position increases which reduces the spatially indirect interface band gap associated with the CSS.

4.3 Quantitative analysis of the CdSe/$CdSe_xTe_{1-x}$ heterointerface using STEM Z-contrast

Vegards Law, which states that a linear relationship exists between lattice constant and alloy composition at a constant temperature, has been shown to be valid for the $CdSe_xTe_{1-x}$ alloy [66, 68]. Therefore, as a first approximation of composition, we measured the average lattice constant in the tips and apply Vegards Law to assign composition (Figure 4.5). This approach is further strengthened by TEM size statistics of the NRHs confirming that they are sufficiently longer than the seeds to comfortably

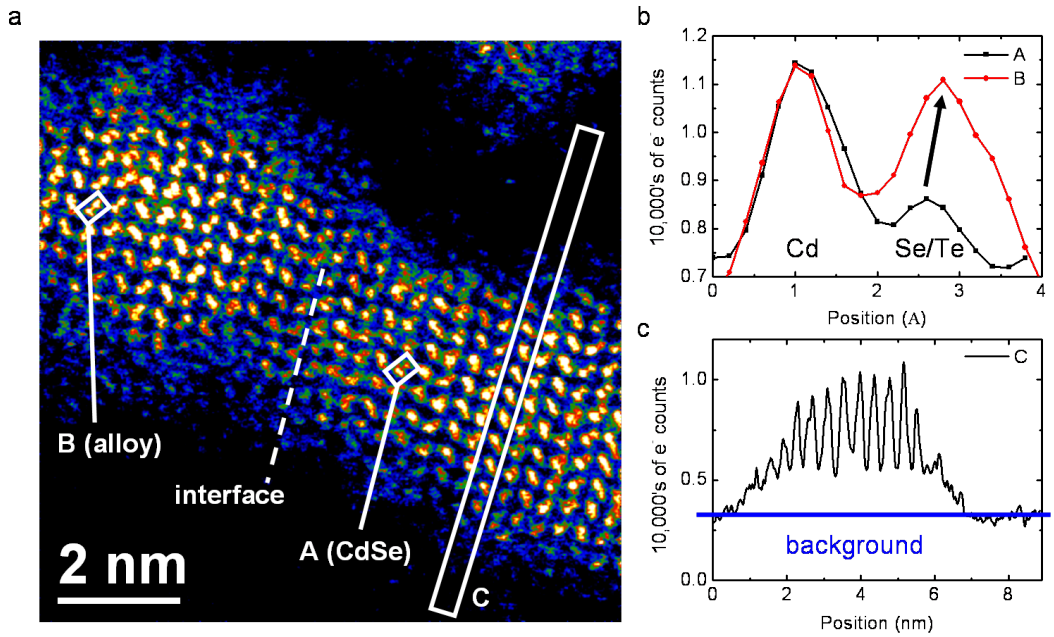

Figure 4.9: **a,** High resolution STEM image of a CdSe/$CdSe_xTe_{1-x}$ NRH. Boxed regions correspond with the integrated line-scans in **b** and **c**. The interface (dashed line) is estimated based on comparisons of line-scans of cation-anion (Cd-chalcogen) pairs in the image. **b,** Raw line-scans of two cation-anion (Cd-chalcogen) pairs corresponding with the boxed regions (A,B) in **a**. Line-scan A is assigned to CdSe since one peak is substantially higher than the other, and also because this region is near the center of the NRH. The higher peak is assigned to Cd having a much larger atomic number than Se. Line-scan B is assigned to the alloy since the peaks are closer in magnitude. The higher peak in B has the same crystallographic orientation (or equivalently, the left side of line-scan) as the higher peak in A, thus it is also assigned to the Cd column while the second peak is assigned to a combination of Te and Se atoms in that column. **c,** Longer integrated line-scan across the length of the NRH (in the CdSe region) as indicated by boxed region C in **a**. The non-negligible scattering away from the NRH is averaged to measure a "background" which is subtracted as a constant from the raw intensity profiles to compute the changes in intensity we report.

use ∼10 lattice fringes from the tip to measure composition of the second component (Figure 4.6a). While TEM imaging is excellent for statistical analysis of NRH size statistics and average lattice constants, alone it fails at characterizing the interface, particularly the interfacial strain, because composition effects on lattice constant cannot be easily differentiated from

strain effects. Having already established that Z-contrast inversion in aberration corrected scanning transmission electron microscopy (STEM) with a high angle annular dark field detector (HAADF) is excellent for establishing the heterointerface in non-alloyed NRHs [58], we now apply this technique to quantitatively characterize the structure of alloyed NRHs.

HAADF STEM is well established as a quantitative technique for elemental analysis [69]. It has been used for analysis of heterostructure interfaces [70], lattice point defects [71] and nanocrystals [72] with atomic column resolution. CdSe/$CdSe_xTe_{1-x}$ NRHs are particularly suited for this technique because of the large difference in atomic number between Se and Te, and also their small thickness. Further, because of the inherent anisotropy in NRHs, atomic column analysis can be easily conducted on each component (provided the right zone axis is available) independent of each other as opposed to core/shell NCHs.

Our approach to investigating NRHs with HAADF STEM is outlined in Figure 4.9. First, we search for a NRH with the [1 1 2 0] zone axis where the columns of cations and anions align with the electron beam. This is typically not difficult because in low magnification there is a difference in contrast between on axis and off axis NRHs. Using image analysis software (Digital Micrograph) we take integrated line-scans across cation-anion pairs in the high magnification image. The line-scans reveal two peaks corresponding with the Cd column and the Se/Te column (Figure 4.9b). Based on lower magnification images of the entire NRH telling us where the CdSe seed probably is and also based on the peak height difference in the line scans, we assign one side of the peaks in scan profiles to the Cd column, the other peak to the chalcogen column. In every lattice plane along the length of the NRH ({0 0 0 1} planes), the Cd (or chalcogen) column will

remain on the same side due to the crystal structure. After subtracting a constant due to the baseline scattering from the carbon support (Figure 4.9c), we calculate the peak intensity difference from the Cd column to the chalcogen column. For the non alloyed case, across the interface this peak intensity difference will change in sign or "invert" since Se has a smaller atomic number than Cd but Te has a larger atomic number. We refer to this this change in sign of peak intensity difference "Z-contrast inversion." For the alloyed NRHs, the peak intensity difference doesn't necessarily invert (depending on the Te concentration), nor do we expect it to.

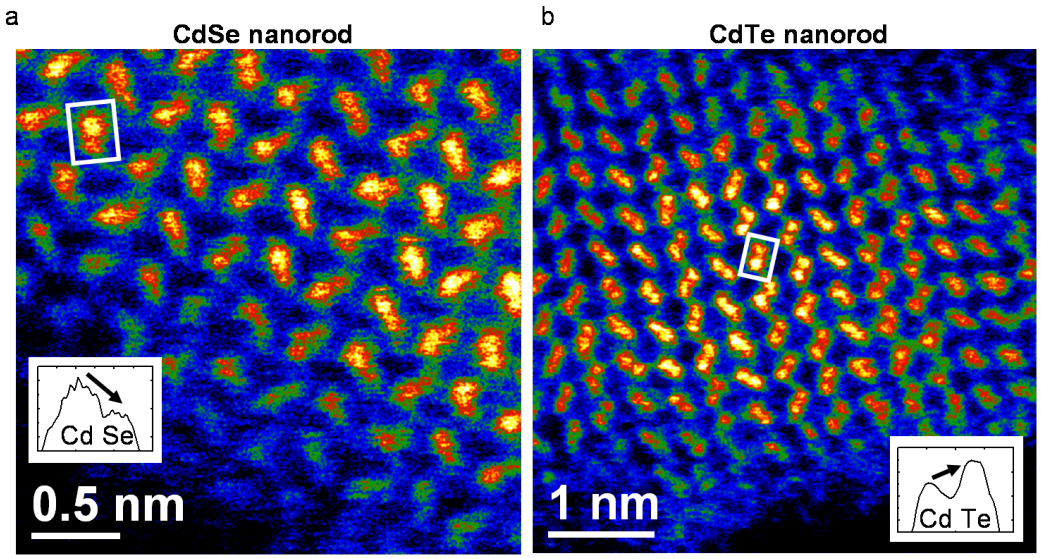

Figure 4.10: **a,b,** Characteristic high resolution abberation correction HAADF STEM images of a CdSe NR (**a**) and CdTe NR (**b**) used to establish the baseline Z-contrast (control sample)

In order to quantify alloy composition from HAADF-STEM images, Z-contrasts in control CdSe and CdTe non-alloyed NRs need to be analyzed to establish the limits. Figure 4.10 shows examples of the high resolution STEM images that were used to quantify the baseline Z-contrast for each material. We find that on average a column of Se atoms has a 25.8% (with 11.9% standard deviation and 2.14% standard error) lower scattering

intensity than a column of Cd atoms in CdSe NRs, while a column of Te atoms has a 4.4% (with 11.5% standard deviation and 1.84% standard error) higher scattering intensity, on average, in CdTe NRs (e.g. to get these numbers we took the raw scan profiles, subtracted the background scattering constant for the image, then computed Z-contrast = (Se/Te peak intensity - Cd peak intensity)/Cd peak intensity). While these scattering intensities are lower than what one would expect from the Z^2 dependence of the scattering cross section, a number of factors could reduce the contrast from the ideal case. Factors such as; scattering from capping molecules, thickness effects, possible thin shell growth, and microscope resolution (via overlap of scattering profiles). Additional atomistic modeling could potentially be used to separate out the contribution of such effects on the total observed contrast. Scattering from the thin carbon support film is 20-30% of the total and has been subtracted from the measured intensities in each image by averaging the scattering intensity in a region far from any NRs (or NRHs) in all values reported.

Before continuing we should address the question of the source of the seemingly large standard deviation. There are a number of possible sources of the deviation in measured scattering intensities; some may be desirable, others avoidable. For example, variations from scattering due to capping molecules, support film variations and surface oxidation/contamination may be reduced with special care in the sample preparation (see Methods). Variations due to the capping molecules are not completely avoidable since the NRHs are inherently prepared with them. We used the thinnest available carbon support film but variations in contrast due exclusively to the support (away from a NRH) were still $\sim$20% of the background (see Figure 4.9c). Alternatively, scattering intensity (or the lack thereof) arising

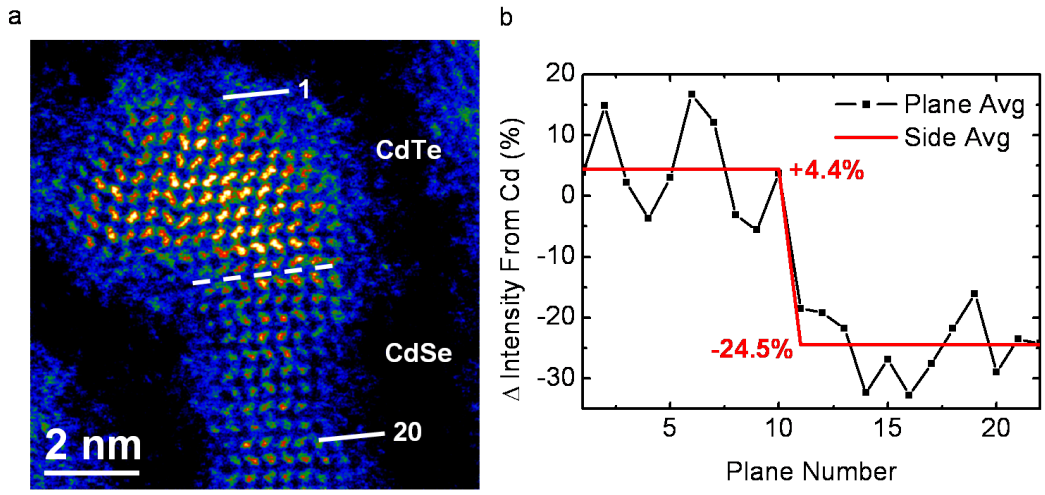

Figure 4.11: **a,** STEM image of a non alloyed (linear) NRH with lattice planes numbered and the estimated junction region shown at the dashed line. **b,** Average Z-contrast (corrected for background) as a percent change in the scattering intensity (electron count) from the Cd (cation) column to the Te (anion) column for each lattice plane in **a** (black). The contrast is averaged on each side of the estimated junction and shown as horizontal (red) lines with the average values shown.

from lattice defects or the discreteness of alloying would certainly appear in the data and if resolved, could provide new insights. For example, in a $CdSe_{0.5}Te_{0.5}$ alloy, a single chalcogen column of only ten atoms should on average have five Se ions and five Te ions. Due to phase segregation or perhaps just by chance, some columns could have more or less than the average 50:50 ratio in the alloy. The distribution of any inhomogeneity in the alloy composition would certainly be of interest. Despite these limitations, we find that by averaging over multiple columns in a plane, we can achieve a reasonably low standard error in the measurements (standard error = standard deviation / square root of number counted). In this way, we essentially compress the data for an entire plane of atoms into a single row of data points along the length of a NRH. In other materials with thicker crystals (or wider NRHs), the standard deviation in measurements is likely to be lower because a single column contains a larger number of

atoms reducing the relative effect of deviations due to the support film and capping molecules.

Analysis of non-alloyed NRHs (Figure 4.11) agrees well with the measured values for single component NRs with -24.5% (1.5% standard error) scattering intensity of the Se column relative to the Cd column on the CdSe seed side and +4.4% (2.5% standard error) intensity from Te to Cd columns on the CdTe side. The interface was abrupt, appearing to occur over a single atomic step. The consistency of this non-alloyed result with the control data on single component NRs supports the applicability of the technique to alloyed NRHs.

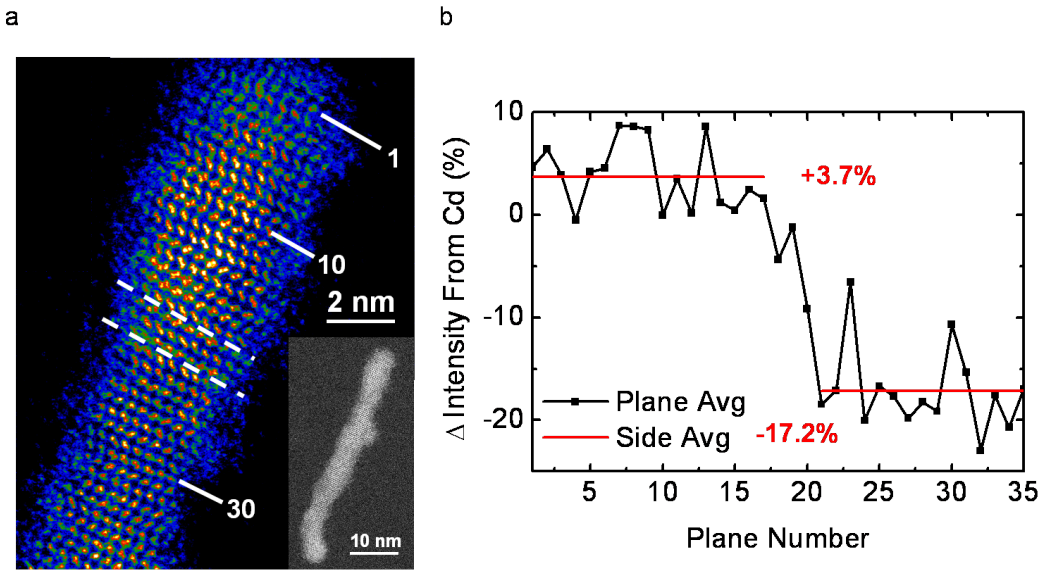

Figure 4.12: **a,** High magnification STEM image, made from a mosaic of two images, of an alloyed NRH made from 0.4 mmol of Te injected (with 0.80 mmol Se) for the second component with lattice planes numbered and the estimated junction region shown between the dashed lines. A low magnification STEM image of the same NRH is shown inset. **b,** Average Z-contrast (corrected for background) as a percent change in the scattering intensity (electron count) from the Cd (cation) column to the chalcogen (anion) column for each lattice plane in **a** (black). The contrast is averaged on each side of the estimated junction region and shown as horizontal (red) lines with the average values shown.

In the most Cd rich alloy we synthesized (0.4 mmol Te), the peak intensity differences (side averaged at -17.2% and +3.7%) were similar to the non-alloyed case except slightly lower overall (Figure 4.12). In the tip, the contrast was expected to be slightly lower since the incorporation of Se should reduce the scattering intensity of the chalcogen column (relative to the Cd column). The reduced intensity in the seed portion of the NRH is likely due to a thin shell of $CdSe_xTe_{1-x}$ which is on average ~2 monolayers in thickness according to Figure 4.6b. The interface in this particular NRH was less sharp than in the non-alloyed NRH shown in Figure 4.11, occurring over 2-5 atomic steps.

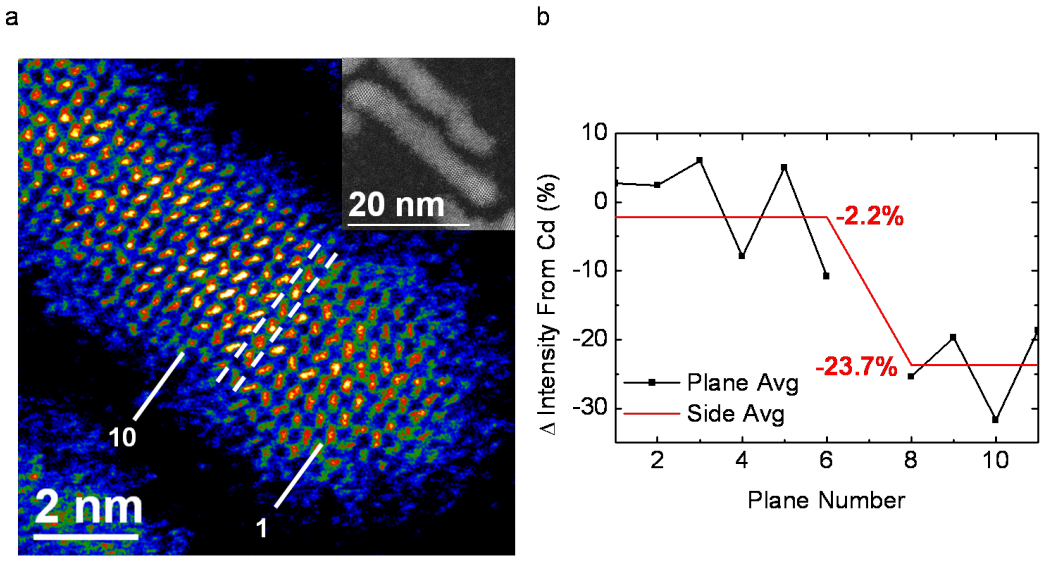

Figure 4.13: **a,** High magnification and low magnification (inset) STEM images of the same alloyed NRH made from 0.3 mmol of Te injected (with 0.80 mmol Se) for the second component with lattice planes numbered and the estimated junction region shown between the dashed lines. **b,** Average peak intensity change (corrected for background) as a percent change in the scattering intensity (electron count) from the Cd (cation) column to the chalcogen (anion) column for each lattice plane in **a** (black). The contrast is averaged on each side of the estimated junction region and shown as horizontal (red) lines with the average values shown.

Decreasing the CdTe content in the second component with the 0.3

mmol Te case, we see the side averaged Z-contrast in the tip (-2.2%) further reduced, as expected (Figure 4.13). With this alloy, the Z-contrast inversion is no longer observed across the interface as Cd column scattering is greater than the chalcogen column scattering at each plane in the NRH on average. In this case, the Z-contrast observed in the seed more closely matched the non-alloyed and control cases at -23.7%. Further, the interface was sharp happening over ∼2 atomic steps. The interface region (between the dashed white lines in Figure 4.13a), occurring over a single c-axis plane, did not have easily resolvable pairs of cation-anion peaks (unlike the ones seen in Figure 4.9b). Since these peak intensities could not be resolved, the Z-contrast for this plane was left out.

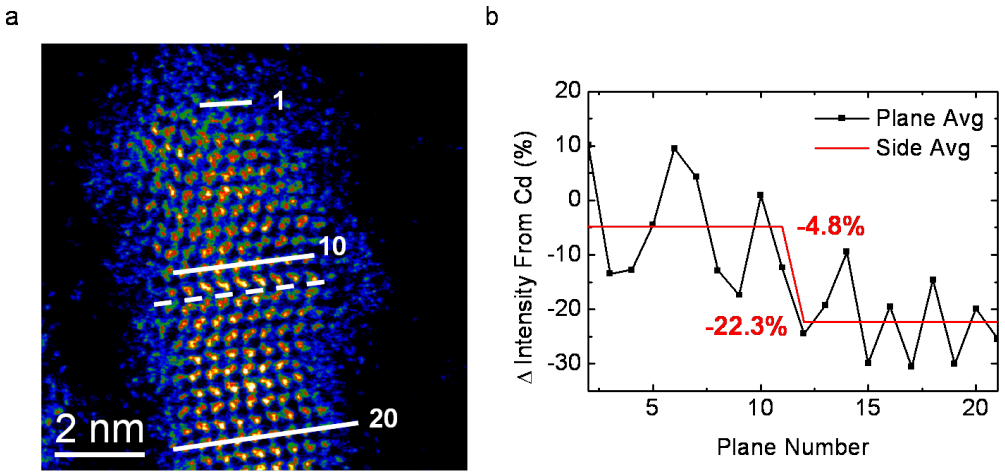

Figure 4.14: **a,** STEM image of an alloyed NRH made from 0.2 mmol of Te injected (with 0.80 mmol Se) for the second component with lattice planes numbered and the estimated junction region shown between the dashed lines. **b,** Average Z-contrast (corrected for background) as a percent change in the scattering intensity (electron count) from the Cd (cation) column to the chalcogen (anion) column for each lattice plane in **a** (black). The contrast is averaged on each side of the estimated junction region and shown as horizontal (red) lines with the average values shown.

In the 0.2 Te case, approaching the x=0.5 alloy (Figure 4.14), the Z-contrast is further reduced in the tip region (-4.8%) continuing the trend

of decreasing tip anion-cation Z-contrast with increasing CdSe content (expected). While the interface is more difficult to resolve in this case, it appears to be abrupt. With the assigned interface (dashed white line in Figure 4.14a, all planes beyond this region have an average peak intensity difference of -22.3% which is again consistent with the measurement of non-alloyed NRH and CdSe NR control case. This is the point where the relatively large standard deviation begins to limit the technique as the scatter in plane Z-contrast becomes on the order of the change in contrast from the tip region to the seed region.

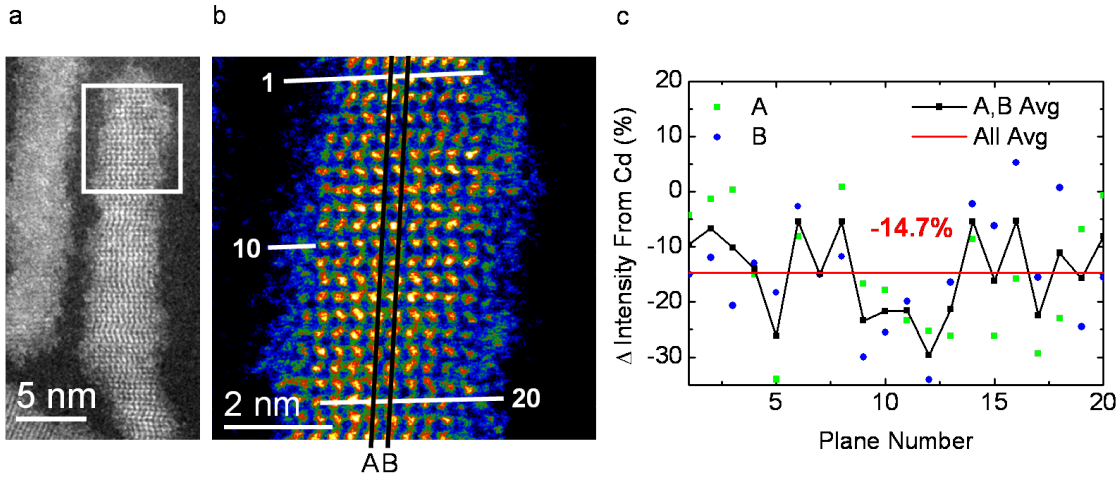

Figure 4.15: **a,b,** Low **a** and high **b** magnification STEM images of the same alloyed NRH made from 0.1 mmol of Te injected (with 0.80 mmol Se) for the second component with lattice planes numbered. **c,** The Z-contrast (corrected for background) for each individual column (green and blue) and their average (black) as a percent change in the scattering intensity (electron count) from the Cd (cation) column to the chalcogen (anion) column for each line (A,B) along the c-axis of the NRH in **a**. The contrast is averaged for all columns measured and shown as a single horizontal (red) line. A junction could not be resolved and is presumed to be outside of this image.

The final case to examine is the CdSe rich alloy synthesized with 0.1 mmol of Te (Figure 4.15). We did not attempt to resolve the interface in this case and only focused on the tip region. In Figure 4.15c we plot the

anion-cation Z-contrast for two rows of atoms (A,B) along the NRH then average them to demonstrate the importance of plane averaging. When we average all of the columns we get -14.7% which agrees with expectations for this alloy.

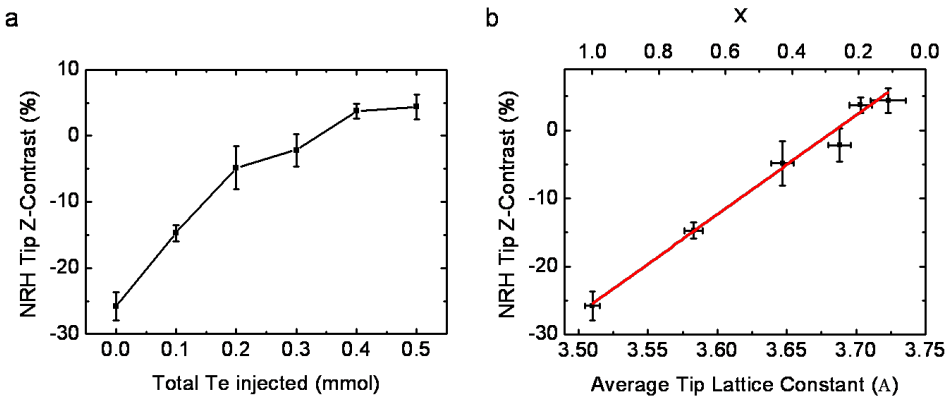

Figure 4.16: **a,** Aggregate average tip Z-contrast data as a function of Te co-injected from the previous figures. Error bars are the standard error for each case. **b,** Average tip Z-contrast versus average tip lattice constant (measured via TEM) (bottom x-axis). Composition computed from the lattice constants using Vegard's Law is also shown (top x-axis). Error bars for the lattice constants are the standard deviations for each average. A linear fit of the data is shown in red.

The tip Z-contrast statistics from each CdSe/$CdSe_xTe_{1-x}$ alloy are plotted in Figure 4.16a. There is a clear trend of increasing NRH tip Z-contrast as the amount of Te co-injected (with Se) increases. Recall that as the amount of Te (Z = 52) in the chalcogen columns increases the amount of Se (Z = 34) decreases (due to the stoichiometry balance), and so the scattering from these columns approaches and eventually overtakes the scattering from the Cd columns (Z = 48). This observation is further evidence that we are systematically controlling the composition of the alloy in these NRHs. When correlated with tip lattice constants (Figure 4.16b), we observe a linear relationship. A linear relationship has been reported previously between Z-contrast and lattice constant in aberration-corrected

imaging of $InAs_xP_{1-x}$ thin films [73], but we are the first to report such a trend in the $CdSe_xTe_{1-x}$ alloy. The linearity of this relationship means that we can use Z-contrast to spatially map composition in NRHs. However, the large deviation in measured Z-contrast in a given region of the NRH means that multiple columns must be averaged for a reliable estimation of composition. If scattering from the carbon support film could be reduced or eliminated, the measurement could become accurate enough to not rely on column averaging. Conversely, if larger diameter NRHs were studied then the signal from these NRHs might outweigh any deviations in scattering from the support film.

4.4 Conclusions from the synthesis and characterization of alloyed NRHs

While the $CdSe/Cd_xZn_{1-x}Te$ system should, in principle, be a nice system for studying the effect of strain, hurdles in the synthesis of these NRHs limited our ability to conduct a systematic study. The $CdSe/CdSe_xTe_{1-x}$ system also initially proved to be difficult to achieve with control, but we were able to synthesize NRHs with the full range of compositions. TEM analysis provided the initial evidence that we were making an alloyed second component and analysis of Z-contrast in atomic column resolution STEM images supported these results. STEM analysis suggests that even in the alloyed NRHs the interface is typically very abrupt (a few atomic steps) which agreed with our prior observations of interfaces in linear (non-alloyed) CdSe/CdTe NRHs. For the time being, using STEM Z-contrast is not the ideal technique for estimating composition spatially in NRHs because of the large standard deviation in scattering intensities

which are likely due to variations in the support film scattering mostly. As a result, many columns must be individually measured and averaged which reduces the spatial resolution of the technique and takes a large amount of time. Lattice constant analysis in TEM images does not require an aberration corrected STEM and is much faster as a method of determining composition. With image analysis algorithms, which could take a STEM image, assign anion-cation columns, and compute the Z-contrast automatically, the process could greatly be sped up.

Having established the heterointerface in alloyed NRHs to be a few atomic steps in thickness, we can now assign lattice constant variation outside of this region purely to strain. Analysis of TEM images shows the lattice constant change to be similarly abrupt (see Figure 3.5) suggesting that in the case of the linear NRHs, both alloyed and non alloyed, the strain field is highly localized near the interface. Any band bending and associated charge barriers due to strain are likely to be also localized near the interface and be extremely thin. Conversely, the strain field and associated band bending in curved NRHs is expected to be more delocalized. We have not carried out a rigorous study of the interface in curved NRHs using STEM because the partial coverage of CdTe around the CdSe (not just at the tips) means that it would be difficult to distinguish between an alloy and a shell.

Because the PL arising in type II NCHs primarily results from recombination at the heterointerface, analysis of the energy of emitted photons can be a reasonable indication of the CSS energy or the "spatially indirect" band gap at the heterointerface. We observed a tuning of the CSS PL energy over the composition range by $\sim$0.5 eV (Figures 4.8 and 4.17). This PL shift is roughly equal to the the estimated valence band offset between CdSe and CdTe of $\sim$0.6 eV. When plotted against the measured

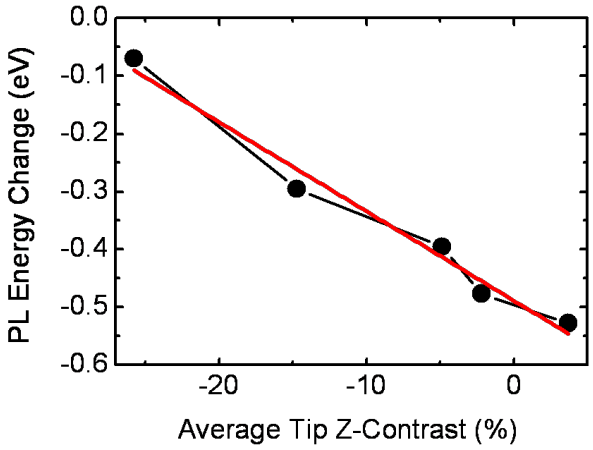

Figure 4.17: The change in PL energy as a function of average Z-contrast in the tips of alloyed NRHs. A linear fit to the data is shown.

Z-contrast in the tips, the change in PL energy is nearly linear. Since the CSS energy is set by the difference between the CdSe conduction band energy and the $CdSe_xTe_{1-x}$ valence band energy (at the type II interface), the CSS PL energy should be tuned by changes in the $CdSe_xTe_{1-x}$ valence band as we observe. There are probably too many factors involved to pull out a strain effect on band structure from PL alone, however, we do not see any sign of a modification to the CSS recombination energy due to anything other than a shift in the valence band of the $CdSe_xTe_{1-x}$ alloy.

The next step for the CdSe/$CdSe_xTe_{1-x}$ system is to explore how changes in the interfacial band structure correlates with changes in the charge kinetics of the NRHs. Understanding how these transfer rates can be modified, and how they compare with competing charge trapping rates, will be critical for establishing the utility of type II NRHs for solar cells.

4.5 Methods

4.5.1 General considerations

The single pot reactions were carried out in a standard Schlenk line under N_2 atmosphere. Technical grade trioctylphosphine oxide (TOPO) (90%), technical grade trioctylphosphine (TOP) (90%), technical grade oleylamine (70%), CdO (99.5%), Se powder (99.99%), and Te powder (99.9%) were obtained from Sigma Aldrich. ACS grade chloroform, methanol, butanol, and toluene were obtained from Fischer Scientific. N-octadecyl phosphonic acid (ODPA) was obtained from PCI Synthesis. Et_2Zn (99.9%) was obtained from STREM Chemicals. Materials were used as received.

4.5.2 Synthesis of CdSe NR seeds for CdSe/Cd_xZn_{1-x}Te NRHs

Seed CdSe nanorods. First, 2.5 g (6.5 mmol) of TOPO, 1.30 g (3.9 mmol) of ODPA and 0.205 g (1.6 mmol) of CdO were added to a 50 ml three-neck round-bottom flask. The reaction mixture was then degassed at 150 °C for 1 h under vacuum with occasional N_2 purges. The reaction mixture was then heated to 300 °C under vigorous stirring to form ODPA-Cd complex until the solution became transparent and colorless, typically after 1 h. The solvent was cooled to 150 °C and degassed for an additional 10 min to remove O_2 and H_2O produced during complexation. At 320 °C under N_2, a solution containing 0.1023 g (1.3 mmol) Se dissolved in 1.6 g (4.3 mmol) TOP and 0.3 ml toluene was swiftly injected. The reaction mixture was quenched to 260 °C where the growth was carried out, the solution changes color from light red to dark maroon over this period. After 15 min at 260 °C, the reaction mixture was rapidly cooled to 100 °C where an aliquot of

the seed CdSe nanorods was taken for analysis.

4.5.3 Synthesis of CdSe/$Cd_xZn_{1-x}Te$ NRHs in a single pot

Subsequent growth of $Cd_xZn_{1-x}Te$ was carried out by addition of Zn and Te reagents to the same reaction vessel maintained under N_2. Following the formation of CdSe NR seeds, the reaction temperature was adjusted to 170 °C at which point 0.5 ml 1M TOP-Te in TOP (0.5 mmol Te) and 0.06 ml Et_2Zn (0.5 mmol) diluted with 4ml of TOP was injected at a rate of ∼14 ml/h via syringe pump. The reaction mixture was stirred for an additional ∼45 min at 170 °C before the heating mantle was removed and the flask was rapidly cooled by air jet. Cleaning and storage procedures were same as described previously for linear and curved NRHs.

4.5.4 Synthesis of CdSe/$Cd_xZn_{1-x}Te$ NRHs in a second pot

Following the synthesis and cleaning (once) of CdSe NR seeds, they were dissolved in a "standard" concentration solution of chloroform. This standard solution had an optical density of 0.41 at 600 nm when 0.1 ml was dissolved in 3 ml chloroform in a 1 cm path length cuvette. Next, 2.0 g TOPO (5.17 mmol) and 0.689 g oleylamine (2.58 mmol) were added to a fresh 50 ml three neck flask and degassed at 120 - 130 °C for 1 h. Then, 0.3 ml (∼10 mg after vacuum drying 1h) of the "standard" CdSe solution was added and the reaction mixture was degassed for an additional 15 min. Subsequent growth of $Cd_xZn_{1-x}Te$ was carried out by addition of Zn and Te reagents to the same reaction vessel maintained under N_2. The reaction temperature was adjusted to 190 °C at which point 0.5 ml 1M TOP-Te in TOP (0.5 mmol Te) and 0.03 ml Et_2Zn (0.25 mmol) diluted with 2ml of

TOP was injected swiftly. The temperature quenched to 145 °C following the swift injection and then was set to 160 °C for 1h before the heating mantle was removed and the flask was rapidly cooled by air jet. Cleaning and storage procedures were same as described previously for linear and curved NRHs.

4.5.5 Synthesis of CdSe NR seeds for CdSe/$CdSe_xTe_{1-x}$ NRHs

First, 2.0 g (5.2 mmol) of TOPO, 0.67 g (2.0 mmol) of ODPA and 0.13 g (1.0 mmol) of CdO were added to a 50 ml three-neck round-bottom flask. The reaction mixture was degassed at 150 °C for 1 h under vacuum with occasional N_2 purges then heated to 350 °C under N_2 with vigorous stirring. The solution became transparent and colorless after 2 h indicating ODPA-Cd complex formation. The reaction mixture was cooled to 150 °C and degassed for an additional 10 min to remove O_2 and H_2O produced during complexation then heated again under N_2. At 320 °C, a solution containing 1.5 ml of 0.33 M TOP-Se in TOP (0.5 mmol) and 0.25 ml of anhydrous toluene was swiftly injected. The reaction mixture was quenched to 260 °C where the growth was carried out. After 20 min at 260 °C an aliquot of the seed CdSe NRs was taken for analysis.

4.5.6 Synthesis of linear CdSe/CdTe NRHs

To the reaction mixture containing CdSe NR seeds at 250 °C under N_2, 0.80 ml of 1M TOP-Se with varying amounts (0.0 - 0.4 ml) of 1 M TOP-Te in TOP diluted with additional TOP to make the total volume equal to 2.0 ml was injected at a rate of 8 ml/h via syringe pump. The reaction mixture was aged for an additional 5 min at 250 °C before the heating mantle was

removed and the flask was rapidly cooled by air jet. An aliquot of the NRHs was taken halfway through the injection for analysis. Upon completion of reaction, the final product was cleaned by precipitation with methanol (80%) and butanol (20%), then stored as a solution in chloroform under N_2 atmosphere.

4.5.7 TEM/STEM

Transmission electron microscopy (TEM) samples were prepared on Cu grids with ultra thin carbon film (<2nm) on lacey carbon support from a dilute solution of NCs cleaned twice then dissolved in chloroform. A low intensity, wide area electron beam shower was conducted for 30 min prior to imaging to limit the migration of contaminants, particularly organics, due to electron beam heating. The beam shower was critical for taking multiple ultra high magnification images on the same NRH with good contrast. TEM analysis was carried out with a JEOL 2100 TEM operating at 200 kV. STEM and some TEM analyses were carried out with a JEOL 2200 aberration corrected STEM/TEM operating at 200 kV.

4.5.8 Absorption and photoluminescence

UV-vis absorption spectra were obtained with Agilent 8453 photodiode array spectrometer. Photoluminescence spectra were collected with a Horiba Jobin Yvon FluoroMax-3 fluorometer.

4.5.9 XRD and EDS

Rigaku Geigerflex with the D-MAX system was used for the acquisition of powder X-ray diffraction patterns. EDS analysis was carried out with a

JEOL 2010f STEM operating at 200 kV.

CHAPTER 5

TRANSIENT ABSORPTION SPECTROSCOPY OF NANOROD HETEROSTRUCTURES

Having investigated a number of strategies for the synthesis and structural characterization of type II (semiconductor) NRHs, we would like to understand more about the band structure of these new materials. Absorption is convenient for studying the availability of states in the the conduction band to which electrons in the, often higher density (of states), valence band can be excited from. Photoluminescence is an excellent tool for probing the recombination energies of these excited electrons, typically once they have relaxed to the lowest energy states available in the conduction band. The simplicity of these techniques, and the wide availability of instruments to take these measurements, has made them standard methods for characterization of nanocrystals immediately following their synthesis. However, because absorption and PL are steady state techniques (as we have reported thusfar), they tell nothing about the kinetics of excited electrons (and/or holes) within the modified (from bulk) band structures of nanocrystals and of NCHs.

Transient absorption spectroscopy (TA) is a technique well suited for investigating the kinetics of charge processes in NCHs [74–77]. By observing the rates and wavelengths of absorption bleach (change in absorption (ΔA) <0) and the recovery of absorption, we can asses the rates of charge transfer across the heterointerface and compare them to rates of competing processes such as charge trapping and recombination.

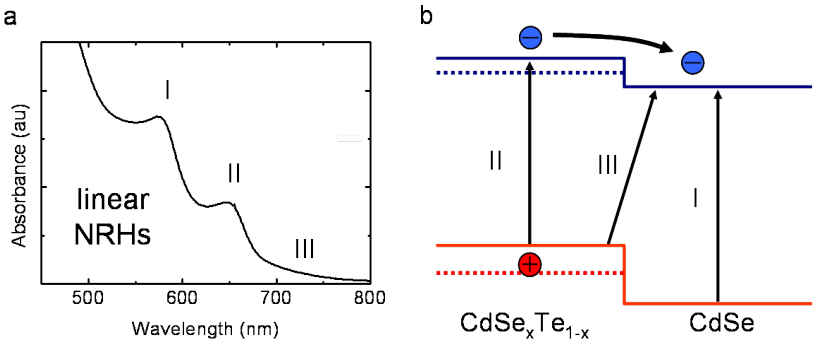

Figure 5.1: **a,** Typical absorption spectra for linear NRHs with the three primary absorption transitions of interest labeled (CdSe 1s (I), CdSe/CdTe (II) and CSS (III)). **b,** Approximate quantum confined (but unstrained) band diagram for CdSe/CdTe NRHs with the primary absorption transitions (I-III) from **a** labeled. The approximate positions of the conduction and valence bands of $CdSe_{0.5}Te_{0.5}$ in the alloyed NRHs we studied are shown as dotted lines. We primarily attempt to pump the second component of the NRHs (CdTe or $CdSe_{0.5}Te_{0.5}$), transition II, which initially fills these states and bleaches the (II) transition from occurring. On a very short time scale, the excited electron is expected to relax across the heterojunction (arrow) to the CdSe conduction band, causing a rise in the bleach of transitions I and III as the bleach of transition II recovers. We can not rule out the pumping of transition III while we pump the higher energy transition II. Not shown are competing transitions to mid-gap surface (electron and hole) trap states which occur in both single component NRs and NRHs.

5.1 Ultrafast transient absorption for probing charge separation processes

The TA spectra for CdSe and CdTe NRs exhibit the strongest bleach at wavelengths longer than the pump (lower in photon energy) and corresponding precisely with the 1s peak in their absorption spectra (Figure 5.2). In addition to the peak wavelengths, the shape and extinction of the TA spectra at wavelengths longer than the pump wavelength strongly match the absorption for each case. These observations indicate that the bleach is due to the filling of the 1s states by pump excited electrons which reduce the number of available states, and consequently, reduces the

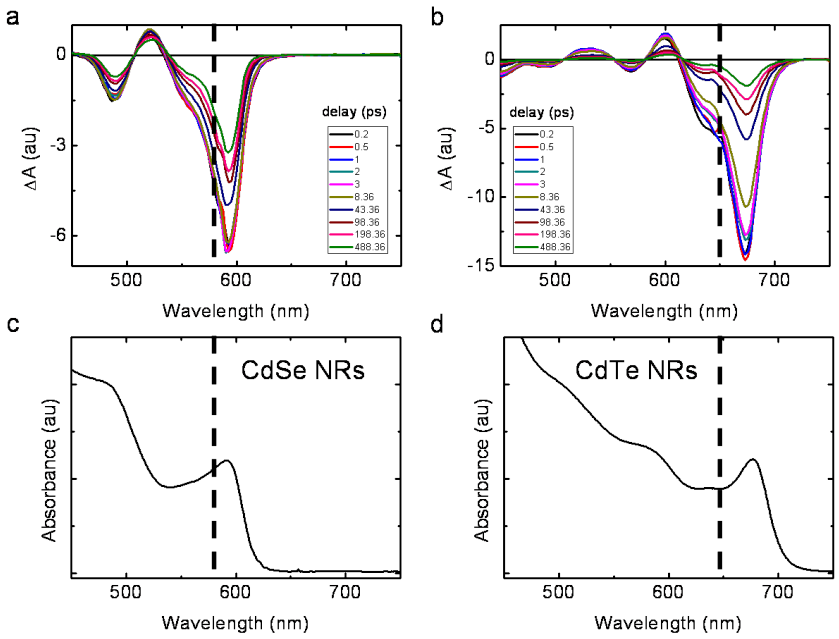

Figure 5.2: **a,b,** TA spectra for CdSe (**a**) and CdTe (**b**) NRs pumped at ∼590 nm and ∼650 nm respectively (pump wavelength noted by the dashed line) at different delays (see legend) from the ∼200 fs duration laser pulse. **c,d,** Absorption spectra of the same CdSe (**c**) and CdTe NRs (**d**) (pump noted by the dashed line).

absorption at the corresponding wavelengths. An absorption bleach is also observed for the absorption corresponding to the 1p states, however, a similarly large absorption is induced ∼30 nm to the red of the 1p bleaches. Therefore, we assign the bleach at the 1p states to a shift in absorption rather than a state filling phenomena. Interestingly, the 1d state of CdTe also appears to undergo a Stark shift although these energies are outside the spectral range of the instrument for CdSe. These observations are consistent with prior reports of the quantum confined Stark effect in which the energy of states above the (1s) ground state, e.g. the 1p and 1d states, are shifted to lower energy as a result of the electric field due the the presence of an exciton. The Stark effect may be even larger in NRs due to the inherent anisotropy of the crystal (and exciton). In addition, the

electric field of the dipole due to the polarity of the tip facets in a NR may contribute. Further, trapping of electrons (and/or) holes at surfaces may also induce a Stark shift to the absorption. A thorough analysis of the kinetics of electric field induced shift in higher energy states is left for future work.

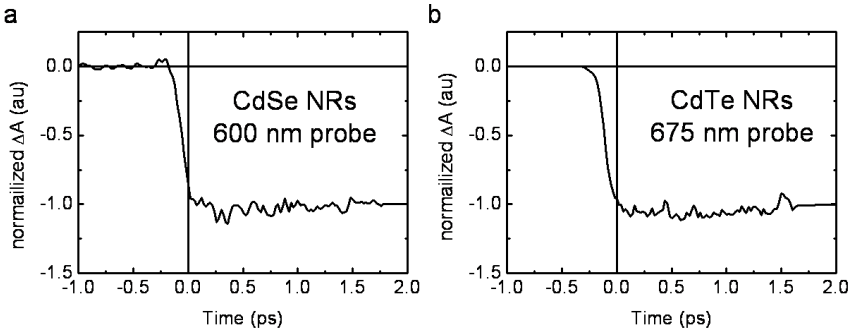

Figure 5.3: **a,b,** TA bleach kinetics for CdSe (**a**) and CdTe (**b**) NRs pumped at ∼590 nm and ∼650 nm respectively by a ∼200 fs duration laser pulse. The CdSe bleach is probed at 600nm while the CdTe bleach is probed at 675 nm. The kinetics are normalized to assign the bleach at 2 ps to be equal to -1. Time zero is set by the estimated peak of the pump signal.

The CdSe and CdTe NR short delay kinetics do not exhibit any clear features on the ultra fast (<2ps) time scale following the initial rise due to the pump. This observation indicates that charge trapping and recombination processed occur on a longer time scale, and thus, any features observed on this time scale for the NRHs can probably be attributed to charge kinetics associated with charge transfer. We point out that the time scale of the initial rise in the bleach is due to the abruptness of the convoluted pump and probe (instrument response function) which is estimated to have a ∼250 fs temporal width.

Unlike the single component CdSe and CdTe NRs, NRHs exhibit the largest bleach at shorter wavelength (higher energy) than the pump (Figure 5.4). This strongly supports the notion that electrons excited by the pump

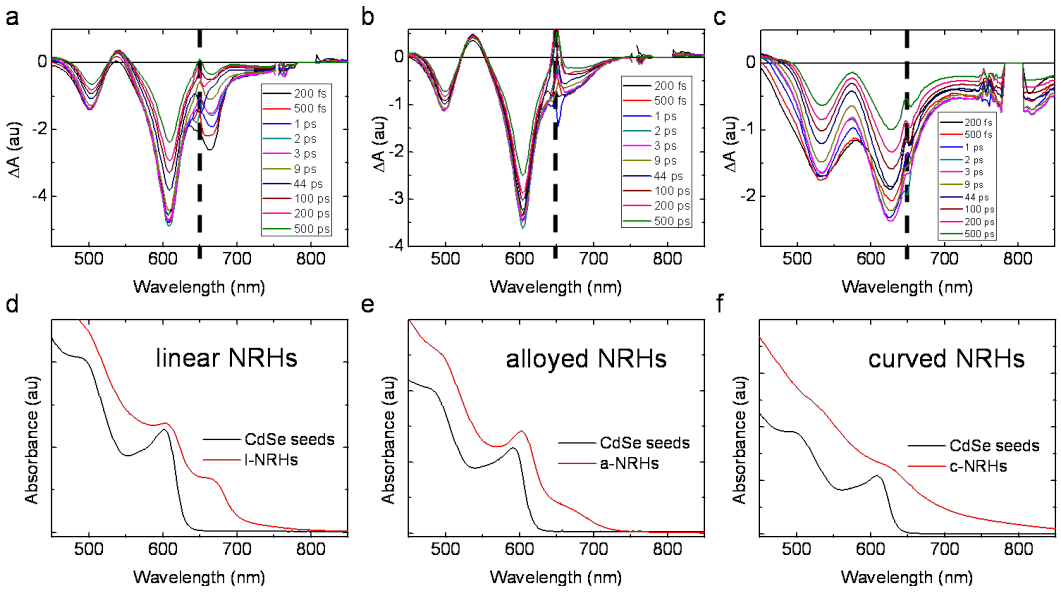

Figure 5.4: **a,b,c,** TA spectra for linear (**a**), CdSe/$CdSe_{0.5}Te_{0.5}$ alloyed (**b**) and curved (**c**) NRHs pumped at ∼650 nm (pump noted by the dashed line) at different delays (see legend) from the ∼200 fs duration laser pulse. **d,e,f,** Absorption spectra of the same linear (**d**), CdSe/$CdSe_{0.5}Te_{0.5}$ alloyed (**e**) and curved (**f**) NRHs.

in CdTe or $CdSe_{0.5}Te_{0.5}$ alloy regions are being transfered to the CdSe seeds. We expect the lowest energy state of the electron to be found in the CdSe seeds and the strongest bleach matches well with the 1s peak of the CdSe seed contribution to the NRH absorption. In addition to the primary bleach of CdSe 1s absorption following the pump, we also observe a significant bleach of the CdTe 1s absorption features in the linear NRHs which rapidly dissipates to leave only a CSS tail in the TA signal (Figure 5.4a), which we attribute to CSS absorption. In the alloyed (Figure 5.4b) and curved NRHs (Figure 5.4c), features associated primarily to the second component are more difficult to distinguish, however, a significant CSS absorption bleach is clearly present in the curved NRHs out to long wavelengths (Figure 5.4c). While establishing a peak for the CSS signal is difficult, the shape of the feature we associate with CSS in the NRH absorption spectra (tail

extending into the red) matches the longer wavelength region of the TA spectra (Figure 5.4f). While signal past 800 nm is near the presence of measurement artifacts, there does appear to be a peak in the curved NRH TA spectra near ∼825 nm which we attribute to the lowest energy CSS state. There are no such features in either the linear or alloyed NRHs.

Like the single component CdSe and CdTe NRs, the NRHs all exhibit a spectral shift in the 1p CdSe states to longer wavelength which is likely related to the Stark effect (features <∼600 nm). The Stark effect may be more pronounced in the NRHs than the NRs due to electric fields associated with strain and the charge separated state. Further, the Stark features appear larger in the curved NRHs relative to the main CdSe 1s bleach than in the other cases. While the cause of this more pronounced Stark feature is unclear, it may be due, in part, to an increased broadness of the band energies (note the broader absorption features). More work is needed to understand the Stark effect in type II NRHs.

The linear NRH kinetics (Figure 5.5a) exhibit a rapid, ∼650 fs, decay of the CdTe bleach on a similar time scale as the CSS bleach rises (∼400 fs). The CdSe bleach of the linear NRHs rises surprisingly fast, <250fs (faster than the instrument response time), which might mean that our time zero correction is off such that part of the instantaneous rise is included in the fit. These observations indicate rapid electron transfer in agreement with previous reports ∼500 fs. The alloyed NRH kinetics (Figure 5.5b) have a very similar time constants for the linear NRHs, however, the CdTe bleach does not recover as much (same time constant, lower amplitude exponential fit). This is possibly evidence of a de-localized electron within the alloyed NRHs due to the smaller conduction band offset (5.1). If this is the case, the alloyed NRHs would have a quasi type II band

offset in which the hole remains localized in CdTe, while the de-localized electron bleaches the the absorption of both CdSe and CdTe, thus the initial CdTe bleach would not recover (much).

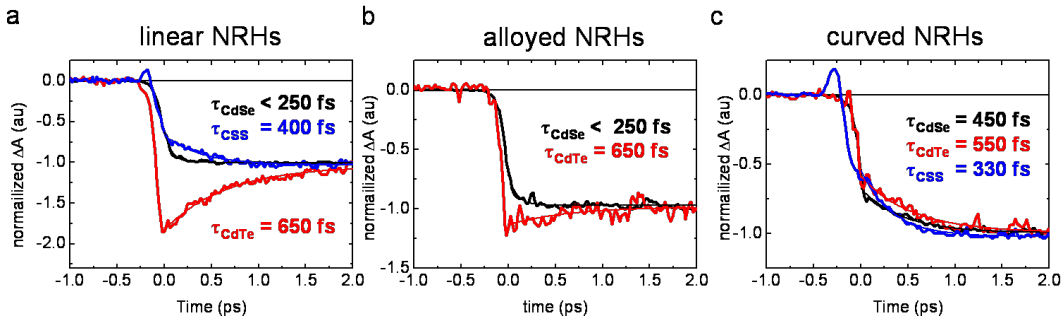

Figure 5.5: **a,b,c,** Short delay TA bleach kinetics for linear (**a**), $CdSe/CdSe_{0.5}Te_{0.5}$ alloyed (**b**) and curved (**c**) NRHs pumped at ∼650 nm by a ∼200 fs duration laser pulse. The CdSe 1s (black), CdTe 1s (or CdSeTe) (red) and CSS (blue) (not for the alloy) bleaches are probed at 600 nm (actually 625 for the curved NRHs), 665 nm and 740 nm respectively. The kinetics are normalized to assign the bleach at 2 ps to be equal to -1. Time zero is set by the estimated peak of the pump signal and set as the same for each measurement. The data has been corrected for solvent response (chirp correction) and reduced in spectral resolution. The data was fit with single exponentials (shown), time constants are inset.

The curved NRH kinetics (Figure 5.5c) exhibit distinctly different behavior from the other two cases. First, at all three relevant wavelengths, the curved NRHs exhibit a rise in bleach with almost identical kinetics, both in time (330 - 550 fs) and magnitude. The difference between 330 fs and 550 fs is probably negligible given the signal to noise ratio. The fact that we don't see a decaying bleach when we pump at 665 nm ("CdTe") is probably more of an indication of the broadness of the CdTe absorption in these structures, which we already expect from the lack of a observable peak in the curved NRH absorption spectrum attributed to CdTe. However, the apparently much slower rise of the CdSe bleach (∼450 fs) is unusual. The large magnitude of the exponential features is also unusual,

and suggests a smaller contribution of instantaneous bleach than in the other cases. We previously observed (Figures 3.2b, 3.4, 3.13c and 3.6) that the strain field in curved NRHs is more de-localized, therefore, any barrier appearing in the conduction band at the heterointerface (see Figure 4.1b) could be similarly wide. A wider barrier would mean that the tunneling rate from the CdTe region to the CdSe region is slower. Strain may be somehow be creating a metastable intermediate state to which electrons first transition to before eventually reaching the CdSe conduction band. Alternatively, strain may be somehow slowing down the relaxation of hot (excited) carriers in the conduction band of curved NRHs.

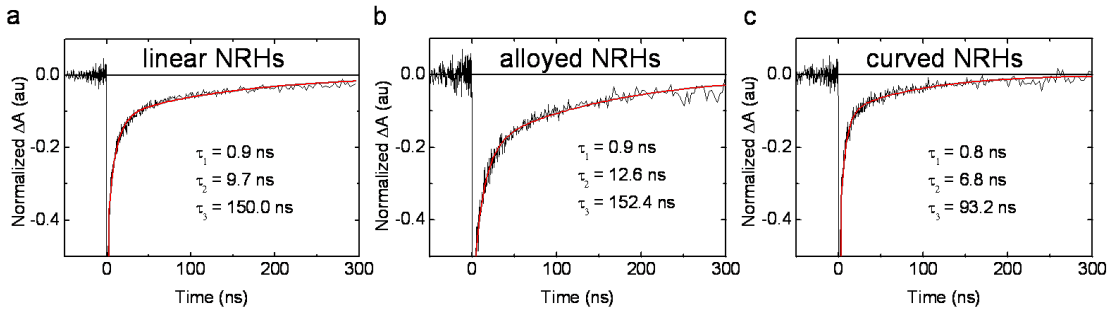

Figure 5.6: **a,b,c,** Long delay TA bleach kinetics for linear (**a**), $CdSe/CdSe_{0.5}Te_{0.5}$ alloyed (**b**) and curved (**c**) NRHs pumped at ∼650 nm. The CdSe 1s bleach is probed at 600 nm for linear (**a**) and alloyed (**b**) NRHs, at 625 nm for curved NRHs (**c**). The kinetics are normalized to assign the maximum bleach (time = 0 on this temporal scale) to be equal to -1. Time zero is set by the estimated peak of the bleach signal. The data in each case is fit with a sum of three exponentials (red), time constants are shown (inset). The bleach kinetics at other wavelengths are not shown because only the CdSe bleach is present on these time scales (with reasonable signal to noise).

5.2 Long delay transient absorption for measuring recombination kinetics

Alloyed and linear NRHs exhibit similar long delay time constants, but alloyed NRHs appear to have a larger component of the signal coming from the longer time constant, likely due to fewer electron traps associated with CdTe. This seems unusual because one would expect more electron-hole wave function overlap at the interface in the alloyed NRHs which should speed up recombination. However, since the quantum yield of PL in the NRHs is extremely low (<0.1%), recombination can be assumed to be dominated by non-radiative processes such as trap mediated and Auger recombination. Curved NRHs show the shortest time constants which may be simply explained by the larger interface area in these structures (enhancing recombination across the heterointerface). Further, the closer proximity of the type II interface (on average) to the surface in curved NRHs could help speed up surface trapping and recombination. Yet another possibility is the presence of strain induced defects which trap electrons and speed up non-radiative recombination. We have already shown the PL in curved structures to be at least an order of magnitude lower (or completely absent for larger CdSe seeds) than the already extremely weak PL from linear NRHs (see Figure 3.15), so the observation of faster recombination is not surprising.

In comparison to NRHs, CdSe and CdTe NR long delay kinetics (Figure 5.7) both demonstrate faster bleach recovery times. This indicates that recombination happens faster in the single component NRs and there are a few good explanations. First, CdSe and CdTe NRs both exhibit relatively high PL quantum yield indicating much more efficient radiative

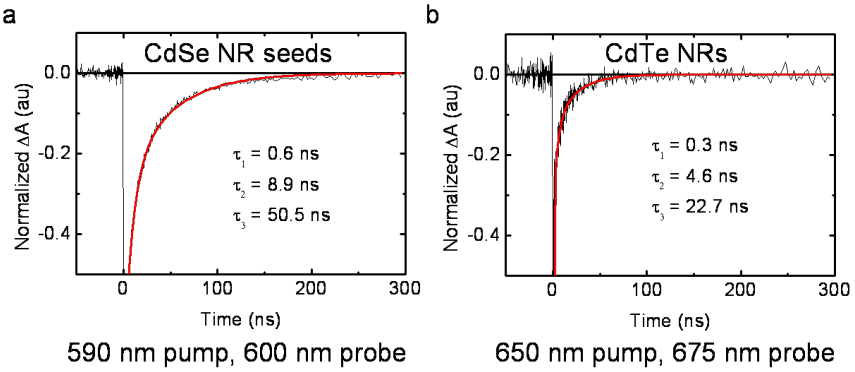

Figure 5.7: **a,b,** Long delay TA bleach kinetics for CdSe (**a**) and CdTe (**b**) NRs pumped at pumped at ∼590 nm and ∼650 nm respectively. The CdSe 1s bleach is probed at 600 nm for CdSe NRs (**a**) and at 675 nm for the CdTe NRs (**b**). The kinetics are normalized to assign the maximum bleach (time = 0 on this temporal scale) to be equal to -1. Time zero is set by the estimated peak of the bleach signal. The data in each case is fit with a sum of three exponentials (red), time constants are shown (inset).

recombination processes. Second, surface traps are more likely to capture electrons (and recover bleach) since the electron wavefunction is spread out over the entire NR. Regarding the faster recombination rate in CdTe NRs, previous reports have found surface oxidation related electron traps [78] to be common with CdTe NCs. Even though we prepared these samples carefully under a N_2 environment and conducted these measurements the day after, CdTe NRs still exhibited a faster decay time. Older CdTe NRs exhibited much faster bleach decays (not shown).

5.3 Conclusions about carrier dynamics in type II NRHs

There are multiple relevant conclusions to be made about carrier dynamics from this study of transient absorption (TA) spectroscopy. First, we confirmed the relevance of prior TA reports on type II NCHs to our linear CdSe/CdTe NRHs in that we observed rapid and long lived exciton

dissociation. We found the rate to be similarly fast for the $CdSe/CdSe_{0.5}Te_{0.5}$ alloyed NRHs but observed an absence of CdTe bleach recovery which likely indicated a de-localized electron and a quasi-type II heterojunction. Finally, the curved NRHs showed a slightly slower exciton dissociation rate and a faster recombination rate. We have some ideas about how the surface and/or strain could play a role in the distinct spectra kinetics of curved NRHs but the complexity of their band structure makes a final answer difficult.

5.4 Methods

5.4.1 Short delay transient absorption spectroscopy measurements

All TA measurements were conducted at the Argonne Center for Nanoscale Materials in collaboration with Dr. Matt Pelton. Short delay measurements were carried out using a Helios spectrometer (Ultrafast Systems). An amplified Ti:Sapphire pulse (800 nm, 120 fs, 0.5 μJ/pulse, 1.67 kHz repetition rate Spectra-Physics Spitfire Pro) was split into two beams. The first beam, containing 10% of the power, was focused into a sapphire window to generate a white light continuum (440 nm 750 nm), which serves as the probe. The other beam, containing 90% of the power, was sent into an optical parametric amplifier (Spectra-Physics TOPAS) to generate the pump beam. After the pump beam passes through a depolarizer, it is focused and overlapped with the probe beam at the sample. The pump power was chosen to be 150 nJ/pulse (250 μW power); at these pump energies, we observed no power-dependent kinetic features corresponding to multiexciton decay, indicating that each nanorod absorbs on average less

than one photon per pulse. The pump-probe delay is controlled with a mechanical delay line. All samples were dissolved in anhydrous toluene and stirred during measurements. Pump wavelengths of 590 nm for CdSe NRs and 650 nm for all other samples were used. Absorption spectra of the samples were found to be identical before and after the transient-absorption experiments, indicating that the measurements do not damage the samples.

5.4.2 Short delay transient absorption spectroscopy measurements

Long delay measurements were carried out using a EOS spectrometer (Ultrafast Systems). An amplified Ti:Sapphire pulse (800 nm, 120 fs, 0.5 μJ/pulse, 1.0 kHz repetition rate Spectra-Physics Spitfire Pro) was sent into an optical parametric amplifier (Spectra-Physics TOPAS) to generate the pump beam. After the pump beam passes through a depolarizer, it is focused and overlapped with the probe beam at the sample. The pump power was chosen to be 250 nJ/pulse (250 μW power); at these pump energies, we observed no power-dependent kinetic features corresponding to multiexciton decay, indicating that each nanorod absorbs on average less than one photon per pulse. The probe is generated by sending a lower-power pulsed laser through a photonic-crystal fiber, generating a broadband probe directly. The probe runs independently of the pulse leading to stochastic delays which are measured electronically for each pulse. All samples were dissolved in anhydrous toluene and stirred during measurements. Pump wavelengths of 590 nm for CdSe NRs and 650 nm for all other samples were used. Absorption spectra of the samples were found to be identical before and after the transient-absorption experiments, indicating that the measurements do not damage the samples.

5.4.3 General synthesis considerations

Reactions were carried out in a standard Schlenk line under N_2 atmosphere. Technical grade trioctylphosphine oxide (TOPO) (90%), technical grade trioctylphosphine (TOP) (90%), CdO (99.5%), Se powder (99.99%), Te powder (99.9%), anhydrous methanol (99.8%) and anhydrous toluene (99.8%) were obtained from Sigma Aldrich. ACS grade chloroform, ethanol, methanol, butanol, xylenes, hexanes and toluene were obtained from Fischer Scientific. N-octadecyl phosphonic acid (ODPA) was obtained from PCI Synthesis. Materials were used as received.

5.4.4 Synthesis of seed CdSe NRs

First, 2.0 g (5.2 mmol) of TOPO, 0.67 g (2.0 mmol) of ODPA and 0.13 g (1.0 mmol) of CdO were added to a 50 ml three-neck round-bottom flask. The reaction mixture was degassed at 150 °C for 1 h under vacuum with occasional N_2 purges then heated to 350 °C under N_2 with vigorous stirring. The solution became transparent and colorless after 2 h indicating ODPA-Cd complex formation. The reaction mixture was cooled to 150 °C and degassed for an additional 10 min to remove O_2 and H_2O produced during complexation then heated again under N_2. At 320 °C, a solution containing 1.5 ml of 0.33 M (TOPSe) and 0.25 ml of anhydrous toluene was swiftly injected. The reaction mixture was quenched to 260 °C where the growth was carried out. After 20 min at 260 °C an aliquot of the seed CdSe NRs was taken for analysis.

5.4.5 Synthesis of linear CdTe NRs

For comparisons of similar sizes, additional growth of CdSe and CdTe NRs were carried out. Following the formation of CdTe NR seeds, the mixture was cooled slightly to 250 °C under N_2 where 2.0 ml of 0.25 M TOP-Te was injected at a rate of 8 ml/h via syringe pump. The reaction mixture was aged for an additional 5 min at 250 °C before the heating mantle was removed and the flask was rapidly cooled by air jet. Upon completion of reaction, the final product was cleaned by precipitation with methanol (80%) and butanol (20%), then stored as a solution in anhydrous toluene under N_2 atmosphere.

5.4.6 Synthesis of linear CdSe/CdTe NRHs

To the reaction mixture containing CdSe NR seeds at 250 °C under N_2, 0.5 ml of 1 M TOP-Te in TOP diluted with additional 1.5 ml of TOP was injected at a rate of 8 ml/h via syringe pump. The reaction mixture was aged for an additional 5 min at 250 °C before the heating mantle was removed and the flask was rapidly cooled by air jet. Upon completion of reaction, the final product was cleaned by precipitation with methanol (80%) and butanol (20%), then stored as a solution in anhydrous toluene under N_2 atmosphere.

5.4.7 Synthesis of linear CdSe/$CdSe_{0.5}Te_{0.5}$ alloyed NRHs

To the reaction mixture containing CdSe NR seeds at 250 °C under N_2, 0.15 ml of 1 M TOP-Te and 0.80 mmol of 1M TOP-Se diluted with an additional 1.05 ml of TOP was injected at a rate of 8 ml/h via syringe pump. The reaction mixture was aged for an additional 5 min at 250 °C

before the heating mantle was removed and the flask was rapidly cooled by air jet. Upon completion of reaction, the final product was cleaned by precipitation with methanol (80%) and butanol (20%), then stored as a solution in anhydrous toluene under N_2 atmosphere.

5.4.8 Synthesis of curved CdSe/CdTe NRHs

Following the formation of CdSe NR seeds, the reaction mixture maintained under N_2 was heated to 300 °C where 0.5 ml of 1 M TOP-Te in TOP diluted with additional 1.5ml of TOP was injected at a rate of 8 ml/h via syringe pump (total injection time ∼15 min). The reaction mixture was aged for an additional 5 min at 300 °C before the heating mantle was removed and the flask was rapidly cooled by air jet. Upon completion of reaction, the final product was cleaned by precipitation with methanol (80%) and butanol (20%), then stored as a solution in anhydrous toluene under N_2 atmosphere.

CHAPTER 6

PHOTOVOLTAICS INTEGRATING NANOROD HETEROSTRUCTURES

Significant components of this chapter were submitted as "Integration of Type II Nanorod Heterostructures into Photovoltaics" to Nature Nanotechnology.

High quality epitaxial interfaces and delicate control over shape anisotropy achievable by versatile wet chemical synthesis make nanorod heterostructures (NRHs) with staggered band offsets efficient in separating and directing photo-generated carriers. These characteristics are also salient features useful for improving both the performance and the cost-effectiveness of photovoltaics (PVs). However, difficulties in carrier transport and extraction have imposed severe limitations, outweighing the benefits of enhanced charge separation. Hence integration of type II NRHs into PVs has thus far been unfruitful. Here, we demonstrate PVs that utilize NRHs as an extremely thin absorber between electron and hole transporting layers. In the limit approaching monolayer thickness, PVs incorporating NRHs have three times the short circuit current and conversion efficiency of devices made from their single component counterparts. Comparisons between linear and curved NRHs are also made revealing the importance of internal geometry and heterointerfacial area for enhanced contribution of charge-separated state absorption to photocurrent and in contacting charge transport layers.

Solar cells incorporating semiconductor nanocrystals (NCs) have

dramatically improved in recent years with power conversion efficiencies breaking 5% [79] and photon-to-current-conversion efficiencies above 100% [80] as new ways to utilize these quantum confined structures have been developed. Improvements in efficiency combined with versatile and scalable solution processibility (e.g., easy thin film formation at ambient conditions, incorporation into light scattering and guiding media, etc.) make integration of NCs into next generation PVs very attractive. Type II band offset nanocrystal heterostructures (NCHs) with epitaxial junctions between two different semiconductors exhibit additional advantages such as ultrafast photoinduced charge separation [74] and increased carrier lifetimes [75]. Type II NCHs can be synthesized in a variety of sizes and shapes with only minor modifications to the synthesis of single component NCs. Anisotropic (non-core/shell) type II NCHs, NRHs for example, are of particular interest because each component has exposed surface necessary for carrier extraction. Anisotropic shape also provides directionality in guiding carriers. With strong absorption in the spectral range relevant for solar applications and well-established synthesis, CdSe/CdTe NRHs are especially promising PV materials [81–83]. The type II heterointerface leads to charge separated state (CSS) absorption with a smaller binding energy penalty for dissociation and allows lower energy photons to be captured without sacrificing open circuit voltage (V_{OC}). Interfacial lattice strain can also lead to further benefits [33]. For example, deposition of CdTe onto CdSe NR seeds could be easily varied from tip only growth of "linear" NRHs to partial side growth of highly strained "curved" NRHs [58] providing additional means of tuning electronic structure to manipulate photogenerated charges.

The built-in band offset, directionality in charge separation, and

size/strain-tunable spectral response are salient features of CdSe/CdTe NRHs that could lead to significant advances in PVs. However, the ability of NRHs to improve PV performance has yet to be demonstrated. In general, undesirable aspects such as surface charge traps and inefficient carrier transport, rather than advantages brought forth by the type II interface and nanometer size scale, can limit performance [49]. Hence, it is critical to identify the optimal role(s) of NRHs when integrating them into PVs. With the exception of quantum dot sensitized solar cells, where incompatibility of most NCs with the corrosive electrolyte is a major roadblock [84], previous applications of NCs in PVs used NCs as both a light absorber and a charge transport medium. Charge transport through a NC film is quite inefficient due to the existence of surface traps and NC-NC hopping barriers [85–87] in addition to large charging energies [88]. Single phase NCs may act as an effective absorber in polymer-NC (donor-acceptor) bulk heterojunction solar cells [27] but once free carriers are created, electrons must find a pathway through interconnecting NCs to be extracted at the contact. Schottky junction solar cells incorporating NCs between conductors of differing work functions have been demonstrated as well [21] but again rely on inefficient transport of carriers through the NC film. While significant carrier mobilities have been observed in chemically treated (via ligand exchange) [87, 89–92] and doped NC solids [85, 93], expected discontinuities in the conduction and valence bands that lead to carrier trapping [90] make transport inherently more difficult through a film of type II NRHs. Geyer et al. recently found that transport through films of CdSe/CdTe nanobarbells was dominated by hole transport and was nearly identical to transport through p-type films of CdTe NCs because it was dominated by interconnecting pathways of CdTe

domains [78]. If CdSe/CdTe NRHs are to be used as absorbers in solar cells, both electrons and holes need to be transported (in the opposite directions) through the film.

Hence the key question we seek to address here is how to exploit advantages of type II band offset in NRHs while circumventing problems of carrier transport. Through proof-of-concept PVs Incorporating Nanocrystal Heterostructures (PINCHs), we demonstrate more than two-fold improvement in the overall conversion efficiency with CdSe/CdTe NRHs when compared to non-heterostructured single component nanorod (NR) devices. The improvement arises from both increased photovoltage and increased photocurrent. Enhanced CSS absorption in curved NRHs leads to further improvement in photocurrent. Active layer thickness dependence observed provides insights for improving PINCH device design.

6.1 PINCH: Type II NRHs as extremely thin absorbers

In order to exploit efficient charge separation in type II NRHs without being limited by carrier transport and extraction, our solar cell design relies on a strategy similar to the extremely thin absorber (ETA) concept proposed by Kaiser et al. [94]. In an ETA solar cell, two wide gap semiconductors forming a rectifying junction and having appropriate band energies sandwich an extremely thin film of typically intrinsic absorbing material. Here, our PINCH devices are similar to ETA solar cells with type II NRHs as the absorber. The key difference is that the NRHs with high quality epitaxial heterointerface also act as the charge separator unlike ETA solar cells where charge separation occurs at often less well-defined absorber/wide gap semiconductor interface. Photogenerated electrons in

NRHs are transferred to a wide gap electron transport layer (ETL) while holes are transferred to a wide gap hole transport layer (HTL). Both ETL and HTL should be chosen for high conductivity, photostability and appropriate band energies to block minority carriers. This approach avoids exciton diffusion as the working principle, is expected to greatly improve exciton dissociation efficiencies and does not require carrier transport through multiple NRHs.

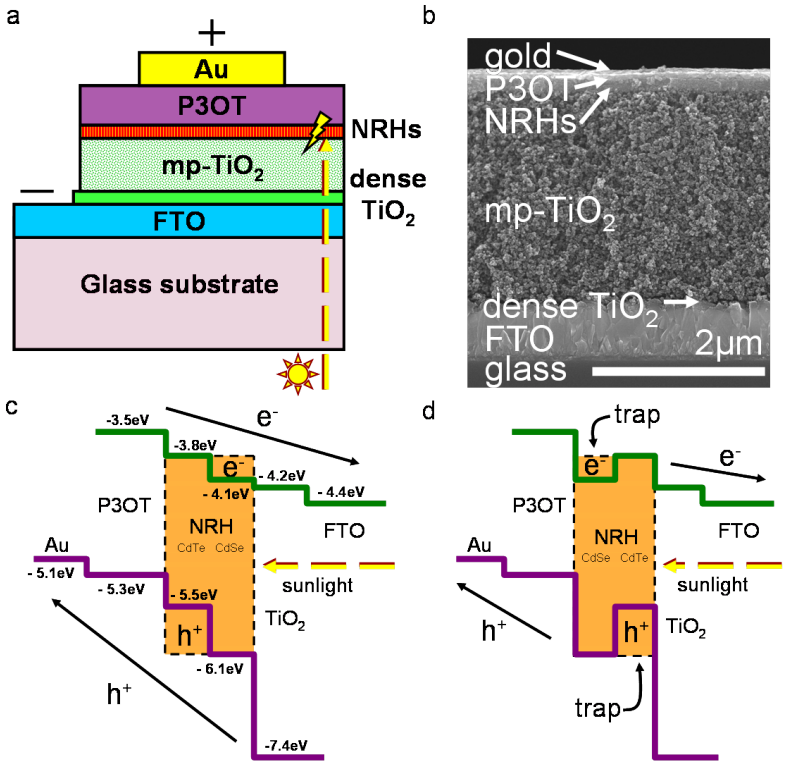

Figure 6.1: **a,** Schematic of PINCH device structure. **b,** An SEM cross section of an actual device which contains four dips of linear NRHs for the absorbing layer. **c,** The device band diagram for an ideally aligned NRH. Band edge positions are aproximated based on reported band energies relative to vacuum level in addition to the band gaps experimentally measured via absorption spectra. **d,** Band diagram for a NRH with a non-ideal alignment.

As a proof-of-concept, we have fabricated devices with the layered structure depicted in Figure 6.1a. A scanning electron microscopy (SEM)

image of the cross-section of a device is shown in Figure 6.1b. Four types of absorber layers, CdSe NRs, CdTe NRs, linear CdSe/CdTe NRHs, and curved CdSe/CdTe NRHs, have been compared. As seen in the approximate band diagram of a NRH device in Figure 6.1c, there is a clear driving force for electrons to migrate towards the fluorinated tin oxide (FTO) contact and for holes to head towards the Au contact. The ideal alignment is then for CdSe to contact TiO_2 (the ETL) and CdTe to contact poly(3-octylthiophene-2,5-diyl) (P3OT, the HTL). If a NRH is not appropriately aligned with the transport layers as shown in Figure 6.1d, the transport/blocking layers still prevent the NRH from acting like a shunt but carriers may become trapped. We anticipate a combination of both types of band arrangements in our devices where we expect the NRHs to be randomly oriented.

With the exception of devices fabricated to examine layer thickness dependence discussed later, all devices consist of an absorber NR or NRH layer formed by a single dip coating step resulting in approximately 40 nm in thickness (based on SEM imaging and estimated from optical density using reported extinction coefficients [95]). Transmission electron microscopy (TEM) images of NRs and NRHs used in this study are shown in Figures 6.2a through 6.2d along with their absorption and photoluminescence (PL) spectra in solution. The syntheses are based on previous reports [75] in which CdSe or CdTe is grown epitaxially on seed CdSe NRs (or CdTe NRs for the CdTe only case) in a single pot (see methods). The NRs and NRHs are recapped with pyridine and dissolved in a solution of methanol and pyridine for dip coating.

The photocurrent action spectra (photocurrent relative to incident photons), also known as external quantum efficiency (EQE), of all 4 types

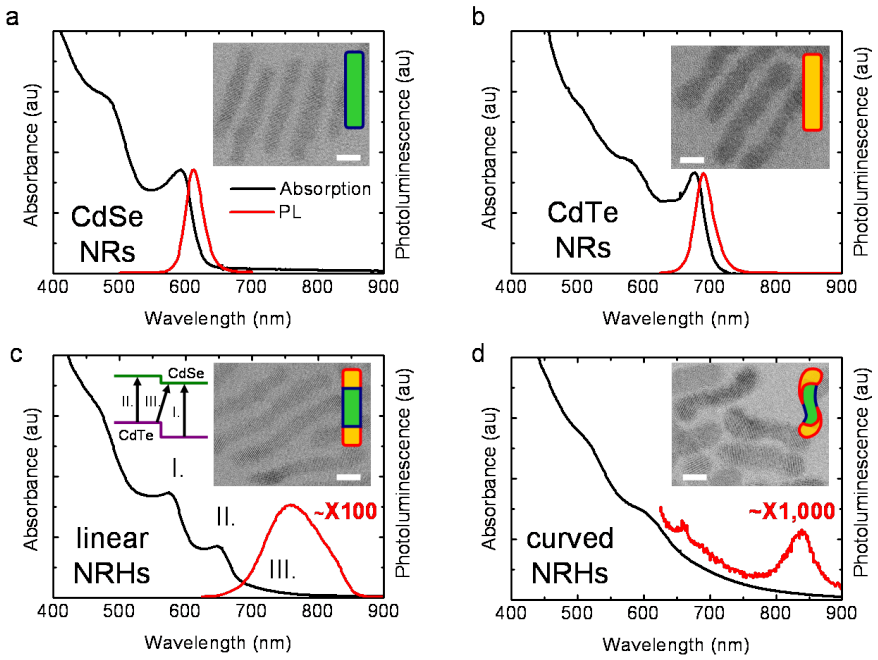

Figure 6.2: **a-d,** The absorption, photoluminescence, TEM image (inset) and structural schematic (inset) for the CdSe NRs (**a**), CdTe NRs (**b**), linear NRHs (**c**), and curved NRHs (**d**) used in this study. The scale bars of TEM images are 5 nm. Left inset in c shows optical transitions within the type II CdSe/CdTe band structure which correspond to CdSe (I), CdTe (II) and CSS (III) absorption features.

of devices are plotted in Figures 6.3a-6.3d. Features corresponding to exciton transitions are visible in the photocurrent indicating that, through all device processing steps, quantum confinement is maintained. Absorption spectra of films of NRs and NRHs even after drying in vacuum oven further confirm quantum confinement effects to be maintained (Figure 6.4). CdSe and CdTe NR control devices exhibit expected behavior in their photocurrent action spectra. The zero-bias photocurrent peak at the photon energy corresponding to the first exciton transition peak of CdTe is missing in both the CdTe NR control device and linear NRH device. These results are consistent with what has been observed in layered CdSe/CdTe NC PV cells previously reported [78]. This reduced contribution of direct CdTe excitation is likely caused by electron traps arising from CdTe surface

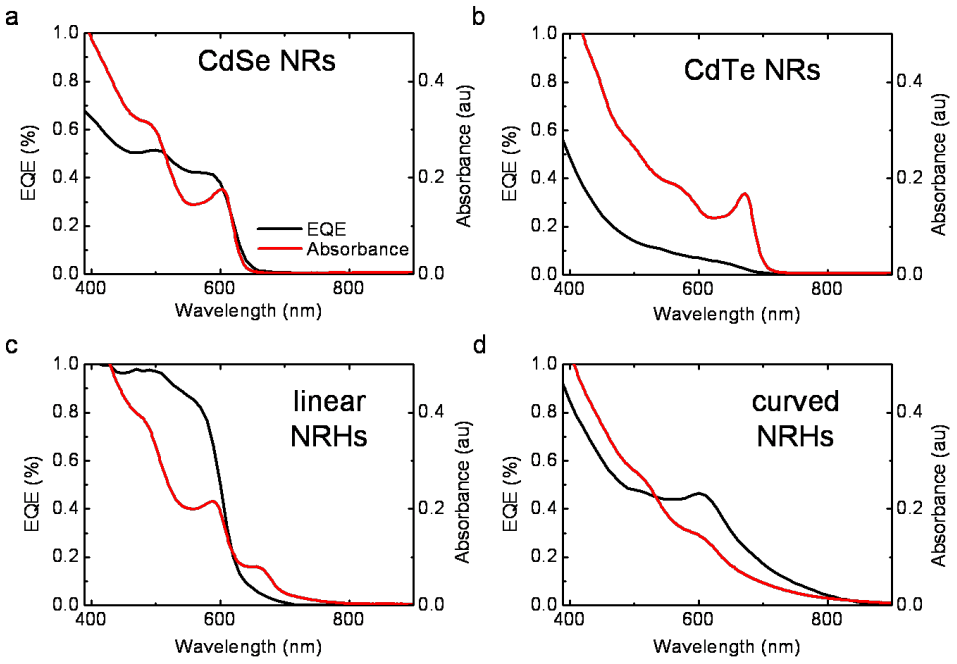

Figure 6.3: **a-d,** The EQE of devices formed from single dip (∼40 nm film) coating of recapped CdSe NRs (**a**), CdTe NRs (**b**), linear NRHs (**c**), and curved NRHs (**d**) shown along with the corresponding as-synthesized solution absorption spectra.

oxidation which competes with the electron transfer across the heterointerface. Although the broad absorption feature near the CdTe first exciton transition makes it difficult to distinguish, we suspect the same effect to be occurring in the curved NRH devices. These results indicate that photoexcitations that lead to both electrons and holes being generated in the CdTe region of NRHs are not very beneficial to PV performance. However, the key result is that devices incorporating curved NRHs exhibit significant photocurrent responses in the red tail of the spectrum which arises from CSS excitation at the heterointerface. Unlike previous report of layered device geometry consisting of CdSe NCs, linear CdSe/CdTe NRHs and CdTe NCs [78], photon energy absorbed directly into spatially separated excitons in our NRH devices do contribute significantly to the photocurrent (even at zero-bias), particularly in the case of the curved

NRHs. Because curved NRHs have a greater interfacial area, they are observed to have a larger CSS absorption cross section (Figure 6.1G) than the linear NRHs. The weakly bound electrons and holes in the CSS are more likely to be efficiently converted to free carriers that contribute to photocurrent. Further, large CSS absorption allows for low energy (sub band gap) photons to significantly contribute to photocurrent without sacrificing open circuit voltage which is, in principle, determined by the band energies.

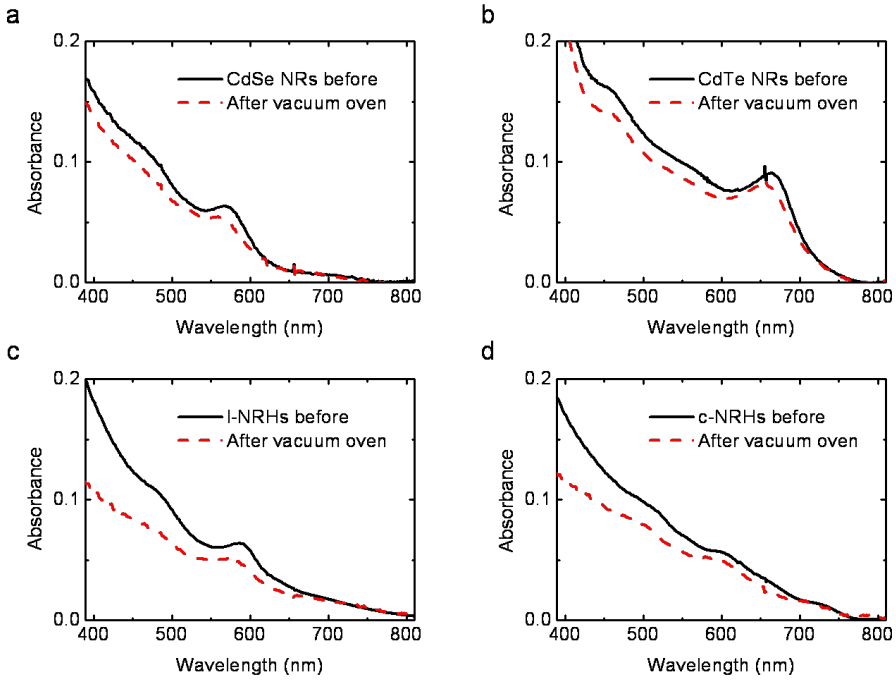

Figure 6.4: **a-d,** The change in absorbance of films following dip coating of CdSe (**a**), CdTe (**b**) NRs, linear (**c**) and curved (**d**) NRHs before and after the vacuum oven treatment at 100 °C for 24 h. Absorbance from glass/FTO/TiO_2 substrate prior to NR/NRH film deposition has been subtracted.

6.2 JV characteristics

Having established that CSS transitions in NRHs can meaningfully contribute to PV performance in our PINCH devices, we compare current density versus voltage (JV) characteristics of the 4 devices under AM 1.5G simulated sunlight (100 mW/cm^2) in Figure 6.5. The dark currents are more than an order of magnitude smaller at all biases (except near the V_{OC}) and all NR and NRH devices outperformed the control device consisting of direct TiO_2/P3OT interface (Figure 6.6). The highest V_{OC} is observed in devices with linear NRHs (∼0.60V) followed by curved NRHs (∼0.50V), CdTe NRs (∼0.40V) then CdSe NRs (∼0.10V).

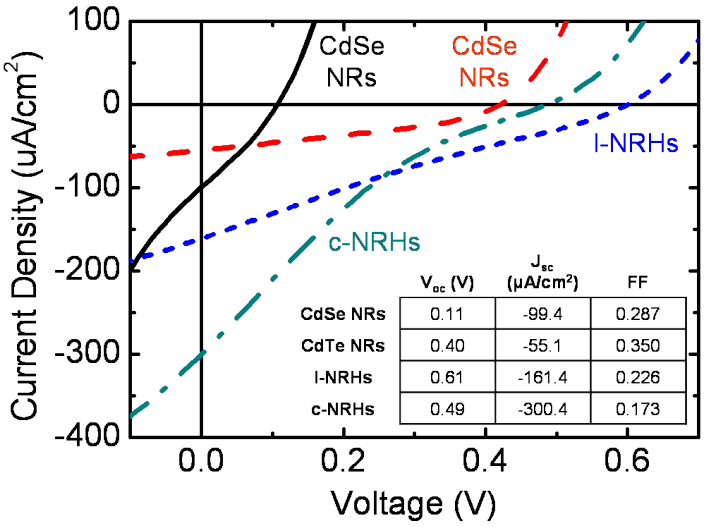

	V_{oc} (V)	J_{sc} (μA/cm^2)	FF
CdSe NRs	0.11	-99.4	0.287
CdTe NRs	0.40	-55.1	0.350
l-NRHs	0.61	-161.4	0.226
c-NRHs	0.49	-300.4	0.173

Figure 6.5: Current density (J) versus voltage (V) is plotted for devices incorporating a single dip (∼40 nm film) of recapped CdSe NRs, CdTe NRs, linear NRHs (l-NRHs) and curved NRHs (c-NRHs) under 100mW/cm^2 AM1.5 filtered light. The values of the open circuit voltage (V_{OC}), short circuit current (J_{SC}) and fill factor (FF) from each curve are also shown (inset).

The maximum possible V_{OC} for these devices should be determined by the ETL (TiO_2) conduction band to HTL (P3OT) valence band offset

which is approximately 1.1V. Less than the maximum possible V_{OC} reflects recombination processes present in the cell. The lowest V_{OC} observed in CdSe NR control device may be explained by inefficient charge separation which is expected to occur at the interface of CdSe NRs and the transport layers. Low short circuit current density (J_{SC}) in CdTe NR device may be due to oxidation induced electron traps. The higher V_{OC} in CdTe NR device than the larger band gap CdSe NR device may be attributed to a larger driving force (conduction band offset) for electron transfer from CdTe to TiO_2 [96]. Devices incorporating NRHs, which are inherently good at charge separation, exhibit significantly better performance than the single component NR control devices (higher V_{OC} and J_{SC}). The conversion efficiencies in the linear and the curved NRH devices are similar and roughly triple the CdTe devices. The improvement is even greater when compared with devices using CdSe NRs (seven times or better).

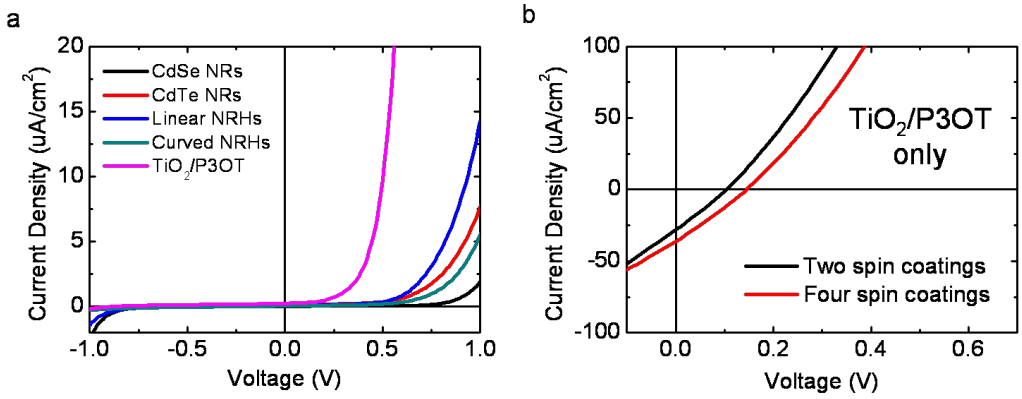

Figure 6.6: **a,** JV characteristics of single dip NR and NRH devices in the dark. The dark JV characteristics of a device made without NRs or NRHs but with two spin coatings of P3OT is also shown to demonstrate the rectifying nature of the P3OT/TiO_2 junction. **b,** JV characteristics of devices made without NRs or NRHs but with two and four spin coatings of P3OT under 100mW/cm^2 AM1.5 filtered light.

While the thinness of NRH films (only slightly thicker than the average length of individual NRHs) removes the necessity of inefficient

transport through multiple NRHs, carrier extraction, especially electron extraction, may be expected to be problematic due to CdTe surface oxidation leading to electron traps [78]. Increased J_{SC} and V_{OC} from the PINCH devices incorporating NRHs indicate that direct contact with transport layers can effectively compete with potential carrier trapping at the NRH surface. In particular, electron transfer to TiO_2 from NRHs should be more efficient then in single component NR cases. In devices consisting of only CdSe NRs as the absorbing layer, surface oxidation induced electron traps are not as problematic but charge separation, which should occur at the NR-transport layer interface, is expected to be less efficient due to interfacial recombination sites. Furthermore, charge transfer into the transport layer needs to overcome large exciton binding energies in CdSe NRs whereas electrons are already separated from holes in NRHs. In CdTe NR only control devices, similar exciton dissociation problem is also present. While surface oxide electron traps may enhance local charge separation, it would make electron transfer into TiO_2 energetically less favorable. In photoexcited NRHs, which have relaxed to the CSS, electrons are already separated from the holes and localized in CdSe (away from CdTe surface electron traps). Therefore, electron extraction into TiO_2 can compete effectively with trapping at the CdTe surface. Significantly higher J_{SC} in devices incorporating curved NRHs than in those with linear NRHs may be explained by the fact that curved structures with partial side growth of CdTe have larger CdSe/CdTe interfacial area, enhancing charge separation.

While J_{SC} and V_{OC} both improve, NRH devices exhibit a somewhat unusual inflection point in their JV characteristics which then leads to a lower fill factor (FF). One explanation for the inflection point at $\sim$0.3V is

that this is where the misaligned NRHs (i.e., when CdSe and CdTe contact the wrong transport layers as shown schematically in 6.2d) contribute to the PV response. At low biases (<0.3V), misaligned NRHs do not contribute or contribute weakly to photocurrent due to charge traps (Figure 6.1d) CdSe-HTL and CdTe-ETL offsets prevent carrier injection from transport layers to NRHs. When there is a large enough forward bias, charges in the transport layers can now overcome the NRH-transport layer band barriers and be injected into the misaligned NRHs where they recombine and counter the photocurrent. Given that the conduction band offset between TiO_2 and CdTe is about 0.4V, the inflection point appearing at $\sim$ 0.3V is consistent with a threshold external bias needed for electron injection from ETL into the misaligned NRHs leading to recombination with photo-generated holes. Assuming random orientation, the chance for contact formation with the wrong transport layer should be about the same as the favorable contact formation in curved NRHs where significant amount of CdTe deposits on the sides of the seed CdSe NRs. On the other hand, different orientations of linear NRHs with CdTe only at the tips (i.e., more anisotropic shape) may lead to larger number of distinct but less effective configurations in contacting the carrier transport layers which in turn may make the inflection point in the JV characteristics less prominent at the expense of reduced photocurrent. Hence methods to properly align NRHs should lead to significant improvement in PV performance for both types of NRHs.

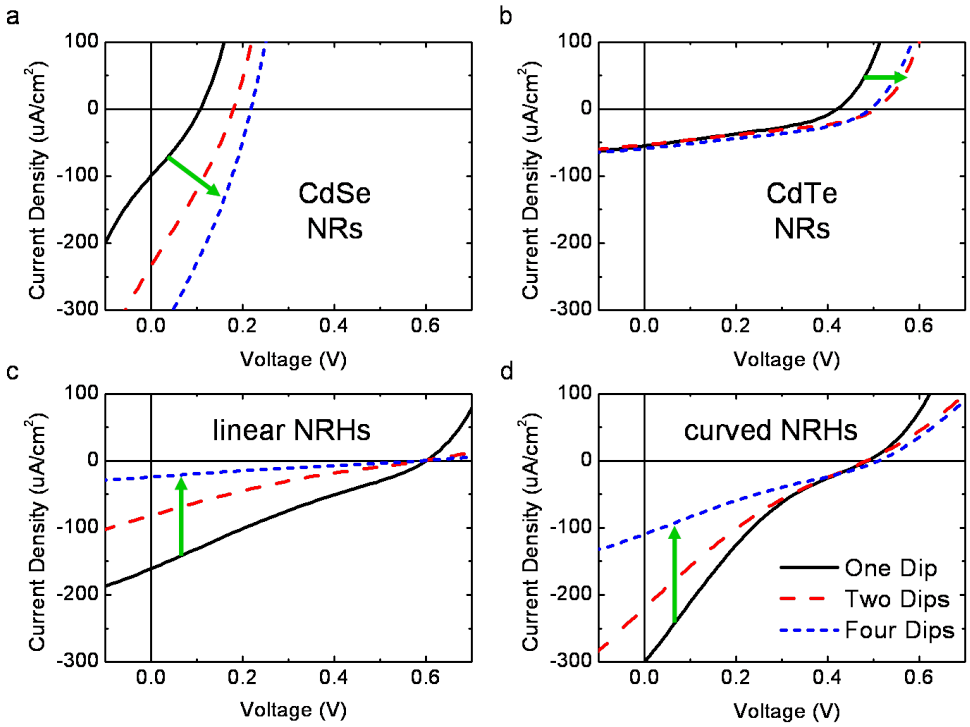

Figure 6.7: **a-d,** JV characteristics for each device fabricated with one, two and four dipping cycles of CdSe NRs (**a**), CdTe NRs (**b**), linear NRHs (**c**), and curved NRHs (**d**) contrasting the effect of increasing absorbing layer thickness on performance of NR- vs. NRH-based devices. The corresponding absorption spectra of these devices following each dipping cycle are shown in Figure 6.6.

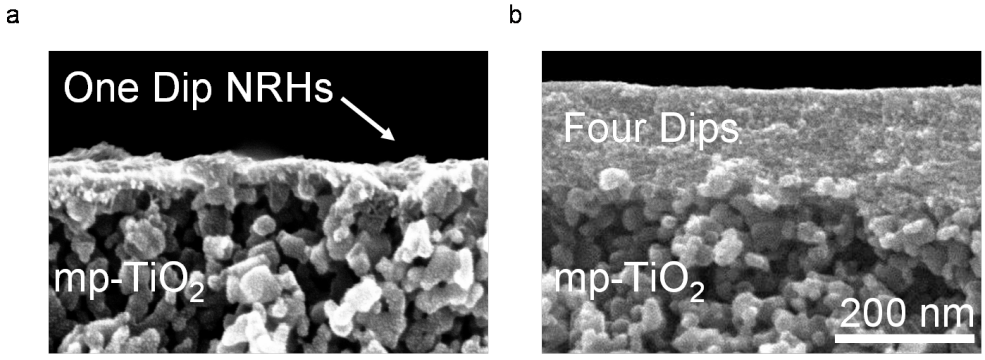

Figure 6.8: **a,b,** SEM cross sections of partially completed devices (without P3OT and gold) with one and four dip coatings of linear NRHs. We estimate that a single dip coating produces a $\sim$ 40 nm thick layer while four dip coating cycles produces a film of approximately 150 nm thickness. It can be seen that the NRH film does not penetrate into the mesoporus TiO_2 beyond the pore size of $\sim$30 nm.

6.3 Divergent effects of increasing NR/NRH film thickness

In addition to improving NRH alignment, the amount of absorbing layer can be optimized to enhance PV performance. Our current device design with ∼40 nm thick NR or NRH absorbing layer is only effective at absorbing <10% of the incident light near the band edge transitions, which is far from optimal. The simplest approach to achieving more absorption is to increase the thickness of the absorbing layer. Additional NR/NRH dipping cycles lead to increasing absorbance (Figure 6.9) consistent with thickness increase observed by SEM (Figure 6.8) and a reduction in the dark current (not shown). For the devices incorporating single component NRs, this additional thickness leads to more photons being absorbed and the photocurrent increases as does the photovoltage (Figures 6.7a and 6.7b). These enhancements are more pronounced in CdSe NRs since surface oxidation of CdTe is expected to leave additional electron traps that counteract increased photon absorption [78]. Conversely, for both the curved and linear NRH incorporating PINCHs, additional dipping cycles lead to significantly reduced photocurrent while the V_{OC} remains unchanged (Figs. 6.7c and 6.7d). The decrease in photocurrent is consistent with the expectation that thicker film of NRHs would lead to barriers for carrier transport which reduces the number of carriers that can be extracted. Note that the single dip coating thickness of ∼40 nm is only slightly larger than the average length of the NRHs (∼33 nm). The reduction in photocurrent with NRH film thickness emphasize the importance of having both the ETL and HTL in close proximity to (in contact with) an absorbing NRH for producing photocurrent i.e., to avoid transport through multiple NRHs

where type II band offset related traps (in addition to surface oxide traps of CdTe) can make transport highly inefficient.

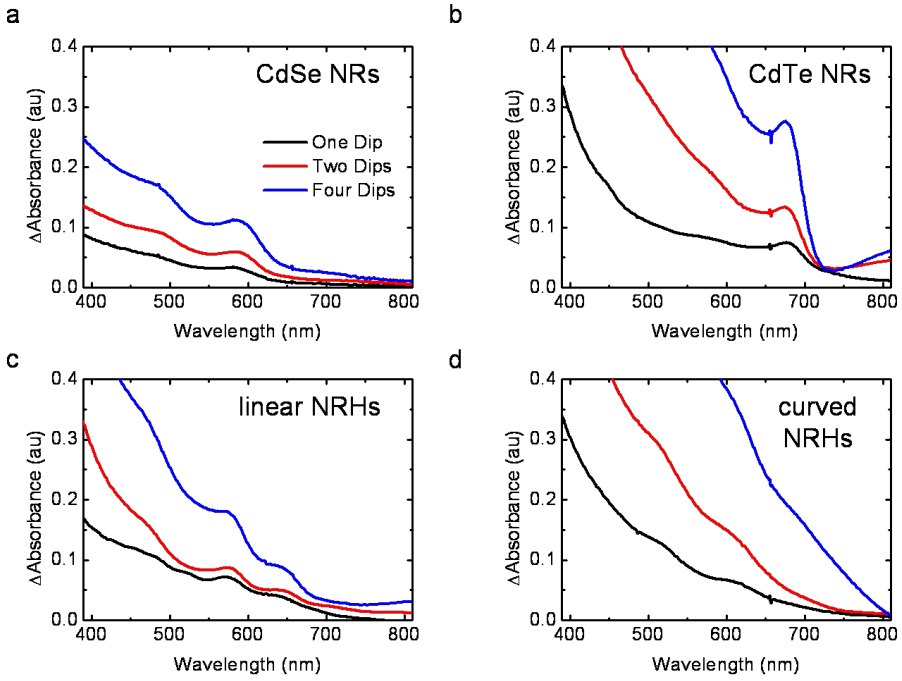

Figure 6.9: **a-d,** Absorbance of each device following one, two and four dip coating cycles. Absorbance from glass/FTO/TiO_2 substrate prior to NR/NRH film deposition has been subtracted. The devices are the same as the ones shown in Figure 6.7

6.4 Conclusions about integration of type II NRHs into PV

With our relatively simple device design, we have shown that CSS transitions arising from type II band offset NRHs can contribute meaningfully to PV performance improvement. Our results also point to areas of improvement in device design. The thickness effects suggest that in order to exploit type II NRHs in solar cells, they need to be absorbers but not charge transport media. Lower FFs, most likely arising from NRHs being misaligned with transport layers, suggest improvements in NRH

deposition process, which maximize contact between CdSe (CdTe) component and ETL (HTL), would be beneficial. Interestingly, curved NRHs with significant amount of CdTe grown on the sides of CdSe seed NRs exhibit better performance than the linear NRHs when deposited randomly. By optimizing the internal structure of individual NRHs to promote CSS absorption we are able to greatly enhance PV performance. Nearly a factor 2 larger J_{SC} observed in curved NRH devices (over the linear NRH devices) is indicative of this importance. In addition to the increasing heterointerface area and NRH morphology that optimizes proper contact with the ETL and HTL, lattice strain within NRHs may also be an important factor.

6.5 Methods

6.5.1 General considerations

Reactions were carried out in a standard Schlenk line under N_2 atmosphere. Technical grade trioctylphosphine oxide (TOPO) (90%), technical grade trioctylphosphine (TOP) (90%), CdO (99.5%), Se powder (99.99%), Te powder (99.9%), Titanium (IV) isopropoxide (TTIP) (99.99%), electronic grade regioregular poly(3-octylthiophene-2,5-diyl) (P3OT) (99.995%), acetylacetone (99.5%), anhydrous methanol (99.8%), anhydrous pyridine (99.8%) and anhydrous toluene (99.8%) were obtained from Sigma Aldrich. ACS grade chloroform, ethanol, methanol, butanol, xylenes, hexanes and toluene were obtained from Fischer Scientific. N-octadecyl phosphonic acid (ODPA) was obtained from PCI Synthesis. DSL 90T anatase (>99%) TiO_2 paste (20 wt%) was purchased from Dyesol. TEC 7 (7/sq) fluorinated tin

oxide (FTO) on 2.3 mm thick glass with 80-82% visible transmission was purchased from Pilkington. Materials were used as received.

6.5.2 Synthesis of seed CdSe and CdTe NRs

First, 2.0 g (5.2 mmol) of TOPO, 0.67 g (2.0 mmol) of ODPA and 0.13 g (1.0 mmol) of CdO were added to a 50 ml three-neck round-bottom flask. The reaction mixture was degassed at 150 °C for 1 h under vacuum with occasional N_2 purges then heated to 350 °C under N_2 with vigorous stirring. The solution became transparent and colorless after 2 h indicating ODPA-Cd complex formation. The reaction mixture was cooled to 150 °C and degassed for an additional 10 min to remove O_2 and H_2O produced during complexation then heated again under N_2. At 320 °C, a solution containing 1.5 ml of 0.33 M (TOPSe) (or TOPTe for CdTe nanorods) and 0.25 ml of anhydrous toluene was swiftly injected. The reaction mixture was quenched to 260 °C where the growth was carried out. After 20 min at 260 °C an aliquot of the seed CdSe (or CdTe) NRs was taken for analysis.

6.5.3 Synthesis of linear CdSe/CdSe and CdTe/CdTe (non-heterostructured) NRs

For comparisons of similar sizes, additional growth of CdSe and CdTe NRs were carried out. Following the formation of CdSe (or CdTe) NR seeds, the mixture was cooled slightly to 250 °C under N_2 where 2.0 ml of 0.25 M TOP-Se (for CdSe NRs) or TOP-Te (for CdTe NRs) was injected at a rate of 8 ml/h via syringe pump. The reaction mixture was aged for an additional 5 min at 250 °C before the heating mantle was removed and the flask was rapidly cooled by air jet. Upon completion of reaction, the final

product was cleaned by precipitation with methanol (80%) and butanol (20%), then stored as a solution in chloroform under N_2 atmosphere.

6.5.4 Synthesis of linear CdSe/CdTe NRHs

To the reaction mixture containing CdSe NR seeds at 250 °C under N_2, 0.5 ml of 1 M TOP-Te in TOP diluted with additional 1.5 ml of TOP was injected at a rate of 8 ml/h via syringe pump. The reaction mixture was aged for an additional 5 min at 250 °C before the heating mantle was removed and the flask was rapidly cooled by air jet. Upon completion of reaction, the final product was cleaned by precipitation with methanol (80%) and butanol (20%), then stored as a solution in chloroform under N_2 atmosphere.

6.5.5 Synthesis of curved CdSe/CdTe NRHs

Following the formation of CdSe NR seeds, the reaction mixture maintained under N_2 was heated to 300 °C where 0.5 ml of 1 M TOP-Te in TOP diluted with additional 1.5 ml of TOP was injected at a rate of 8 ml/h via syringe pump (total injection time ∼15 min). The reaction mixture was aged for an additional 5 min at 300 °C before the heating mantle was removed and the flask was rapidly cooled by air jet. Upon completion of reaction, the final product was cleaned by precipitation with methanol (80%) and butanol (20%), then stored as a solution in chloroform under N_2 atmosphere.

6.5.6 Recapping and Dipping Solution Preparation

The final reaction product except 1ml (for later analysis) was cleaned twice by dissolving reaction product in chloroform, then precipitating with

methanol and butanol. The cleaned NRs or NRHs were then dissolved in a minimal amount of chloroform and added with 10 ml (123.5 mmol) anhydrous pyridine to a 50 ml three-neck round-bottom flask fitted with a reflux condenser. N_2 gas was bubbled for 1h at room temperature then the mixture was stirred at 60 °C for 24 h under an N_2 atmosphere. Following the recapping, NRs or NRHs were precipitated with hexanes and the entire solution was dissolved in 2 ml of anhydrous pyridine and 4 ml of anhydrous methanol to form the dipping solution which was stored under N_2 atmosphere.

6.5.7 Device Fabrication

FTO coated glass substrates were cut into 2 cm x 1.1 cm pieces for each device then cleaned by sonication in acetone then rinsed with DI water and isopropanol. 200 nm of dense TiO_2 was deposited onto the substrates at 400°C by spray pyrolysis (8.58 ml ethanol, 0.82 ml acetylacetone, 0.59 ml TTIP per substrate). The dense TiO_2 was removed from one edge of the FTO/glass substrate with a razor blade to expose the back contact. A ∼1.5 μm thick layer of mesoporous TiO_2 is screen printed with a 90T mesh from Dysol paste and sintered at 500 °C in air with the following heat treatment: room temperature to 500 °C at a rate of 3 °C/min, held at 500 °C for 1 hr, then 500 °C to room temperature at a rate of -5 °C/min. The heat treated substrates were dipped into pyridine recapped NR or NRH solutions and dried with an N_2 jet to produce a film that was optically homogeneous. A ∼30 nm film of P3OT was then spin coated at 2000 rpm in air from a prepared solution of 34 mg P3OT in 0.29 g of chloroform and 12.6 g of xylenes. To crosslink P3OT, reduce NR/NRH spacing and improve thermal

stability, the devices were baked in a vacuum oven (∼100 torr) at 100 °C for 24 h. A 100 nm Au top contact was evaporated by electron beam evaporator at 0.5 Å/s at $5x10^{-6}$ torr using a shadow mask. The active area of each device was 0.283 cm^2.

6.5.8 Characterization

Transmission electron microscopy (TEM) samples were prepared on Cu grids with thin carbon film from a dilute solution of NCs in chloroform. TEM analysis was carried out with a JEOL 2100 TEM operating at 200 kV. HRTEM and STEM analyses were carried out with a JEOL 2200 aberration corrected STEM/TEM operating at 200 kV. SEM images were taken with a Hitachi S-4800 at 10kV. Cross sections were prepared from samples using a glass cutter then Pd/Au was sputtered onto the cross section to reduce charging. UV-vis absorption spectra were obtained with Agilent 8453 photodiode array spectrometer. Photoluminescence spectra were collected with a Horiba Jobin Yvon FluoroMax-3 fluorometer. Dark and light JV curves were measured immediately after device fabrication using a Keithly 2400 Source Meter. The measurements were taken at 0.01V/step, 1 s/step. Simulated sunlight at 100mW/cm^2 was generated by a Newport solar simulator with an AM 1.5G filter. External quantum efficiency was measured with an OL 750 Spectroradiometer under a light bias. Measurements were taken in steps of 10 nm with a 1-2 s delay between steps. The chopper frequency was set to 41 Hz.

CHAPTER 7

CONCLUSIONS AND FUTURE DIRECTIONS

7.1 Conclusions

With our work on the Fe_3O_4/CdS system, we have shown that the junction formation step can be separated from growth while the average number of CdS particles growing on Fe_3O_4 seeds can be maintained in anisotropic NCH synthesis. By doing so, we have been able to examine how the maximum number of heterojunctions that can form depend on the size of the seed NCs and how the growth rate affects the resulting NCH morphology. The emerging picture of the growth mechanism for anisotropic Fe_3O_4/CdS NCHs from the results obtained is as follows. CdS can nucleate on $\{1\,1\,1\}$ planes of seed Fe_3O_4 NCs in either wurtzite or zinc blende form. Slow growth leads to dots-on-dot morphologies where the maximum number of CdS that can grow on Fe_3O_4 is mainly determined by the interfacial strain. The strain may be considered to limit the nearest possible distance between growing CdS particles. Rods-on-dot structures arise at fast growth rates and these structures provide insights on the heterointerfaces and how polytypism in CdS leads to three distinct morphologies: "branched" structure when CdS nucleates as zinc blends and "linear" and "kinked" structures with wurtzite nucleation. The branched and the linear structures have the same junction planes with coincidence sites -i.e. $\{1\,1\,1\}_{\text{CdS(Zinc Blende)}}$ or $\{0\,0\,0\,1\}_{\text{CdS(Wurtzite)}}$ aligned with

$\{1\,1\,1\}_{Fe_3O_4}$. The CdS junction planes of kinked structures are $\{1\,0\,\bar{1}\,1\}$ planes which in the presence of stacking faults may become nearly identical to the $\{0\,0\,0\,1\}$ planes at the interface. While the overall wurtzite to zinc blende ratio of the CdS nuclei does not appear to change very much with size, the linear-to-kinked ratio increases with increasing seed Fe_3O_4 size which may also be attributed to strain effects.

We have presented atomic resolution imaging of both linear and curved CdSe/CdTe NRHs. In the absence of strain relieving defects, surprisingly large compressive strain of $\sim$4% leading to an overall axial deflection can be induced on the seed CdSe NRs when the larger lattice CdTe deposits on both the tips and on the sides of the seeds. Linear barbell NRHs exhibit sharp interfaces. Both types of NRHs exhibit absorption features corresponding to charge transfer, expected of type II band offset heterostructured materials. The linear barbell structures exhibit weak but large Stokes-shifted PL at room temperature while the curved exhibit more than an order of magnitude lower PL yield. Almost complete quenching of PL in the curved NRHs may be associated with charge trapping at the surface that is in close proximity to the heterointerface where charge separation occurs. Combined with the ability to control the location of CdTe on the seed CdSe NRs, strain effects observed here may provide new approaches to directing separation of photogenerated carriers which may facilitate incorporation of NRHs in various energy applications.

Despite difficulties in managing differences in precursor reactivity, we developed a strategy for synthesizing alloyed CdSe/$CdSe_xTe_{1-x}$ NRHs with controlled composition. We were able to verify the tuning of composition both by TEM and Z-contrast HAADF-STEM analysis. In the process, we found the interface to consistently be very sharp, a few

monolayers in thickness, but were limited in resolution by column averaging which was required to reduce the large deviations in scattering intensity likely resulting mostly from the support film. As we tuned the composition, we discovered a linear relationship between the change in PL energy (from the CdSe seeds) with the composition. The magnitude of change in PL energy of ∼0.5eV across the composition range was in good agreement with the estimated valence band offset between CdSe and CdTe. This indicated that the valence band of $CdSe_xTe_{1-x}$ was effectively tuned with the alloy composition. The linear relationship suggested that strain did not play an appreciable role in determining the energy of the CSS in these linear structures.

We conducted a transient absorption (TA) spectroscopy study of linear, alloyed and curved NRHs to uncover the dynamics of excited carriers in these structures. We found extremely rapid charge separation in all cases with the alloy and linear NRHs fastest. Long delay kinetics revealed a long time constant component of the bleach decay not present in the single component CdTe and CdSe NRs. This long decay component, while relatively small in amplitude, hints at the potential for type II NRHs to produce long lived carriers following the absorption of a photon. We were not surprised to find faster recombination in the curved NRHs and suspect the increase in interface area and/or proximity of the interface to the surface plays a significant role.

Many studies of type II NRHs have been motivated by solar energy applications yet few have actually incorporated these structures into devices and none have demonstrated an improvement over single component NC-based devices. With a relatively simple device, designed from the start to take advantage of type II NRH's attractive qualities, we were able to

learn much about the role a type II NRH would play in a next generation solar cell. First, type II NRHs need to act only as absorbers and not as charge transporters. Second, NRHs should be optimized so as to promote the contribution of charge separated states to their absorption since this absorption of lower energy photons can meaningfully contribute to photo-current without much of a voltage penalty. And finally, type II NRHs should be aligned with transport layers so that each component of every NRH is appropriately contacted. Even without a fully optimized device, on a film thickness equivalent basis, we have shown that NRHs can outperform their single phase (CdSe and CdTe) NR counterparts in the limit approaching a single monolayer thickness of the absorbing film.

7.2 Future directions

Based on intuitive expectations about the strain effects on the interface band structure, it may be favorable to use CdTe NRs as seeds or at least as a comparison with the CdSe seeded system. With CdTe seeded $CdTe/Cd_xZn_{1-x}Te$ NCHs, the seeds would be expected to be entirely under compressive strain (in the absence of curvature) as opposed with CdSe seeds. To probe even larger strains CdS, may be explored as a seed material which has a 10% mismatch with CdTe and can easily be prepared as wurtzite phase NRs with precision [97].

Another approach to isolating strain effects from band structure effects could be to form a heterojunction of graded composition. By varying the degree of grading one could in principle control the magnitude of strain. $CdSe/CdSe_xTe_{1-x}$ may be a model system to demonstrate first, that nanorod heterostructures of graded composition can be synthesized, and

second, that there is some information about strain effects to be gleaned when this graded composition NRH is compared with the abrupt CdSe/CdTe case outlined in this thesis. A compositional gradient would be achieved by varying the Te/Se ratio in a series of chalcogen precursor injections.

In addition to TA, it would be ideal to measure radiative recombination kinetics via time resolved PL simultaneously. Time resolved PL would only be possible on the linear and alloyed NRHs (with reasonable PL yield), however, by cooling curved NRHs the PL yield may increase enough to conduct a time resolved study. PL decay times could be correlated with TA bleach decay kinetics to extract the radiative contribution to the overall recombination rates observed.

Regarding solar cell integration of type II NRHs, since our current device design does not fully utilize incident photons, increasing the number of NRHs in the absorption layer is necessary. This increase should be achieved by conformally coating a high surface area ETL (or HTL) and infilling with the HTL (or ETL) to avoid problems of carrier transport through multiple NRHs. Given that NRHs do not penetrate mesoporous ETL of ~25 nm average diameter TiO_2 very much, simply increasing the TiO_2 pore size may lead to a significant improvement.

7.3 Concluding remarks

Clearly, NRHs exhibit a number of seemingly attractive qualities for photovoltaics. Absorbed photons generate physically separated electrons and holes within the structure extremely rapidly and some of these carriers persist for over 150 ns. We can tune the structures with relative ease in

their size, shape and composition. These structural changes are well correlated with changes in optical and electronic properties which may enable us to choose properties first, then engineer NRHs to fit the design criteria.

When it comes to practical application of these materials for solar energy applications, serious challenges remain. The ideal application of type II NRHs in a solar cell requires an extremely thin film, which is uniformly thick and in which, the NRH components are appropriately aligned with adjacent transport layers. Having an extremely thin film doesn't give any meaningful absorption, so the strategies must be developed for channeling light into this film or increasing the film area/volume ratio through a meso-porous structure. These approaches may not be applicable with ultra cheap roll-to-roll processes currently used by the lowest cost PV manufacturers. Further, oxidation of NRHs, particularly certain materials (e.g. CdTe, PbSe, PbS), greatly reduces their utility. Since many PV technologies already have this problem, the oxidation issue may not be so worrying, but certainly it needs to be kept in mind.

Regarding the future applications of the work discussed in this thesis, we would like to quote Dr. Herbert Kroemer, father of the heterojunction, from his Nobel Lecture: "We must take a long-term look when judging the applications potential of any new technology: It must not be judged simply by how it might fit into already existing applications, where the new discovery may have little chance to be used in the face of competition with already entrenched technology. Dismissing it on the grounds that it has no known applications will only stifle progress towards those applications that will grow out of that technology. I do not think we can realistically predict which new devices and applications may emerge,

but I believe we can create an environment encouraging progress, by not always asking immediately what any new science might be good for." [98]

One of the most exciting aspects of this nanocrystal research, in general, is how rapidly it is changing. In the last five years, NC solar cell record efficiencies have more than doubled and are now approaching 10%. There is still much we don't know about how to take advantage of the various attractive qualities of nanocrystals in useful ways, but new discoveries are being made every day. The ease and scalability of colloidal synthesis suggests that nanocrystals are a path towards cheap sustainable solar energy harvesting. With a little luck and determination, we will continue on the path astonishing progress we have made in these inspiring times.

REFERENCES

[1] S. G. Kwon and T. Hyeon, "Colloidal chemical synthesis and formation kinetics of uniformly sized nanocrystals of metals, oxides, and chalcogenides," *Accounts of Chemical Research*, vol. 41, no. 12, pp. 1696–1709, 2008.

[2] R. Xie, Z. Li, and X. Peng, "Nucleation kinetics vs chemical kinetics in the initial formation of semiconductor nanocrystals," *Journal of the American Chemical Society*, vol. 131, no. 42, pp. 15 457–15 466, 2009.

[3] J. Y. Rempel, M. G. Bawendi, and K. F. Jensen, "Insights into the kinetics of semiconductor nanocrystal nucleation and growth," *Journal of the American Chemical Society*, vol. 131, no. 12, pp. 4479–4489, 2009.

[4] B. Koo, R. N. Patel, and B. A. Korgel, "Synthesis of CuInSe2 nanocrystals with trigonal pyramidal shape," *Journal of the American Chemical Society*, vol. 131, no. 9, pp. 3134–3135, 2009.

[5] S. Peng and S. Sun, "Synthesis and characterization of monodisperse hollow Fe3O4 nanoparticles," *Angewandte Chemie International Edition*, vol. 46, no. 22, pp. 4155–4158, 2007.

[6] C. B. Murray, D. J. Norris, and M. G. Bawendi, "Synthesis and characterization of nearly monodisperse CdE (E = sulfur, selenium, tellurium) semiconductor nanocrystallites," *Journal of the American Chemical Society*, vol. 115, no. 19, pp. 8706–8715, 1993.

[7] J. A. McGuire, J. Joo, J. M. Pietryga, R. D. Schaller, and V. I. Klimov, "New aspects of carrier multiplication in semiconductor nanocrystals," *Accounts of Chemical Research*, vol. 41, no. 12, pp. 1810–1819, 2008.

[8] A. J. Nozik, "Multiple exciton generation in semiconductor quantum dots," *Chemical Physics Letters*, vol. 457, no. 1-3, pp. 3 – 11, 2008.

[9] D. I. Enache, J. K. Edwards, P. Landon, B. Solsona-Espriu, A. F. Carley, A. A. Herzing, M. Watanabe, C. J. Kiely, D. W. Knight, and G. J. Hutchings, "Solvent-free oxidation of primary alcohols to

aldehydes using Au-Pd/TiO_2 catalysts," *Science*, vol. 311, no. 5759, pp. 362–365, 2006.

[10] V. I. Klimov, A. A. Mikhailovsky, S. Xu, A. Malko, J. A. Hollingsworth, C. A. Leatherdale, H.-J. Eisler, and M. G. Bawendi, "Optical gain and stimulated emission in nanocrystal quantum dots," *Science*, vol. 290, no. 5490, pp. 314–317, 2000.

[11] M. Shim and P. Guyot-Sionnest, "N-type colloidal semiconductor nanocrystals," *Nature*, vol. 407, no. 6807, pp. 981–983, 2000.

[12] C. Wang, M. Shim, and P. Guyot-Sionnest, "Electrochromic semiconductor nanocrystal films," *Applied Physics Letters*, vol. 80, no. 1, pp. 4–6, 2002.

[13] H.-Y. Chen, M. K. F. Lo, G. Yang, H. G. Monbouquette, and Y. Yang, "Nanoparticle-assisted high photoconductive gain in composites of polymer and fullerene," *Nature Nanotechnology*, vol. 3, no. 9, pp. 543–547, 2008.

[14] P. V. Kamat, "Quantum dot solar cells. semiconductor nanocrystals as light harvesters," *The Journal of Physical Chemistry C*, vol. 112, no. 48, pp. 18 737–18 753, 2008.

[15] I. Medintz, H. Uyeda, E. Goldman, and H. Mattoussi, "Quantum dot bioconjugates for imaging, labelling and sensing," *Nature Materials*, vol. 4, no. 6, pp. 435–446, 2005.

[16] D. R. Larson, W. R. Zipfel, R. M. Williams, S. W. Clark, M. P. Bruchez, F. W. Wise, and W. W. Webb, "Water-soluble quantum dots for multiphoton fluorescence imaging in vivo," *Science*, vol. 300, no. 5624, pp. 1434–1436, 2003.

[17] H. B. Na, I. C. Song, and T. Hyeon, "Inorganic nanoparticles for MRI contrast agents," *Advanced Materials*, vol. 21, no. 21, pp. 2133–2148, 2009.

[18] M. Kuno, D. P. Fromm, H. F. Hamann, A. Gallagher, and D. J. Nesbitt, "Nonexponential "blinking" kinetics of single CdSe quantum dots: A universal power law behavior," *The Journal of Chemical Physics*, vol. 112, no. 7, pp. 3117–3120, 2000.

[19] M. Pelton, D. G. Grier, and P. Guyot-Sionnest, "Characterizing quantum-dot blinking using noise power spectra," *Applied Physics Letters*, vol. 85, no. 5, pp. 819–821, 2004.

[20] R. Asahi, T. Morikawa, T. Ohwaki, K. Aoki, and Y. Taga, "Visible-light photocatalysis in nitrogen-doped titanium oxides," *Science*, vol. 293, no. 5528, pp. 269–271, 2001.

[21] J. M. Luther, M. Law, M. C. Beard, Q. Song, M. O. Reese, R. J. Ellingson, and A. J. Nozik, "Schottky solar cells based on colloidal nanocrystal films," *Nano Letters*, vol. 8, no. 10, pp. 3488–3492, 2008.

[22] W. Ma, J. M. Luther, H. Zheng, Y. Wu, and A. P. Alivisatos, "Photovoltaic devices employing ternary PbS_xSe_{1-x} nanocrystals," *Nano Letters*, vol. 9, no. 4, pp. 1699–1703, 2009.

[23] R. Vogel, P. Hoyer, and H. Weller, "Quantum-sized PbS, CdS, Ag_2S, Sb_2S_3, and Bi_2S_3 particles as sensitizers for various nanoporous wide-bandgap semiconductors," *The Journal of Physical Chemistry*, vol. 98, no. 12, pp. 3183–3188, 1994.

[24] B. Sun, H. J. Snaith, A. S. Dhoot, S. Westenhoff, and N. C. Greenham, "Vertically segregated hybrid blends for photovoltaic devices with improved efficiency," *Journal of Applied Physics*, vol. 97, no. 1, p. 014914, 2005.

[25] X. Peng, L. Manna, W. Yang, J. Wickham, E. Scher, A. Kadavanich, and A. Alivisatos, "Shape control of CdSe nanocrystals," *Nature*, vol. 404, no. 6773, pp. 59–61, 2000.

[26] Y. Yin and A. Alivisatos, "Colloidal nanocrystal synthesis and the organic-inorganic interface," *Nature*, vol. 437, no. 7059, pp. 664–670, 2005.

[27] W. U. Huynh, J. J. Dittmer, and A. P. Alivisatos, "Hybrid nanorod-polymer solar cells," *Science*, vol. 295, no. 5564, pp. 2425–2427, 2002.

[28] M. A. Hines and P. Guyot-Sionnest, "Synthesis and characterization of strongly luminescing ZnS-capped CdSe nanocrystals," *The Journal of Physical Chemistry*, vol. 100, no. 2, pp. 468–471, 1996.

[29] X. Wang, X. Ren, K. Kahen, M. A. Hahn, M. Rajeswaran, S. Maccagnano-Zacher, J. Silcox, G. E. Cragg, A. L. Efros, and T. D. Krauss, "Non-blinking semiconductor nanocrystals," *Nature*, vol. 459, no. 7247, pp. 686–689, 2009.

[30] S. Kim, B. Fisher, H.-J. Eisler, and M. Bawendi, "Type-II quantum dots: CdTe/CdSe(core/shell) and CdSe/ZnTe(core/shell) heterostructures," *Journal of the American Chemical Society*, vol. 125, no. 38, pp. 11 466–11 467, 2003.

[31] V. I. Klimov, S. A. Ivanov, J. Nanda, M. Achermann, I. Bezel, J. A. McGuire, and A. Piryatinski, "Single-exciton optical gain in semiconductor nanocrystals," *Nature*, vol. 447, no. 7143, pp. 441–446, 2007.

[32] L. P. Balet, S. A. Ivanov, A. Piryatinski, M. Achermann, and V. I. Klimov, "Inverted core/shell nanocrystals continuously tunable between type-I and type-II localization regimes," *Nano Letters*, vol. 4, no. 8, pp. 1485–1488, 2004.

[33] A. M. Smith, A. M. Mohs, and S. Nie, "Tuning the optical and electronic properties of colloidal nanocrystals by lattice strain," *Nature Nanotechnology*, vol. 4, no. 1, pp. 56–63, 2009.

[34] W. Shi, H. Zeng, Y. Sahoo, T. Y. Ohulchanskyy, Y. Ding, Z. L. Wang, M. Swihart, and P. N. Prasad, "A general approach to binary and ternary hybrid nanocrystals," *Nano Letters*, vol. 6, no. 4, pp. 875–881, 2006.

[35] J. Yang, H. I. Elim, Q. Zhang, J. Y. Lee, and W. Ji, "Rational synthesis, self-assembly, and optical properties of PbS-Au heterogeneous nanostructures via preferential deposition," *Journal of the American Chemical Society*, vol. 128, no. 36, pp. 11 921–11 926, 2006.

[36] M. Casavola, V. Grillo, E. Carlino, C. Giannini, F. Gozzo, E. Fernandez Pinel, M. A. Garcia, L. Manna, R. Cingolani, and P. D. Cozzoli, "Topologically controlled growth of magnetic-metal-functionalized semiconductor oxide nanorods," *Nano Letters*, vol. 7, no. 5, pp. 1386–1395, 2007.

[37] T. Mokari, C. Sztrum, A. Salant, E. Rabani, and U. Banin, "Formation of asymmetric one-sided metal-tipped semiconductor nanocrystal dots and rods," *Nature Materials*, vol. 4, no. 11, pp. 855–863, 2005.

[38] J. Gao, B. Zhang, Y. Gao, Y. Pan, X. Zhang, and B. Xu, "Fluorescent magnetic nanocrystals by sequential addition of reagents in a one-pot reaction: a simple preparation for multifunctional nanostructures," *Journal of the American Chemical Society*, vol. 129, no. 39, pp. 11 928–11 935, 2007.

[39] R. Buonsanti, V. Grillo, E. Carlino, C. Giannini, M. L. Curri, C. Innocenti, C. Sangregorio, K. Achterhold, F. G. Parak, A. Agostiano, and P. D. Cozzoli, "Seeded growth of asymmetric binary nanocrystals made of a semiconductor TiO_2 rodlike section and a magnetic γ-Fe_2O_3 spherical domain," *Journal of the American Chemical Society*, vol. 128, no. 51, pp. 16 953–16 970, 2006.

[40] D. V. Talapin, J. H. Nelson, E. V. Shevchenko, S. Aloni, B. Sadtler, and A. P. Alivisatos, "Seeded growth of highly luminescent CdSe/CdS nanoheterostructures with rod and tetrapod morphologies," *Nano Letters*, vol. 7, no. 10, pp. 2951–2959, 2007.

[41] L. Carbone, C. Nobile, M. De Giorgi, F. D. Sala, G. Morello, P. Pompa, M. Hytch, E. Snoeck, A. Fiore, I. R. Franchini, M. Nadasan, A. F. Silvestre, L. Chiodo, S. Kudera, R. Cingolani, R. Krahne, and L. Manna, "Synthesis and micrometer-scale assembly of colloidal CdSe/CdS nanorods prepared by a seeded growth approach," *Nano Letters*, vol. 7, no. 10, pp. 2942–2950, 2007.

[42] H. Zhong and G. D. Scholes, "Shape tuning of type II CdTe-CdSe colloidal nanocrystal heterostructures through seeded growth," *Journal of the American Chemical Society*, vol. 131, no. 26, pp. 9170–9171, 2009.

[43] T. Mokari, E. Rothenberg, I. Popov, R. Costi, and U. Banin, "Selective growth of metal tips onto semiconductor quantum rods and tetrapods," *Science*, vol. 304, no. 5678, pp. 1787–1790, 2004.

[44] K.-W. Kwon, B. H. Lee, and M. Shim, "Structural evolution in metal oxide/semiconductor colloidal nanocrystal heterostructures," *Chemistry of Materials*, vol. 18, no. 26, pp. 6357–6363, 2006.

[45] K.-W. Kwon and M. Shim, "γ-Fe_2O_3/II-VI sulfide nanocrystal heterojunctions," *Journal of the American Chemical Society*, vol. 127, no. 29, pp. 10 269–10 275, 2005.

[46] H. McDaniel and M. Shim, "Size and growth rate dependent structural diversification of Fe_3O_4/CdS anisotropic nanocrystal heterostructures," *ACS Nano*, vol. 3, no. 2, pp. 434–440, 2009.

[47] T. Sadowski and R. Ramprasad, "Core/shell CdSe/CdTe heterostructure nanowires under axial strain," *The Journal of Physical Chemistry C*, vol. 114, no. 4, pp. 1773–1781, 2010.

[48] H. Zhong, Y. Zhou, Y. Yang, C. Yang, and Y. Li, "Synthesis of type II CdTe-CdSe nanocrystal heterostructured multiple-branched rods and their photovoltaic applications," *The Journal of Physical Chemistry C*, vol. 111, no. 17, pp. 6538–6543, 2007.

[49] Y. Li, R. Mastria, A. Fiore, C. Nobile, L. Yin, M. Biasiucci, G. Cheng, A. M. Cucolo, R. Cingolani, L. Manna, and G. Gigli, "Improved photovoltaic performance of heterostructured tetrapod-shaped CdSe/CdTe nanocrystals using C60 interlayer," *Advanced Materials*, vol. 21, no. 44, pp. 4461–4466, 2009.

[50] J. Bang, J. Park, J. H. Lee, N. Won, J. Nam, J. Lim, B. Y. Chang, H. J. Lee, B. Chon, J. Shin, J. B. Park, J. H. Choi, K. Cho, S. M. Park, T. Joo, and S. Kim, "ZnTe/ZnSe (core/shell) type-II quantum dots: Their optical and photovoltaic properties," *Chemistry of Materials*, vol. 22, no. 1, pp. 233–240, 2010.

[51] T. Hyeon, S. S. Lee, J. Park, Y. Chung, and H. B. Na, "Synthesis of highly crystalline and monodisperse maghemite nanocrystallites without a size-selection process," *Journal of the American Chemical Society*, vol. 123, no. 51, pp. 12 798–12 801, 2001.

[52] W. Bollmann, *Crystal defects and crystalline interfaces*. Berlin, New York: Springer-Verlag, 1970.

[53] H. Grimmer, "the generation function for coincidence site lattices in the cubic system," *Acta Crystallographica*, vol. A40, pp. 108–112, 1984.

[54] A. Trampert and K. Ploog, "Heteroepitaxy of large-misfit systems: Role of coincidence lattice," *Crystal Research and Technology*, vol. 35, no. 6-7, pp. 793–806, 2000.

[55] A. Brokman and R. Balluffi, "Coincidence lattice model for the structure and energy of grain boundaries," *Acta Metallurgica*, vol. 29, no. 10, pp. 1703 – 1719, 1981.

[56] S.-H. Choi, E.-G. Kim, and T. Hyeon, "One-pot synthesis of copper-indium sulfide nanocrystal heterostructures with acorn, bottle, and larva shapes," *Journal of the American Chemical Society*, vol. 128, no. 8, pp. 2520–2521, 2006.

[57] W. Han, L. Yi, N. Zhao, A. Tang, M. Gao, and Z. Tang, "Synthesis and shape-tailoring of copper sulfide/indium sulfide-based nanocrystals," *Journal of the American Chemical Society*, vol. 130, no. 39, pp. 13 152–13 161, 2008.

[58] H. McDaniel, J.-M. Zuo, and M. Shim, "Anisotropic strain-induced curvature in type-II CdSe/CdTe nanorod heterostructures," *Journal of the American Chemical Society*, vol. 132, no. 10, pp. 3286–3288, 2010.

[59] M. Shim and H. McDaniel, "Anisotropic nanocrystal heterostructures: Synthesis and lattice strain," *Current Opinion in Solid State and Materials Science*, vol. 14, no. 5, pp. 83 – 94, 2010.

[60] A. E. Saunders, B. Koo, X. Wang, C.-K. Shih, and B. A. Korgel, "Structural characterization and temperature-dependent photoluminescence of linear CdTe/CdSe/CdTe heterostructure nanorods," *ChemPhysChem*, vol. 9, no. 8, pp. 1158–1163, 2008.

[61] B. Koo and B. A. Korgel, "Coalescence and interface diffusion in linear CdTe/CdSe/CdTe heterojunction nanorods," *Nano Letters*, vol. 8, no. 8, pp. 2490–2496, 2008.

[62] D. C. Lee, I. Robel, J. M. Pietryga, and V. I. Klimov, "Infrared-active heterostructured nanocrystals with ultralong carrier lifetimes," *Journal of the American Chemical Society*, vol. 132, no. 29, pp. 9960–9962, 2010.

[63] S. Yang, D. Prendergast, and J. B. Neaton, "Strain-induced band gap modification in coherent core/shell nanostructures," *Nano Letters*, vol. 10, no. 8, pp. 3156–3162, 2010.

[64] S. K. Yadav, T. Sadowski, and R. Ramprasad, "Density functional theory study of ZnX (X = O, S, Se, Te) under uniaxial strain," *Phys. Rev. B*, vol. 81, no. 14, p. 144120, 2010.

[65] C.-Y. Yeh, Z. W. Lu, S. Froyen, and A. Zunger, "Zinc-blende–wurtzite polytypism in semiconductors," *Phys. Rev. B*, vol. 46, no. 16, pp. 10 086–10 097, 1992.

[66] R. E. Bailey and S. Nie, "Alloyed semiconductor quantum dots: Tuning the optical properties without changing the particle size," *Journal of the American Chemical Society*, vol. 125, no. 23, pp. 7100–7106, 2003.

[67] D. K. Smith, J. M. Luther, O. E. Semonin, A. J. Nozik, and M. C. Beard, "Tuning the synthesis of ternary lead chalcogenide quantum dots by balancing precursor reactivity," *ACS Nano*, vol. 5, no. 1, pp. 183–190, 2011.

[68] R. Islam, H. D. Banerjee, and D. R. Rao, "Structural and optical properties of $CdSe_xTe_{1-x}$ thin films grown by electron beam evaporation," *Thin Solid Films*, vol. 266, no. 2, pp. 215 – 218, 1995.

[69] S. Pennycook, "Z-contrast stem for materials science," *Ultramicroscopy*, vol. 30, no. 1-2, pp. 58 – 69, 1989.

[70] S. J. Pennycook, M. F. Chisholm, A. R. Lupini, M. Varela, A. Y. Borisevich, M. P. Oxley, W. D. Luo, K. van Benthem, S.-H. Oh, D. L. Sales, S. I. Molina, J. Garca-Barriocanal, C. Leon, J. Santamara, S. N. Rashkeev, and S. T. Pantelides, "Aberration-corrected scanning transmission electron microscopy: from atomic imaging and analysis to solving energy problems," *Philosophical Transactions of the Royal Society A: Mathematical, Physical and Engineering Sciences*, vol. 367, no. 1903, pp. 3709–3733, 2009.

[71] M. C. Sarahan, M. Chi, D. J. Masiel, and N. D. Browning, "Point defect characterization in HAADF-STEM images using multivariate statistical analysis," *Ultramicroscopy*, vol. 111, no. 3, pp. 251 – 257, 2011.

[72] J. R. McBride, T. C. Kippeny, S. J. Pennycook, and S. J. Rosenthal, "Aberration-corrected Z-contrast scanning transmission electron microscopy of CdSe nanocrystals," *Nano Letters*, vol. 4, no. 7, pp. 1279–1283, 2004.

[73] S. Molina, D. Sales, P. Galindo, D. Fuster, Y. Gonzlez, B. Aln, L. Gonzlez, M. Varela, and S. Pennycook, "Column-by-column compositional mapping by Z-contrast imaging," *Ultramicroscopy*, vol. 109, no. 2, pp. 172 – 176, 2009.

[74] C. J. Dooley, S. D. Dimitrov, and T. Fiebig, "Ultrafast electron transfer dynamics in CdSe/CdTe donor-acceptor nanorods," *The Journal of Physical Chemistry C Letters*, vol. 112, no. 32, pp. 12 074–12 076, 2008.

[75] C.-H. Chuang, S. S. Lo, G. D. Scholes, and C. Burda, "Charge separation and recombination in CdTe/CdSe core/shell nanocrystals as a function of shell coverage: Probing the onset of the quasi type-II regime," *The Journal of Physical Chemistry Letters*, vol. 1, no. 17, pp. 2530–2535, 2010.

[76] H. Zhu, N. Song, and T. Lian, "Wave function engineering for ultrafast charge separation and slow charge recombination in type II core/shell quantum dots," *Journal of the American Chemical Society*, vol. 133, no. 22, pp. 8762–8771, 2011.

[77] C. She, A. Demortiere, E. V. Shevchenko, and M. Pelton, "Using shape to control photoluminescence from CdSe/CdS core/shell nanorods," *The Journal of Physical Chemistry Letters*, vol. 2, no. 12, pp. 1469–1475, 2011.

[78] S. Geyer, V. J. Porter, J. E. Halpert, T. S. Mentzel, M. A. Kastner, and M. G. Bawendi, "Charge transport in mixed CdSe and CdTe colloidal nanocrystal films," *Phys. Rev. B*, vol. 82, no. 15, p. 155201.

[79] A. G. Pattantyus-Abraham, I. J. Kramer, A. R. Barkhouse, X. Wang, G. Konstantatos, R. Debnath, L. Levina, I. Raabe, M. K. Nazeeruddin, M. Gratzel, and E. H. Sargent, "Depleted-heterojunction colloidal quantum dot solar cells," *ACS Nano*, vol. 4, no. 6, pp. 3374–3380, 2010.

[80] J. B. Sambur, T. Novet, and B. A. Parkinson, "Multiple exciton collection in a sensitized photovoltaic system," *Science*, vol. 330, no. 6000, pp. 63–66, 2010.

[81] F. Shieh, A. E. Saunders, and B. A. Korgel, "General shape control of colloidal CdS, CdSe, CdTe quantum rods and quantum rod heterostructures," *The Journal of Physical Chemistry B*, vol. 109, no. 18, pp. 8538–8542, 2005.

[82] J. E. Halpert, V. J. Porter, J. P. Zimmer, and M. G. Bawendi, "Synthesis of CdSe/CdTe nanobarbells," *Journal of the American Chemical Society*, vol. 128, no. 39, pp. 12 590–12 591, 2006.

[83] S. Kumar, M. Jones, S. S. Lo, and G. Scholes, "Nanorod heterostructures showing photoinduced charge separation," *Small*, vol. 3, no. 9, pp. 1633–1639, 2007.

[84] J. H. Bang and P. V. Kamat, "Quantum dot sensitized solar cells. a tale of two semiconductor nanocrystals: CdSe and CdTe," *ACS Nano*, vol. 3, no. 6, pp. 1467–1476, 2009.

[85] D. Yu, C. Wang, and P. Guyot-Sionnest, "n-type conducting cdse nanocrystal solids," *Science*, vol. 300, no. 5623, pp. 1277–1280, 2003.

[86] D. Vanmaekelbergh and P. Liljeroth, "Electron-conducting quantum dot solids: novel materials based on colloidal semiconductor nanocrystals," *Chemical Society Reviews*.

[87] Y. Liu, M. Gibbs, J. Puthussery, S. Gaik, R. Ihly, H. W. Hillhouse, and M. Law, "Dependence of carrier mobility on nanocrystal size and ligand length in PbSe nanocrystal solids," *Nano Letters*, vol. 10, no. 5, pp. 1960–1969, 2010.

[88] M. Shim and P. Guyot-Sionnest, "Permanent dipole moment and charges in colloidal semiconductor quantum dots," *The Journal of Chemical Physics*, vol. 111, no. 15, pp. 6955–6964, 1999.

[89] D. V. Talapin and C. B. Murray, "PbSe nanocrystal solids for n- and p-channel thin film field-effect transistors," *Science*, vol. 310, no. 5745, pp. 86–89, 2005.

[90] G. Konstantatos, I. Howard, A. Fischer, S. Hoogland, J. Clifford, E. Klem, L. Levina, and E. H. Sargent, "Ultrasensitive solution-cast quantum dot photodetectors," *Nature*, vol. 442, no. 7099, pp. 180–183, 2006.

[91] J. E. Murphy, M. C. Beard, and A. J. Nozik, "Time-resolved photoconductivity of PbSe nanocrystal arrays," *The Journal of Physical Chemistry B*, vol. 110, no. 50, pp. 25 455–25 461, 2006.

[92] J.-S. Lee, M. V. Kovalenko, J. Huang, D. S. Cheng, and D. V. Talapin, "Band-like transport, high electron mobility and high photoconductivity in all-inorganic nanocrystal arrays," *Nature Nanotechnology*, vol. 6, no. 6, pp. 348–352, 2011.

[93] B. L. Wehrenberg, D. Yu, J. Ma, and P. Guyot-Sionnest, "Conduction in charged PbSe nanocrystal films," *The Journal of Physical Chemistry B*, vol. 109, no. 43, pp. 20 192–20 199, 2005.

[94] I. Kaiser, K. Ernst, C. H. Fischer, R. Konenkamp, C. Rost, I. Sieber, and M. C. Lux-Steiner, "The eta-solar cell with $CuInS_2$: A photovoltaic cell concept using an extremely thin absorber (eta)," *Solar Energy Materials and Solar Cells*, vol. 67, no. 1-4, pp. 89 – 96, 2001.

[95] W. W. Yu, L. Qu, W. Guo, and X. Peng, "Experimental determination of the extinction coefficient of CdTe, CdSe, and CdS nanocrystals," *Chemistry of Materials*, vol. 15, no. 14, pp. 2854–2860, 2003.

[96] I. Robel, M. Kuno, and P. V. Kamat, "Size-dependent electron injection from excited CdSe quantum dots into TiO_2 nanoparticles," *Journal of the American Chemical Society*, vol. 129, no. 14, pp. 4136–4137, 2007.

[97] L. Xi, W. X. W. Tan, C. Boothroyd, and Y. M. Lam, "Understanding and controlling the growth of monodisperse CdS nanowires in solution," *Chemistry of Materials*, vol. 20, no. 16, pp. 5444–5452.

[98] H. Kroemer, "Quasi-electric fields and band offsets: Teaching electrons new tricks (nobel lecture)," *ChemPhysChem*, vol. 2, no. 8-9, pp. 490–499, 2001.

AUTHOR'S BIOGRAPHY

The author, Hunter McDaniel, was born on November 16th, 1982 in New Orleans, LA. He attended The Woodlands High School in The Woodlands, TX but graduated from the International School of Bangkok in 2001. He has a Bachelor of Science in Physics and a Bachelor of Engineering from the University of California at Santa Barbara which he earned in 2006. His list of publications include:

"Integration of Type II Nanorod Heterostructures into Photovoltaics" McDaniel, H.; Heil, P.; Tsai, C.; Kim, K.; Shim, M.; submitted, 2011

"Tuning Interfacial Absorption and Recombination in Anisotropic $CdSe/CdSe_xTe_{1-x}$ Nanorod Heterostructures with Size, Shape and Composition" McDaniel, H.; Oh, N.; Shim, M.; in progress, 2011

"Anisotropic Nanocrystal Heterostructures: Synthesis and Lattice Strain" Shim, M.; McDaniel, H.; Curr. Opin. Solid Sate Mater. Sci., 2010, 14, 83

"Anisotropic Strain-Induced Curvature in Type-II CdSe/CdTe Nanorod Heterostructures" McDaniel, H.; Zuo, J.-M.; Shim, M.; J. Am. Chem. Soc., 2010, 132, 3286

"Size and Growth Rate Dependent Structural Diversification of Fe_3O_4/CdS Anisotropic Nanocrystal Heterostructures" McDaniel, H.; Shim, M.; ACS Nano, 2009, 3, 434

"Vortex Dissipation in Type I Superconducting Thin Films" McDaniel, H.; Martinis, J. M.; UCSB senior thesis, 2006